T.R.
GEBZE TECHNICAL UNIVERSITY
GRADUATE SCHOOL OF NATURAL AND APPLIED SCIENCES

NUMERICAL INVESTIGATION OF FLOW THROUGH LABYRINTH SEALS WITH AND WITHOUT HONEYCOMB LANDS

AVNİ ERTAŞ
A THESIS SUBMITTED FOR THE DEGREE OF MASTER
MECHANICAL ENGINEERING DEPARTMENT

GEBZE
2023

T.R.
GEBZE TECHNICAL UNIVERSITY
GRADUATE SCHOOL OF NATURAL AND APPLIED SCIENCES

NUMERICAL INVESTIGATION OF FLOW THROUGH LABYRINTH SEALS WITH AND WITHOUT HONEYCOMB LANDS

AVNİ ERTAŞ
MASTER THESIS
MECHANICAL ENGINEERING DEPARTMENT

THESIS SUPERVISOR
ASSIST. PROF. DR. SALİH ÖZEN ÜNVERDİ

GEBZE
2023

T.R.
GEBZE TEKNİK ÜNİVERSİTESİ
FEN BİLİMLERİ ENSTİTÜSÜ

DÜZ LABİRENT KEÇELERİN BAL PETEK YAPISI İLE VE BAL PETEK YAPISI OLMADAN AKIŞ ALANININ NÜMERİK OLARAK İNCELENMESİ

AVNİ ERTAŞ
YÜKSEK LİSANS TEZİ
MAKİNE MÜHENDİSLİĞİ ANABİLİM DALI

DANIŞMANI
Dr. Öğr. Üyesi SALİH ÖZEN ÜNVERDİ

GEBZE
2023

GEBZE TEKNİK ÜNİVERSİTESİ	**YÜKSEK LİSANS JÜRİ ONAY FORMU**

GTÜ Fen Bilimleri Enstitüsü Yönetim Kurulu'nun 19/07/2023 tarih ve 2023/40 sayılı kararıyla oluşturulan jüri tarafından 14/09/2023 tarihinde tez savunma sınavı yapılan Avni Ertaş'ın tez çalışması Makine Mühendisliği Anabilim Dalında YÜKSEK LİSANS tezi olarak kabul edilmiştir.

JÜRİ

ÜYE

(TEZ DANIŞMANI) : Dr. Öğr. Üyesi Salih Özen ÜNVERDİ

ÜYE : Doç. Dr. Gamze GEDİZ İLİŞ

ÜYE : Prof. Dr. Hasan KARABAY

ONAY

Gebze Teknik Üniversitesi Fen Bilimleri Enstitüsü Yönetim Kurulu'nun
…./…/….. tarih ve ……/…. sayılı kararı.

İMZA/MÜHÜR

SUMMARY

Within the scope of this thesis, the flow structure of labyrinth seals used as sealing elements in gas turbine engines has been examined using computational fluid dynamics (CFD) and experimental studies, both with and without honeycomb structures. Computational simulations were conducted using the ANSYS Fluent software, solving the Navier-Stokes equations with the k–ε Realizable and k–ω SST turbulence models. Validation studies were conducted separately for experimental and Computational Fluid Dynamics (CFD) investigations found in the literature to verify the prepared numerical model. Following a detailed examination of the flow field, a parametric modeling approach was employed to conduct a high number of analyses. The one-dimensional Zimmerman-Wolff equation, commonly used in the literature for estimating leakage flow rates in labyrinth seals, was compared with experimental results. To enhance the accuracy of the existing equation, correction coefficients were introduced to the equation based on geometric parameters and boundary conditions using a hybrid turbulence model approach. Ultimately, the new equation showed a reduction in the error rate from up to 20% in the original equation to as low as 5%. The thesis also investigated the impact of RPM on swirl ratio and windage heating in labyrinth seals. Within the analysis matrix used, it was observed that RPM could reduce the leakage flow by up to 15% compared to static conditions. Additionally, the effect of honeycomb structures commonly used in labyrinth seals was examined. A detailed examination of labyrinth seals with honeycomb structures, 1/16 and 1/32 cell sizes were conducted, revealing that structures with 1/32 cell size could reduce the leakage flow rate by up to 22%. However, when using a 1/16 cell size, it was observed that instead of reducing leakage flow, the fluid utilized the honeycomb cell spaces to further increase it.

Key Words: Straight Through Labyrinth Seals, Computational Fluid Dynamics, Gas Turbine Engines, Honeycomb Lands

ÖZET

Bu tez kapsamında hesaplamalı akışkanlar dinamiği (HAD) ve deneysel çalışmaları kullanarak, gaz türbinli motorlarda sızdırmazlık elemanı olarak kullanılan labirent keçelerin akış yapısını bal petek yapısı ile ve bal petek yapısı olmadan incelenmiştir. Hesaplamalarda ANSYS Fluent yazılımı kullanılarak Navier-Stokes (RANS) denklemleri k–ε Realizable ve k–ω SST türbülans modelleri ile birlikte çözülmüştür. Hazırlanan sayısal modelin doğrulanması amacıyla literatürde yer alan deneysel ve HAD çalışmaları için ayrı ayrı validasyon çalışmaları hazırlanmıştır. Akış alanının detaylı incelenmesi sonrasında yüksek sayıda analizlerin gerçekleştirilmesi için parametrik modelleme yaklaşımı kullanılmıştır. Labirent keçelerdeki kaçak debi miktarının hesaplanmasında literatürde sıklıkla kullanılan Zimmerman-Wolff bir boyutlu denklemi deneysel sonuçlar ile karşılaştırılmış ve mevcut denklemin doğruluğunu arttırmak için geometrik parametrelere ve sınır şartlarına bağlı olarak hibrit türbülans modeli yaklaşımı ile denkleme düzeltme katsayıları ilave edilmiştir. Nihai olarak elde edilen yeni denklemde orjinal denklemde gözlemlenen %20 hata oranının %5 e kadar düştüğü gözlemlenmiştir. Labirent keçelerdeki RPM'in girdap oranı ve hava sürtünme ısıtması üzerindeki etkisi de tez kapsamında araştırılmıştır. Kullanılan analiz matrisinde RPM'in kaçak debi miktarını statik koşullara göre %15 e kadar azaltabildiği gözlemlenmiştir. Ek olarak labirent keçelerde sıklıkla kullanılan bal petek yapılarının akış alanı üzerindeki etkisi de incelenmiştir. 1/16 ve 1/32 bal petek hücre boyutuna sahip labirent keçelerin detaylı incelemesi gerçekleştirilmiş, 1/32 hücre boyutuna sahip bal petek yapılarının kaçak debi miktarını %22 ye kadar azalttığı gözlemlenmiştir. 1/16 hücre boyutu kullanımında ise kaçak debinin azalması yerine akışkanın hücre boşluklarını kullanarak kaçak debiyi daha da arttırdığı görülmüştür.

Anahtar Kelimeler: Düz Labirent Keçeler, Hesaplamalı Akışkanlar Dinamiği, Gaz Türbinli Motorlar, Bal petek yapıları

ACKNOWLEDGEMENTS

First and foremost, I would like to extend my gratitude to my thesis advisor, Assistant Prof. Dr. Salih Özen ÜNVERDİ, for his unwavering support throughout this study. Additionally, I wish to express my appreciation to Prof. Dr. Hasan KARABAY and Dr. Erinç Erdem for their encouragement, patience, and profound knowledge, which played a pivotal role in enabling me to successfully complete my research. A special note of appreciation goes to Tusas Engine Industry (TEI) for providing me with this valuable opportunity and to the dedicated employees who carried out the experimental studies. I would like to dedicate a sincere thank you to my late father, Tarık ERTAŞ, whose unwavering support and encouragement have been my guiding light throughout my journey to complete this master's thesis. His wisdom, guidance, and belief in my capabilities continue to inspire me, even in his absence. Although he is no longer with us, his memory continues to drive my determination to excel in my academic pursuits. I am profoundly grateful for the values he instilled in me and the lessons that have significantly shaped my academic and personal growth. I would also like to convey my gratitude to my family for their enduring understanding and encouragement during this challenging period, as well as to my friends Emre Egemen, Ömer Uyav, and Ahmet Cihat Arıkan for their steadfast support and invaluable feedback. Lastly, I consider myself fortunate to have an incredible wife, Aleyna, who has been my unwavering pillar of support throughout the writing of my Master's Thesis and in every aspect of my life. I express my heartfelt thanks to her for her patience, motivation, and continuous encouragement.

TABLE OF CONTENTS

LIST OF ABBREVIATIONS AND ACRONYMS

Abbreviations and Acronyms		**Explanations**
c	:	Clearance
tt	:	Tooth thickness
s	:	Pitch
n	:	Tooth number
H_{cs}	:	Honeycomb cell size
d_h	:	Honeycomb depth
t_w	:	Honeycomb foil thickness
A	:	Flow area
r_t	:	Seal root radius
T_t	:	Total temperature
P_t	:	Total pressure
P_s	:	Static pressure
PR	:	Pressure ratio
h	:	Enthalpy
S	:	Entropy
γ	:	Gamma
C_p	:	Specific heat in constant pressure
ρ	:	Density
R	:	Molecular gas constant [J/kgK]
μ	:	Dynamic viscosity
v	:	Kinematic viscosity
C_d	:	Discharge coefficient
ϕ	:	Flow function
Re	:	Axial reynolds number
Ta	:	Taylor number
Re_θ	:	Rotational reynolds number
k_2	:	Carry-over coefficient

k_{ctt}	:	Clearance to tooth thickness ratio correction
k_{sc}	:	Pitch to clearance ratio correction
k_n	:	Tooth number correction
$\dot{m}$	:	Mass flow rate
y+	:	Dimensionless first cell distance
ω	:	Specific dissipation rate
ε	:	Dissipation rate
k	:	Turbulent kinetic energy
Ω	:	Shaft angular velocity
V_t	:	Tangential velocity
u_w	:	Wall velocity
β	:	Divergence angle of jet
∇	:	Gradient operator
μ_t	:	Turbulent (Eddy) viscosity
0	:	Refers to flow condition upstream
ctt	:	Clearance to tooth thickness ratio
sc	:	Pitch to clearance ratio
t	:	Total
e	:	Exit

LIST OF FIGURES

LIST OF TABLES

1. INTRODUCTION

Turbomachines are essential for industries, such as aviation, defense, space, and power plant, which require advanced technology and have strategic importance, particularly in aviation. The current gas turbine design trend involves a significant increase in the cycle pressure ratio and turbine inlet temperature, which can provide higher thermal and propulsive efficiencies. To achieve these improvements, there is a growing emphasis on developing sealing technologies that reduce gas path seal leakage, minimize vent leakage, improve the control of cooling circuits, and prevent high levels of seal leakage into critical aerodynamic locations along the turbine gas path. In the upcoming sections, the Brayton cycle, which serves as the fundamental cycle employed in gas turbine engines, will be explained. Additionally, the concept of secondary flows and their applications, the role of sealing elements, and a conclusion discussing essential parameters commonly associated with labyrinth seals will be provided.

1.1. Brayton Cycle

The Brayton cycle is a thermodynamic cycle that describes the operation of a gas turbine engine, which is commonly used in power generation and propulsion systems, such as jet engines and some types of power plants. It serves as a fundamental model for understanding the basic principles of these engines. The ideal Brayton Cycle is given with Figure 1.1. The cycle basically consists of compressor, combustion and turbine.

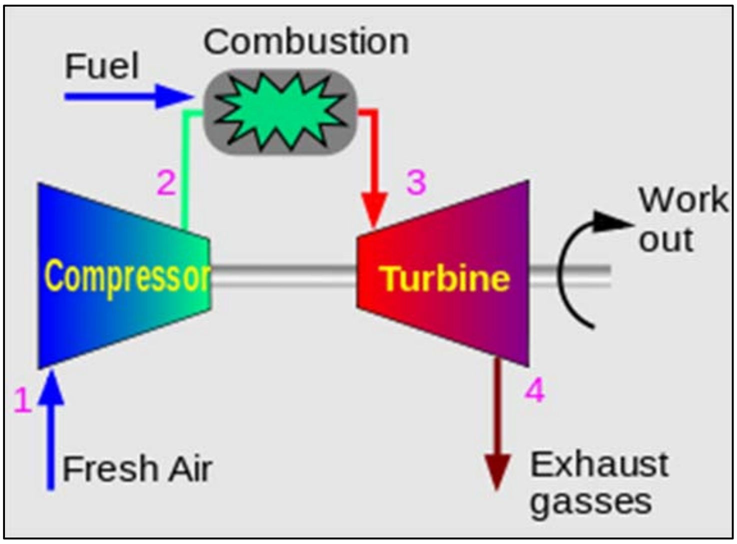

Figure 1.1: Brayton Cycle for Gas Turbine Engines

Figure 1.2 represents temperature-entropy diagram and the cycle begins with the compression process, where atmospheric air is drawn into the compressor of the gas turbine hence temperature rises within the compressor, the air is compressed isentropically, meaning it undergoes a reversible and adiabatic (no heat exchange with the surroundings) process and no entropy generation. The compression process aims to increase the air's density and pressure which in turn enhances the subsequent combustion process. Following compression, the high-pressure, high-temperature air exits the compressor and enters the combustion process. In this phase, fuel is injected into the compressed air stream, and it undergoes combustion at a nearly constant pressure. The combustion process increases the enthalpy of the air. The high-temperature, high-pressure gas mixture now contains the energy derived from the burning fuel. The hot, pressurized gas mixture from the combustion chamber enters the turbine. As the gas flows through the turbine stationary blades, it undergoes an isentropic expansion process. Turbine rotating blades changes the momentum at high-speed hot gases and produces to work on the turbine blades, extracting work from the high-temperature, high-pressure gas. This work is then used to drive the compressor and other auxiliary components of the gas turbine engine. After passing through the turbine, the exhaust gases exit the turbine and are expelled into the atmosphere. The exhaust process occurs at nearly atmospheric pressure, allowing the gas to release excess internal energy to the surroundings. The temperature and pressure of the exhaust gases decrease as a result of this heat dissipation. The cycle is now ready to repeat, with the remaining exhaust gases serving as the starting point for the next cycle.

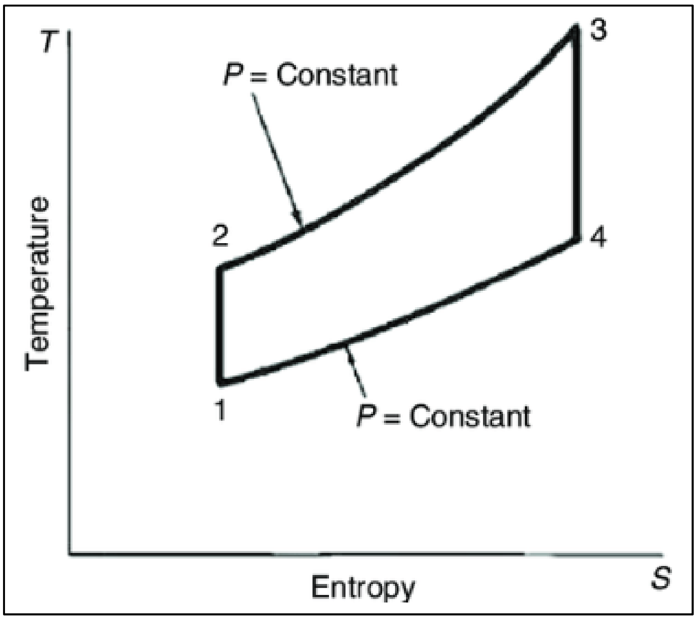

Figure 1.2: Temperature-Entropy Diagram of Brayton Cycle

1.2. Secondary Air System

The secondary air system (SAS) in gas turbine engines is designed to perform various crucial functions beyond the primary combustion process. It involves the controlled circulation of air within the engine to serve purposes like cooling and sealing. Figure 1.3 represents four different stations where SAS flows in used. Station-A used for bearing seal buffering which provide a protective barrier around bearings. Station-B for low-pressure turbine (LPT) cooling flow. Station-C for the high-pressure turbine (HPT) second blade cooling flow. Station-D is the again for HPT cooling in the front stages. It can be seen most of the SAS flow is used in low-pressure turbine (LPT) and high-pressure turbine (HPT).

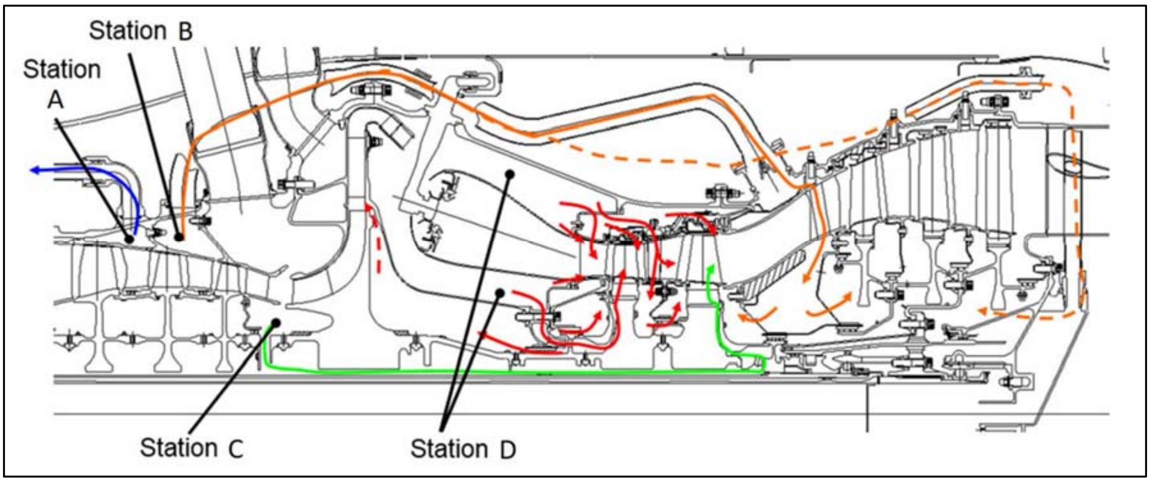

Figure 1.3: Secondary Air System Example of Gas Turbine Engine

Cooling air plays a crucial role in lowering the temperature of both rotating and stationary components. Figure 1.4 shows the air which is supplied to cool the discs and at the same time prevents the hot gas ingestion. Labyrinth seals are used in the areas marked with red in the lower part. Air controlled by labyrinth seals is transferred to these regions in order to prevent the hot gas ingestion in the cavity regions and to cool the discs at the same time. Rim seals are used in the upper part, it serves to prevent hot gas ingestion arising which can trigger thermal fatigue and cracking in the discs.

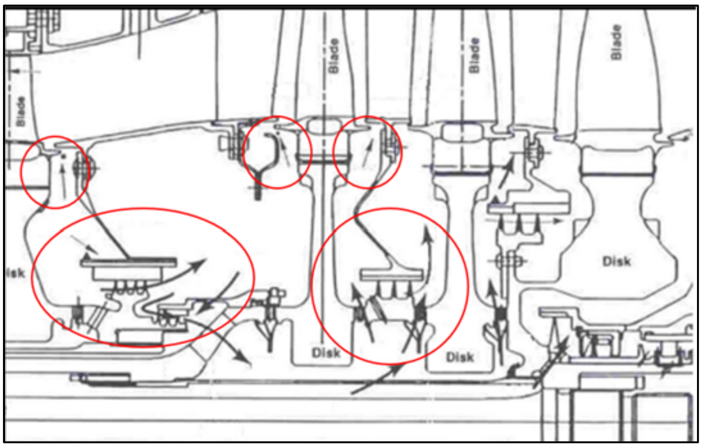

Figure 1.4: SAS Flow for Cooling and Cavity Purging

1.3. Sealing Elements

Sealing elements hold crucial roles within gas-turbine engines, individually contributing to the efficiency and reliability of the engine. In the subsequent discussion, an elaboration on some of the prevalent sealing elements that find application in gas turbine engines will be presented.

1.3.1. Brush seals

These are made of bristles, usually made of metallic materials, such as stainless steel, which are arranged in a radial pattern around the shaft. Figure 1.5 represents brush seal example these are used to prevent gas leakage around the rotating shaft of the engine. Brush seals are a type of seal that demonstrates superior sealing performance compared to labyrinth seals and is produced using advanced technology. These seals are composed of a series of wire bundles supported by front and back plates, positioned in the same direction as the rotation of the rotor. This type of seal can be mounted on the shaft with clearances, direct contact, or interference. In addition to their sealing performance, these seals do not experience permanent wear due to rotor contact during transient conditions and can maintain their sealing effectiveness. Furthermore, these seals occupy less axial space, which provides ease in mechanical design.

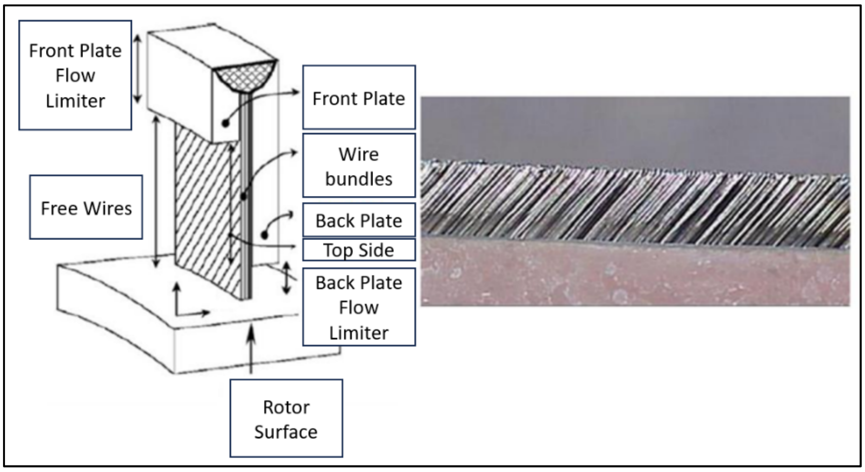

Figure 1.5: Brush Seal

1.3.2. Carbon Seals

In modern gas turbine engines, a new type of seal known as carbon seals is being employed. Figure 1.6 is an example of the carbon seal. These seals represent the cutting-edge of sealing technology in terms of sealing performance. Carbon seals are extensively utilized in the crankcase area of the engine and are notable for their high contact density. Due to this characteristic, effective cooling becomes necessary. Cooling is achieved by supplying oil to the crankcase region. However, the major drawback of carbon seals lies in the challenges associated with their design and the associated costs.

Figure 1.6: Carbon Seals

1.3.3. Labyrinth seals

Figure 1.7 is an example of conventional straight through labyrinth seal. These are composed of a series of fins or ridges that create a tortuous path for gas to flow through. They are used to prevent the leakage of gases along the axis of the rotating shaft. The greatest advantage of labyrinth seals is their ability to be manufactured using traditional methods and operate stably. They are relatively simple compared to other seal types. When used in conjunction with honeycomb structures, their efficiency is enhanced, making them practical for a wide range of operational conditions. However, due to their axial and radial lengths, they are somewhat heavier than other types of seals, and their sealing performance is somewhat inferior. The shape of the teeth, arrangement, space between them, and number of teeth are some of the important parameters that affect the amount of leakage flow.

Figure 1.7: Straight Through Labyrinth Seal

When Figure 1.8 is examined the air in the entrance zone firstly experiences with sudden drop in flow area as in like orifice, flow and pressure drop occurs hence the fluid velocity is increases. At the same time, the radial velocity component in the fluid reaches a certain value due to the sudden narrowing of the flow and the change in direction. This radial velocity component of the fluid causes it to head towards the cavites as it travels along the teeth, creating a circulation flow in pockets. This circulation zone affects the sealing performance due to pressure loss and disturbance of the jet stream flowing from the upper part.

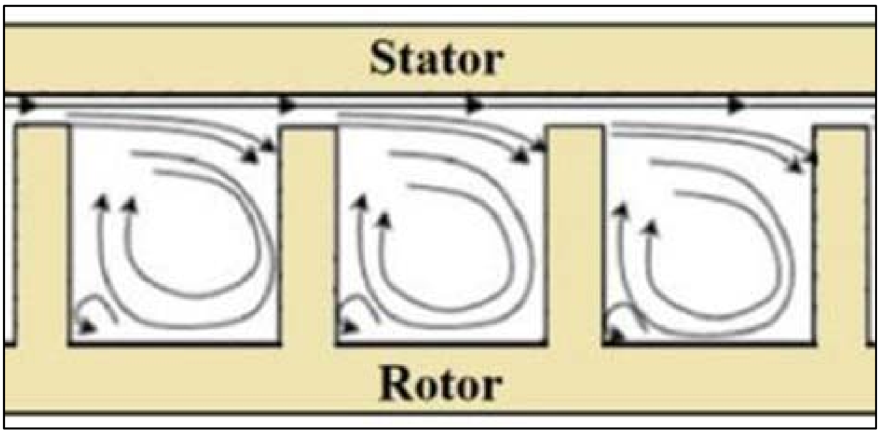

Figure 1.8: Straight Through Labyrinth Seal

Example of secondary air distribution is shown in Figure 1.9. Labyrinth seals are not always used standalone in some regions; they are used with abradable or honeycomb lands. Because seals are a key element for efficiency, proper design of these elements requires a good understanding of flow physics. Once honeycomb lands added to the labyrinth seal honeycomb land structure is now available instead of stator. Honeycombs are mainly increasing the friction and increases the formation of eddies. In addition, directing the fluid into the honeycomb structure will reduce the leakage flow. Honeycomb structures will also create irregularity on the jet flow and in this case, it will reduce the leakage flow and increase the performance of the seal. Choosing the right honeycomb cell size is crucial for achieving optimal performance of the seal. This is because the fluid can exploit the gaps in honeycomb structures with larger cell sizes when passing through a narrow opening, which actually increases the leakage flow rate instead of reducing it.

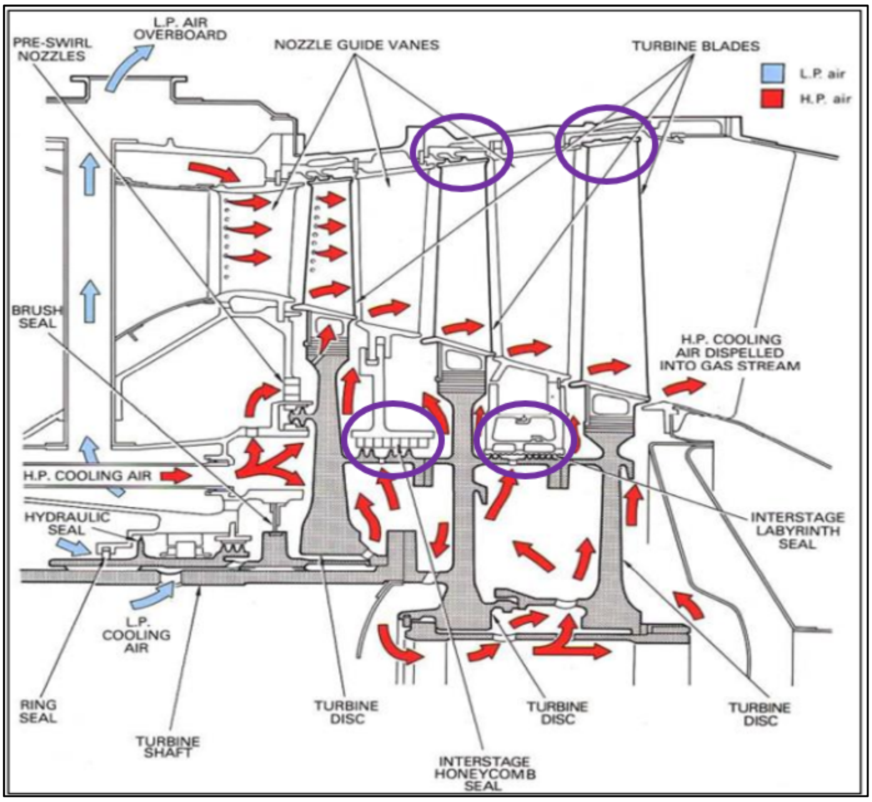

Figure 1.9: Example of Labyrinth Seal Usage in Gas Turbine Engine

Labyrinth seals with honeycomb lands enable reliable operations at lower clearance distances because honeycomb materials are more abradable and honeycomb structure on the stator surface usually wears out during the operation. This results in an increase in the flow turbulence level, which helps the flow enter the honeycomb structure more easily and reduces overall leakage. Figure 1.10 shows an example of a labyrinth seal structure with honeycomb land with geometrical parameters. The main parameters for honeycomb structures are typically cell size, cell depth, and foil thickness as indicated with Figure 1.11. The d_h dimension is typically limited by radial constraints and it represents honeycomb depth. The cell size is generally chosen according to the operating clearance and pressure ratio.

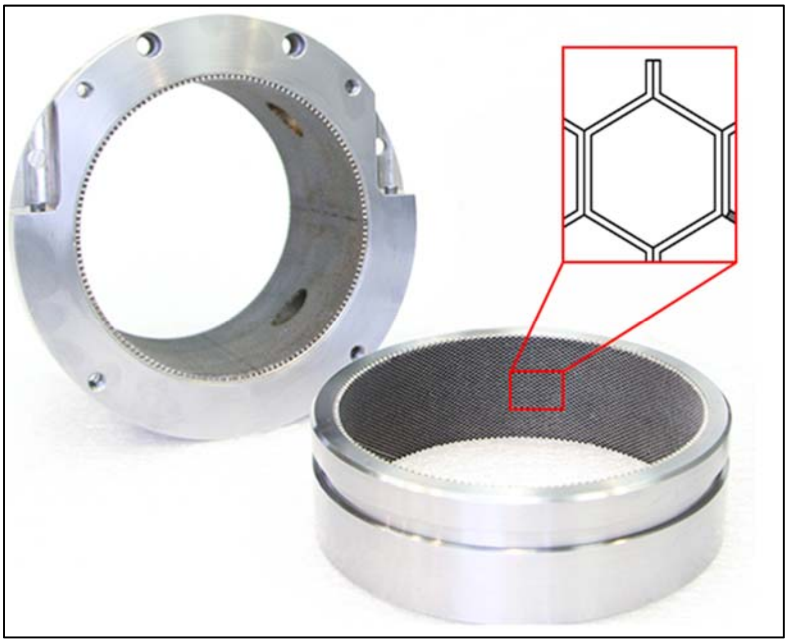

Figure 1.10: Labyrinth Seal with Honeycomb Land

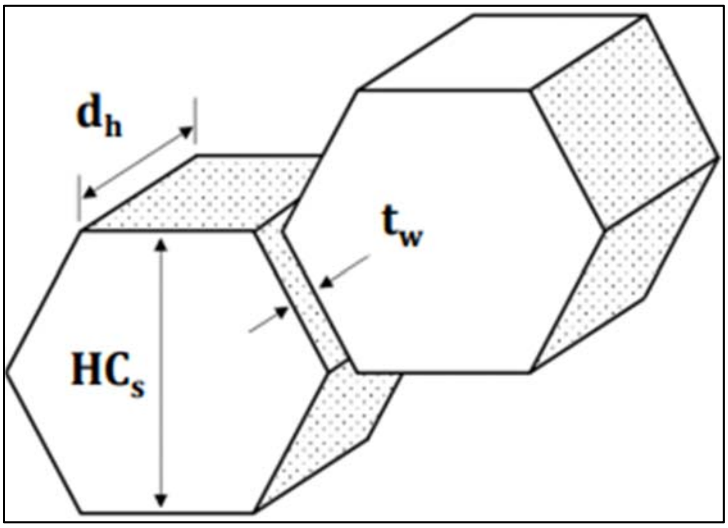

Figure 1.11: Honeycomb Land Geometrical Parameters

The important parameters frequently used for labyrinth seals are given in Table 1.1. Flow function is used to make the amount of leakage flow independent from inlet conditions and geometric differences. The pressure ratio is the critical parameter that determines the operating condition of the labyrinth seals. The axial reynolds number based on the axial velocity of the flow gives information about the flow regime. The rotational Reynolds number helps to understand the dominance of centrifugal forces over viscous forces. Swirl ratio expresses the tangential velocity component of the fluid and the tangential velocity component affects the amount of leakage flow. Windage heating number, on the other hand, generally refers to the heating of the fluid by air friction due to viscous heating in labyrinth seals. The ideal mass flow rate represents the flow that will pass through an area without any loss, and the discharge number represents the ratio of the real flow rate to the ideal flow rate. Finally, Taylor number is a dimensionless quantity that characterizes the importance of centrifugal forces or so-called inertial forces due to rotation of a fluid about an axis, relative to viscous forces. These parameters are useful for examining the performance of the seal.

Table 1.1: Important Parameters for Labyrinth Seals

Parameter	Definition
Flow Function	$\phi = \frac{\dot{m}\sqrt{T_{t0}}}{AP_{t0}}$
Pressure Ratio	P_{t0}/P_{se}
Axial Reynolds Number	$Re = \frac{(\dot{m}/A)2c}{\mu}$
Rotational Reynolds Number	$Re_{\theta} = \frac{\rho\Omega r_t c}{\mu}$
Swirl Ratio	$Swirl\ R = \frac{V_t}{\omega r}$
Windage Heating Number	$\sigma = \frac{\left(2C_p\Delta T_t\right)}{U^2}$
Ideal Mass Flow Rate	$\dot{m}_{ideal} = \frac{APt_0}{\sqrt{T_0}}\sqrt{\frac{1}{Pr}^{\frac{2}{\gamma}} - \frac{1}{Pr}^{\frac{\gamma+1}{\gamma}} \frac{2\gamma}{R(\gamma-1)}}$
Discharge Coefficient	$C_d = \frac{\dot{m}_{real}}{\dot{m}_{ideal}}$
Taylor Number	$T_a = \frac{u_w 2c}{v}\sqrt{\frac{c}{r_w}}$

2. LITERATURE

Becker [1] published the first study to describe labyrinth fluid flow. The flow was treated as a simple annular flow by using the Poiseuille flow approach. The study showed that a decrease in clearance had a greater effect than a change in the fluid path and cavity geometry. Becker's work laid the foundation for further research on labyrinth seals, which are used in various engineering applications to prevent fluid leakage between moving parts such as shafts and casings.

H. M. Martin [2] in 1907 conducted research on labyrinth seals and proposed an equation for calculating leakage flow using gas dynamic fundamentals. Martin's equation assumes a constant flow coefficient and does not consider the effects of the discharge coefficient and kinetic energy transport factor. Martin equation is given with equation 2.1 and detail derivation of Martin equation is also given in [3].

$$\dot{m} = AP_{t0}\sqrt{\frac{1-\left(\frac{P_{se}}{P_{t0}}\right)^{2}}{RT_{t0}\left[n - ln\left(\frac{P_{se}}{P_{t0}}\right)\right]}} \qquad 2.1$$

Stoloda [4] analyzed compressible flows using separate equations for both subsonic and choked flows. The study showed that the mass flow rate is inversely proportional to the square root of the number of teeth, in contrast to Martin’s study, which neglects the effect of kinetic energy carry-over. The carry-over coefficient pertains to the dissipation of energy within the cavity. It quantifies the proportion of kinetic energy that transfers to the subsequent cavity.

Egli [5] examined the effects of the number of teeth and proposed an equation that included factors such as kinetic energy carry-over and the flow coefficient to calculate the leakage flow for straight labyrinth seals. Egli added flow coefficient and carry-over coefficient factor because in ideal modeling, once fluid leaves through the tightes section, it completeley dissipates its kinetic energy and after that there are no velocity components but in real, flow goes into the pockets and joins the circulation. Egli's equation is given with equation 2.2.

$$\dot{m} = k_2 \frac{AP_{t,u}}{\sqrt{RT_u}} \sqrt{\frac{[1-\left(\frac{P_{s,d}}{P_{t,u}}\right)^2]}{n - ln(\frac{P_{s,d}}{P_{t,u}})}} \qquad 2.2$$

Hodkinson [6] approached the issue of kinetic energy carry-over from an analytical fluid mechanics perspective. Hodkinson compared the flow leaving a restriction to a jet, part of which was intercepted by the next opening and carried-over. This phenomenon was considered in the orifice coefficient of the Stodola equation. Hodkinson's study was the first to attempt an analytical prediction of the fluid mechanics origins of the kinetic energy carry-over effect. Hodkinson's equation is given with the equation 2.3 and the kinetic energy carry-over coefficient is given with equation 2.4.

$$\dot{m} = \propto k_2 A \sqrt{\frac{P_{t0} * \rho_0 * [1-\left(\frac{P_{se}}{P_{t0}}\right)^2]}{n}} \qquad 2.3$$

$$k_2 = \left\{1 - \frac{(n-1)(\frac{c}{s})}{n[\left(\frac{c}{s}\right) + 0.02]}\right\}^{-0.5} \qquad 2.4$$

Vermes [7] was another researcher who developed coefficients for kinetic energy carry-over using straight and stepped labyrinth seals. He modified the calculation of leakage flow by using the boundary layer theory to modify Martin's equation. Vermes equation is given with equation 2.5 and the kinetic energy carry-over coefficient is given with equation 2.6.

$$\dot{m} = 5.76 C_d k_2 A \sqrt{\frac{P_{t0}\rho_0[1-\left(\frac{P_{se}}{P_{t0}}\right)^2]}{n+ln(\frac{P_{t0}}{P_n})}} \tag{2.5}$$

$$k_2 = \frac{8.52}{\left[\frac{s-tt}{c}\right]+7.23} \tag{2.6}$$

Zimmerman and Wolff's [8] was developed a model and validated for a wide range of turbomachinery applications. Equation 2.7 and 2.8 are represents the Zimmerman-Wolff's equation to calculate mass flow rate of straight through labyrinth seals without honeycomb lands.

$$\dot{m} = k_2 C_d A P_{t0} \sqrt{\frac{1-(\frac{P_{se}}{P_{t0}})^2}{RT_{t0}[n+ln\left(\frac{P_{t0}}{P_{se}}\right)]}} \tag{2.7}$$

$$k_2 = \sqrt{\frac{n/(n-1)}{1-\left(\frac{n-1}{n}\right)\left[\frac{\frac{c}{l_{pitch}}}{\left(\frac{c}{l_{pitch}}\right)+0.02}\right]}} \tag{2.8}$$

In equation 2.8 it can be seen that the carry-over factor, is a strong function of pitch to clearance ratio and the tooth number. It is basically representing kinetic energy loss of the pockets. Figure 2.2 can be used to find the carry-over factor for different pitch to clearance ratios. It can be seen that as the pitch to clearance ratio increased the carry-over coefficient decreased and this can be explained after the jet flow leaves the vena contract effect, it will penetrate into the next pocket with an angle of β as seen in Figure 2.1.

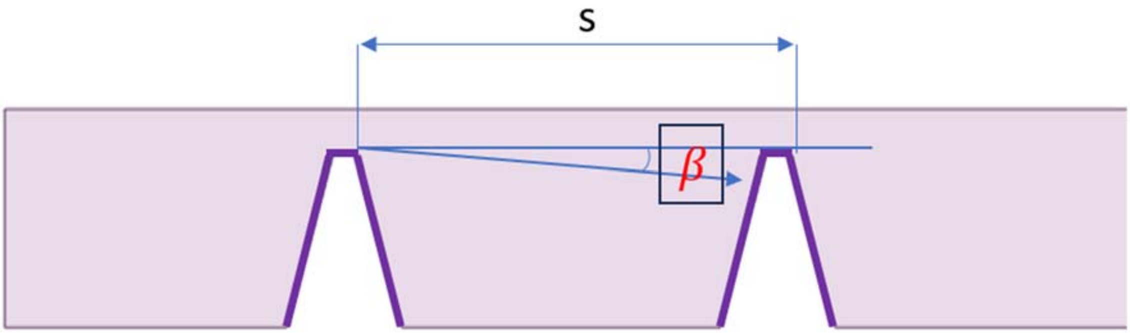

Figure 2.1: Divergence Angle of Jet

As the pitch-to-clearance ratio increases, this penetration will be greater, which will lead to an increase of the circulation zone thus total pressure loss increases and the amount of the leakage flow reduces. The decrease in the amount of leakage flow also means a decrease in the carry-over coefficient. Another coefficient is the C_d, Zimmerman and Wolff showed that it can be described as a function of clearance and tooth thickness. C_d can be found using Figure 2.3 which represents how C_d change with both for Re_{Dh} and ctt ratio. In Figure 2.2 it can be seen that as the clearance to tooth thickness ratio increase by reducing the tooth thickness, the flow in the vena contract region is definitely separated more clearly and narrowing the effective area reducing the leakage flow and thus the C_d value. With a constant tooth thickness as the clearance increases, the effectiveness of the seperated flow at the vena contract region increases more thus C_d reduces.

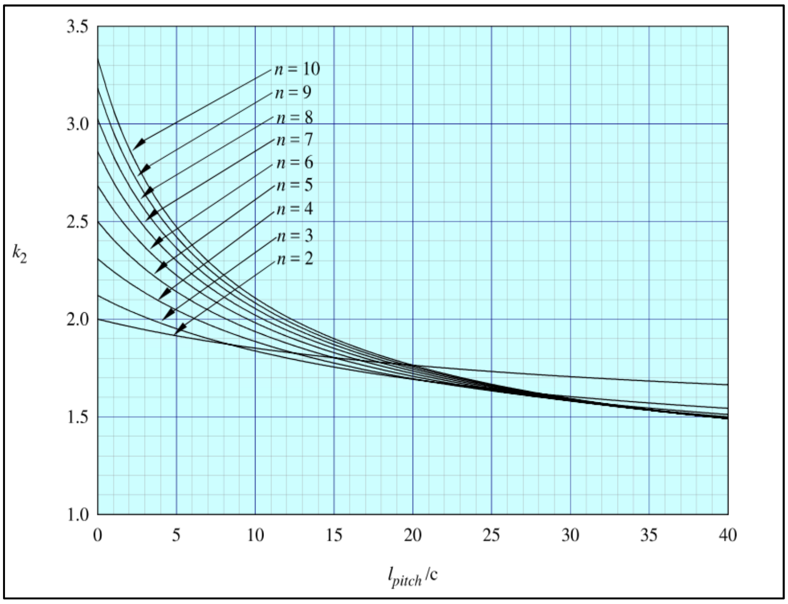

Figure 2.2: Kinetic Energy Carry-Over Coefficient Change with Pitch to Clearance Ratio for Different Tooth Numbers

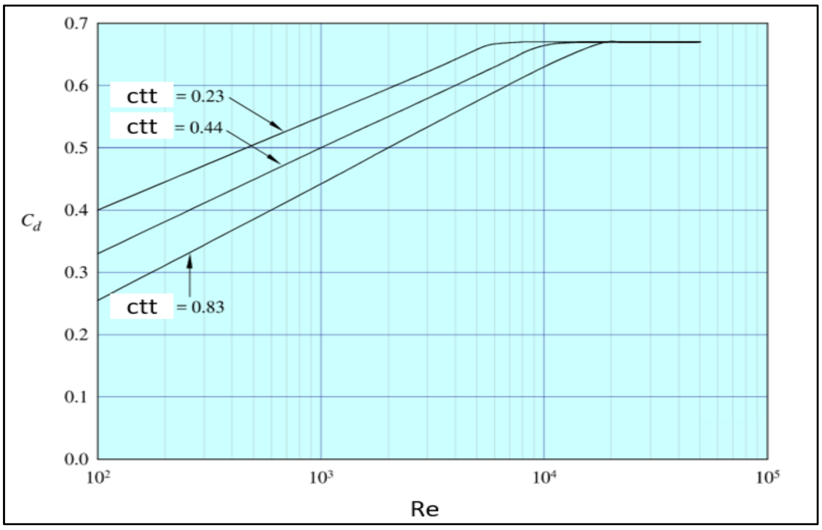

Figure 2.3: Discharge Coefficient Change with Axial Reynolds Number for Different Clearance to Tooth Thicknes Ratio

Zimmerman and Wolff also investigated Stocker's [8] work for honeycomb lands. They found the relation between honeycomb cell size using clearance to cell size ratio for different cell sizes to mass flow reduction. They obtained the curves given in Figure 2.4.

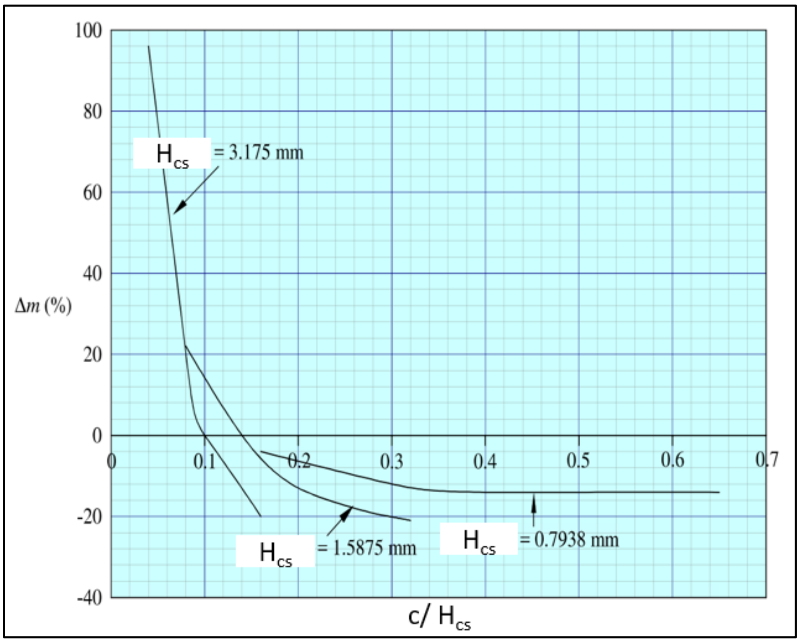

Figure 2.4: Reduction Rate with Clearance to Honeycomb Cell Size Ratio for Different Honeycomb Cell Sizes

Many studies have been conducted to examine the parameters that affect labyrinth seal leakage characteristics. Rhode and Hibbs [9] investigated the effect of the tooth thickness parameter on leakage flow using smooth labyrinth seals. They suggested that swirl development was found to be slightly greater for thicker teeth. Meyer and Lowrie [10] studied the effects of clearance, pitch, and pressure ratio parameters on leakage flow and observed changes in the discharge coefficient. They found that the tooth thickness to clearance and pitch to clearance ratios were effective for the discharge coefficient. At low tooth thickness to clearance ratios, the discharge coefficient showed a significant variation. As the tooth thickness to clearance ratio increased, the variation decreased. They also found that decreasing the pitch to clearance ratio by a factor of 16 increased the discharge coefficient by approximately 18 percent. In 2009, Suryanarayanan and Morrison [11] investigated the effects of different parameters, such as tooth height, tooth thickness, and rotor diameter, on leakage flow. They calculated the transport coefficient, which includes the compressibility effect, and developed a model. The results of the model were compared with the experimental data in the literature. Suryanarayanan and Morrison [12] analyzed the effects of flow conditions and geometry variations on the carry-over coefficient for incompressible flows. They considered the axial reynolds number, pressure ratio, clearance, number of teeth, and shaft speed by using CFD. They found that the axial reynolds number and clearance to pitch ratio had a major influence on the carry-over coefficient. The clearance to pitch ratio varied from 1.0 to 1.8. Suryanarayanan and Morrison [13] proposed a leakage prediction model. Unlike conventional methods, they modeled the discharge coefficient as a function of the carry-over coefficient. Various cases computed using CFD and compressibility were also analyzed and modeled as an expansion factor. They examined the effects of the tooth thickness, tooth height, shaft diameter, and rotation on the discharge coefficient. The non-dimensional numbers tooth thickness to clearance, tooth height to pitch, and the axial reynolds number are used. They found that if the tooth thickness was smaller and/or the clearances were larger, the discharge coefficient was higher across all Re and showed the relationship between the discharge coefficient and axial reynolds number for different tooth thickness to clearance ratios. The results also show that the shaft diameter does not change the discharge coefficient, even when it is three times larger. The effect of the RPM on the leakage flow was also investigated for 20,000 RPM and an axial reynolds number of 239. In this case, the effect was found to be 4%, but it was emphasized that labyrinth seals were used at much higher axial reynolds numbers, and the effect would be negligible. They also showed that the carry-over coefficient is a strong function of the c/s ratio. Finally, they compared their empirical models with existing empirical correlations. In 1975 [14] Stocker used nine different designs for the labyrinth seal and investigated leakage in advanced high-pressure ratio gas turbines. He divided the research into three phases. Stocker showed that increasing cavity turbulence decreases leakage, thereby increasing seal efficiency, and in order to select an appropriate design to provide sufficient leakage, designers must select the optimum configuration. Seal design parameters such as the number of knives, pitch, and step height must be investigated for specific problems.

In the investigation conducted by Demko [15] the impact of rotor rotation speed on leakage flow in labyrinth seals was thoroughly examined through a combination of experimental and numerical approaches. The study introduced a loss coefficient as an effective metric for assessing the influence of rotor rotation speed on pressure drop. Notably, the research unveiled the emergence of secondary flow zones within the seal cavity when rotor speeds exceeded a specific threshold, leading to a reduction in leakage flow. However, it was noted that these secondary flow zones manifested only at relatively high rotation speeds, highlighting their dependence on operational conditions. In a pertinent study by Wensheng et al.[16] the complex relationship between rotor speed and leakage flow rate in labyrinth seals was examined. Employing Ansys CFX, the investigation spanned a spectrum of experimental parameters, encompassing diverse radial gaps, pressure differentials, and rotor speeds. The study revealed noteworthy insights: while increasing pressure differences and increased gap areas the leakage flow increased. Increase in rotor speed up to 20krpm was associated with a reduction in leakage flow about 4%. Washcka's [17] study delved into the behavior of rotating smooth land type labyrinth seals at high speeds, focusing on leakage flow rate and heat transfer using experimental techniques. The experiments involved rotating speeds up to 3000 rpm, and the analysis covered a broad range of conditions, including low axial reynolds numbers and high Taylor numbers. The investigation highlighted the significant influence of rotor speed on labyrinth seal performance, particularly at low axial reynolds numbers, where increasing rotational speed resulted in a noticeable reduction in the mass flow rate coefficient. Remarkably, the study noted that the effect of rotation on leakage flow diminished beyond a specific Ta to Re ratio, while rotation demonstrated an increasing impact on heat transfer. Washcka's findings underscore the importance of considering rotor speed in labyrinth seal analysis, particularly in scenarios involving high-speed rotation, offering insights that contribute to a more comprehensive understanding of labyrinth seal behavior in practical applications.

In 1997 Stocker et. Al [18] moved forward to study solid-smooth, abradable, and honeycomb lands. The objective was to optimize the performance of an advanced labyrinth seal. Some of the major results of this study are as follows:

Honeycomb lands reduce leakage by up to 24% in conventional straight-through labyrinth seals. Rotation reduces straight-through seal leakage by up to 10% for smooth and abradable lands, but it has a negligible effect on honeycomb land. Grooving a porous abradable seal land significantly reduces leakage. Greater roughness increases the leakage. In 2000, Schramm et al. [19] conducted both numerical and experimental studies on stepped labyrinth seals. They observed the flow field using the Laser Doppler Velocimetry method and validated the numerical method using the k-ε turbulence model. It was observed that at small clearances, the fluid tends to move towards the next tooth before entering the cavity regions because of the jet effect. The variation in the clearance affects the flow fields, which directly affects the leakage flow. Choid et al. [20] proposed a 2D modeling approach due to the high computational resources and high-quality mesh requirements of 3D modeling. In their modeling, the honeycomb walls were considered to be flow chambers without thickness. They stated that their analysis encountered convergence problems when a certain thickness was given. Li et al. [21] investigated the effect of honeycomb structures used in steam turbines on leakage flow rate using CFD analysis. They used a standard k-ε turbulence model. They showed that the size and shape of the recirculation zones varied depending on the height and diameter of the honeycomb seal; when the honeycomb cell height remained constant, decreasing the honeycomb cell diameter resulted in lower discharge coefficients and a reduced leakage mass flow rate. Desandos et al. [22] focused on optimizing the stator part of labyrinth seals using different analyses, including several parameters, such as cell diameter, depth, wall thickness, and fin tip thickness. They first validated their numerical model with existing literature data for the discharge coefficient for both smooth and honeycomb labyrinth seals under convergent flow conditions. They then extended the numerical analysis to divergent flow conditions and evaluated honeycomb performance. Finally, we conclude with the following:

- The cell wall thickness only affects the leakage flow rate at very high values, which
  is not applicable to real labyrinth seal applications.
- The cell depth only influences performance below a value of $H_{cs/s} = 2$
- Increasing the tt/H_{cs} ratio and decreasing s/H_{cs} have a strong effect on reducing leakage.

Fraczek et al. [23] investigated the performance of leakage flow in two different honeycomb seal structures. In the first configuration, the clearance was small, and rubbing occurred, whereas in the second configuration, the tooth heights were small, and there was no rubbing. They used the k–ω SST turbulence model and found that as the clearance increased, the fluid flowed directly without undergoing a honeycomb structure, and the rate of leakage reduction decreased. They also indicated that the change in the discharge coefficient value is related to the effective clearance over the fins. Nayak [24] studied the effect of honeycomb land on leakage and windage heating. They used the RNG k-e turbulence model with a modified Schmidt number and validated the CFD methodology based on several experiments. They also showed that the default turbulence model coefficients in CFX did not match well for all pressure ratios, and the maximum flow difference between the numerical model and the experiment was observed at lower seal clearances. They concluded that as the seal clearance decreased, the amount of seal reduction decreased for all honeycomb cell sizes. For example, at a seal clearance of 0.25 mm and honeycomb cell size of 3.2 mm, nearly 65% of seal leakage bypassed through the honeycomb, and it decreased to 5% when the seal clearance reached 2.0 mm. Authors have demonstrated that when utilizing small clearances along with a 3.2 mm honeycomb cell size, there is a decrease in pocket swirl, albeit accompanied by an increase in windage. The elevated bypass flow through honeycomb cells with a diameter of 3.2 mm, exhibiting minimal axial momentum and swirl, results in a decreased overall transfer of swirl at the tooth tip. Kong et al. [25] presents a comprehensive study on the unique characteristics of labyrinth seals within compressor stator wells. Notably, the study explores the impact of inlet and outlet rotor-stator disc cavities on factors such as windage heating, swirl development, and leakage characteristics. Through a combination of experimental testing and numerical simulations, the research delves into the intricate details of flow patterns, temperature variations, and performance metrics. The findings reveal significant insights, including the influence of swirl flow on leakage behavior, reductions in working tip clearance and discharge coefficient at high rotational speeds, and the proportion of windage heating within different cavities.

3. EXPERIMENTAL SETUP

The TEI conducted experimental investigations on a straight-through labyrinth seal. It is noteworthy that these experiments were executed by TEI employees rather than the author himself. This segment will comprehensively cover the experimental setup, the measuring instruments utilized, and the precision associated with these instruments. Furthermore, the labyrinth seal parameters under scrutiny will be specified, and the results will be presented without dimensional units for confidentiality requirements. The general view of the experiment facility is shown in Figure 3.1 and the labyrinth seal is placed in the area marked in red. The details of flow meter instrumentations which is used in the experiments are shown in Table 3.1. Since the pressure ratio range is between 1.1-2.0, the flow rates varied. For this reason, 3 different flowmeter measuring instruments were used. The selection was made according to the appropriate range.

Figure 3.1: Straight Through Labyrinth Seal Experimental Facility General View

Table 3.1: Experimental Flow Measuring Instrumentations Sensivity

CMFS25	F050	F025
1.0 g/s – 4.90 g/s ±%0.49	50 g/s – 200 g/s ±%0.50	19.0 g/s – 90.0 g/s ± %0.50
4.90 g/s – 40.00 g/s ±%0.25	22 g/s – 50 g/s ±%0.69	9.0 g/s – 19.0 g/s ± %0.50

The experimental study involved the utilization of three different clearances, three varying tooth thicknesses, and a range of distinct pressure ratios. All other geometric dimensions were kept constant. The experimental procedures were conducted under static conditions, during which precise measurements of the leakage flow were obtained. Due to the company's confidentiality, the analysis matrix used in the experimental study are provided in Figure 3.2 in a non-dimensionalized form. It should be noted that the targeted clearance values in the test may vary slightly after the measurements are taken.

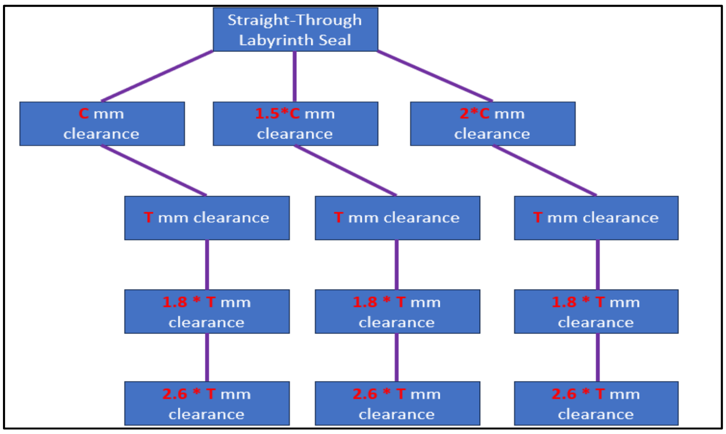

Figure 3.2: Non-Dimensionalized Clearance and Tooth Thickness Values Used in TEI Experiments

Axial reynolds number and discharge coefficient change was examined in the experimental results. The Zimmerman and Wolff equation expressed in equation 2.7 and equation 2.8 is used and added to the comparison.

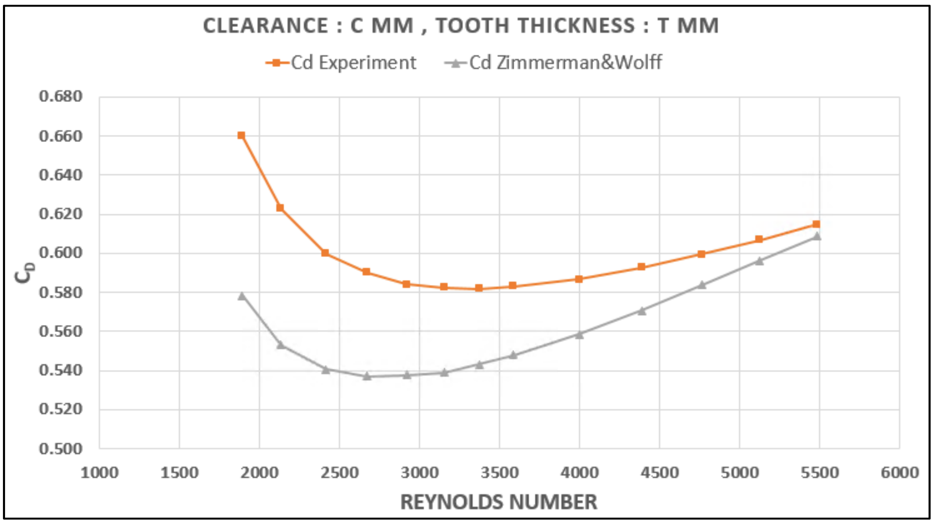

Figure 3.3: Axial Reynolds Number and Discharge Coefficient Comparison with C mm Clearance and T mm Tooth Thickness for the Experiment and Zimmerman-Wolff Equation

When Figure 3.3 is examined, it can be seen that the difference between the experimental results and the Zimmerman-Wolff one-dimensional equation increases especially at low axial reynolds number. Taking into account that the pressure ratio is the only variable that changes, and considering the constant geometric properties of the seal, it becomes evident that the axial reynolds number exhibits a significant dependency on the pressure ratio. As a result, it can be inferred that the Zimmerman-Wolff equation displays a certain deviation from the experimental results especially at low pressure ratios.

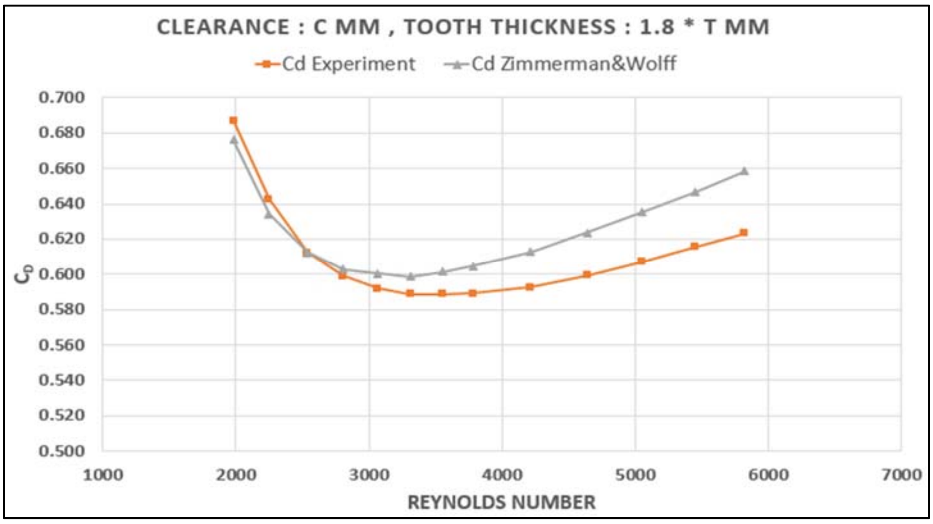

Figure 3.4: Axial Reynolds Number and Discharge Coefficient Comparison with C mm Clearance and 1.8*T mm Tooth Thickness for the Experiment and Zimmerman-Wolff Equation

In Figure 3.4, when the tooth thickness was increased, the discharge coefficient at low axial reynolds number was consistent with the test, but the difference increased when the pressure ratio increased. It has been observed that this situation contradicts with the results of the Figure 3.4 Considering that a fixed pitch and number of teeth are used while performing the tests, in the Zimmerman-Wolff equation the carry-over coefficient will not change as the pressure ratio change. This actually shows that the discharge coefficient value obtained with the using ctt ratio in the Zimmerman-Wolff equation deviates from the experimental results. Figure 3.5 shows that the difference was minimum when the tooth thickness was maximum and the clearance was minimum. In Figure 3.6 it can be seen that low tooth thickness triggers higher deviation again in the low-pressure ratio.

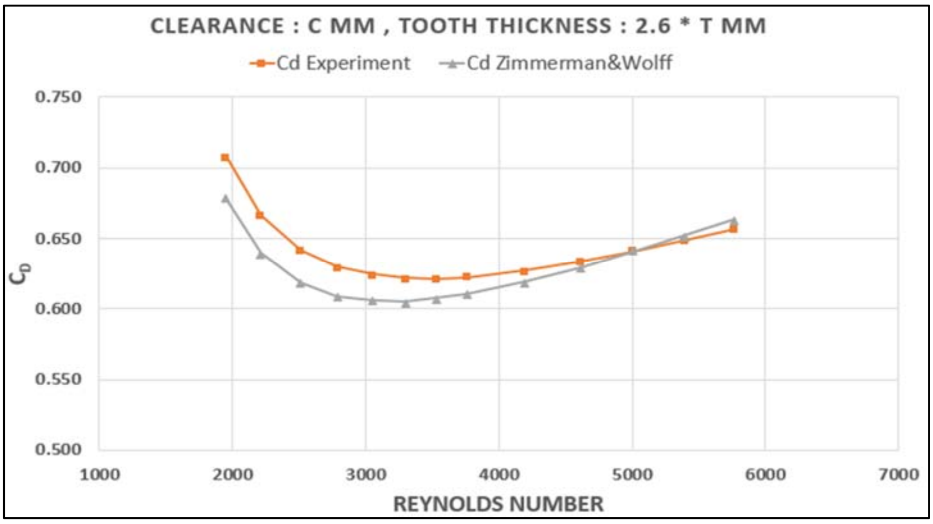

Figure 3.5: Axial Reynolds Number and Discharge Coefficient Comparison with C mm Clearance and 2.6*T mm Tooth Thickness for the Experiment and Zimmerman-Wolff Equation

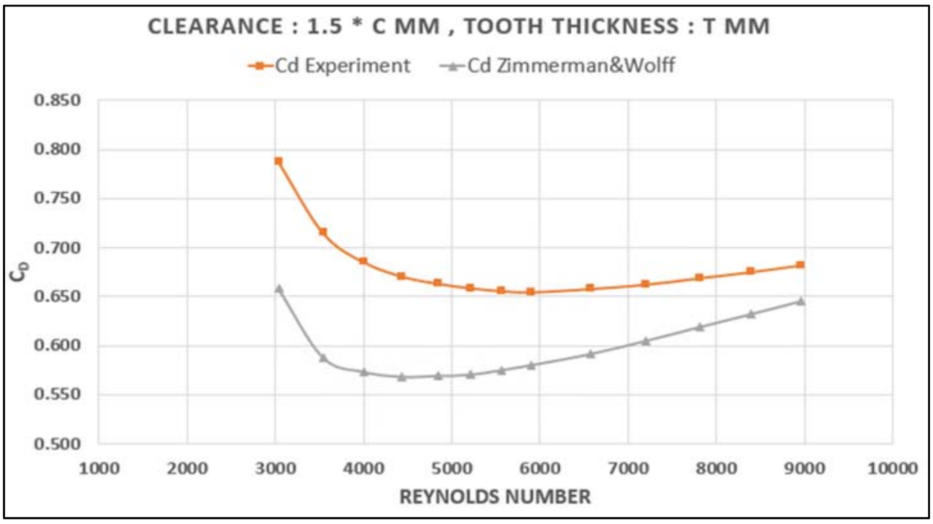

Figure 3.6: Axial Reynolds Number and Discharge Coefficient Comparison with 1.5*C mm Clearance and T mm Tooth Thickness for the Experiment and Zimmerman-Wolff Equation

When Figure 3.7 is examined, the trend is similar with the Figure 3.4 in the low-pressure ratio region. This indicates the there is a need to pay attention for the low tooth thickness and low-pressure ratios.

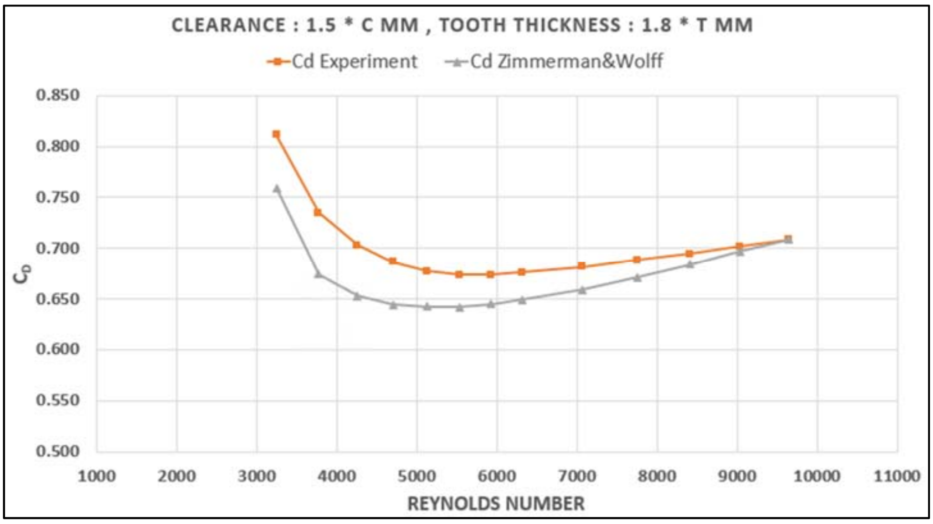

Figure 3.7: Axial Reynolds Number and Discharge Coefficient Comparison with 1.5*C mm Clearance and 1.8*T mm Tooth Thickness for the Experiment and Zimmerman-Wolff Equation

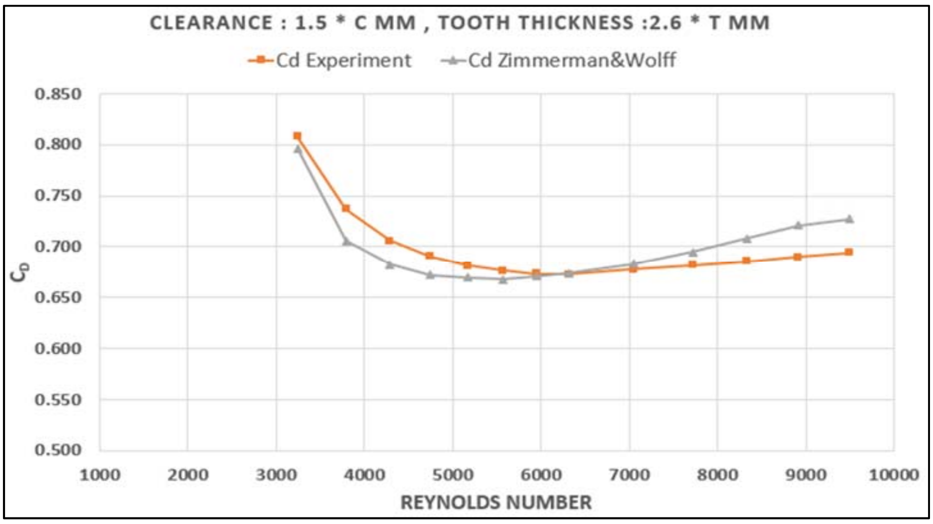

Figure 3.8: Axial Reynolds number Number and Discharge Coefficient Comparison with 1.5*C mm Clearance and 2.6*T mm Tooth Thickness for the Experiment and Zimmerman-Wolff Equation

When the tooth thickness was increased to 1.8 * T in Figure 3.8, it was observed that the experimental results were in agreement. Again, the tooth thickness was maximized and when the Figure 3.7 examined, it was found to Zimmerman-Wolff equation in agreement with the experimental results.

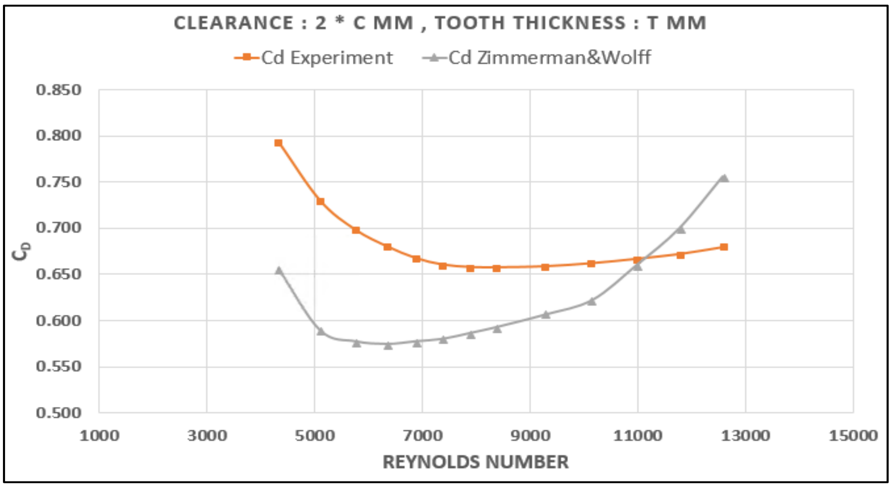

Figure 3.9: Axial Reynolds Number and Discharge Coefficient Comparison with 2*C mm Clearance and T mm Tooth Thickness for the Experiment and Zimmerman-Wolff Equation

When Figure 3.9 is examined, it can be seen that it is similar to Figure 3.6. It is again understood that the Zimmerman-Wolff equation deviates from the experimental results, especially at low pressure ratio and low tooth tip thickness. When Figure 3.10 is examined, even though the clearance has increased, the trend for the lowest tooth thickness was similar at low pressure ratios, but it deviates from the previous results as the pressure ratio increased.

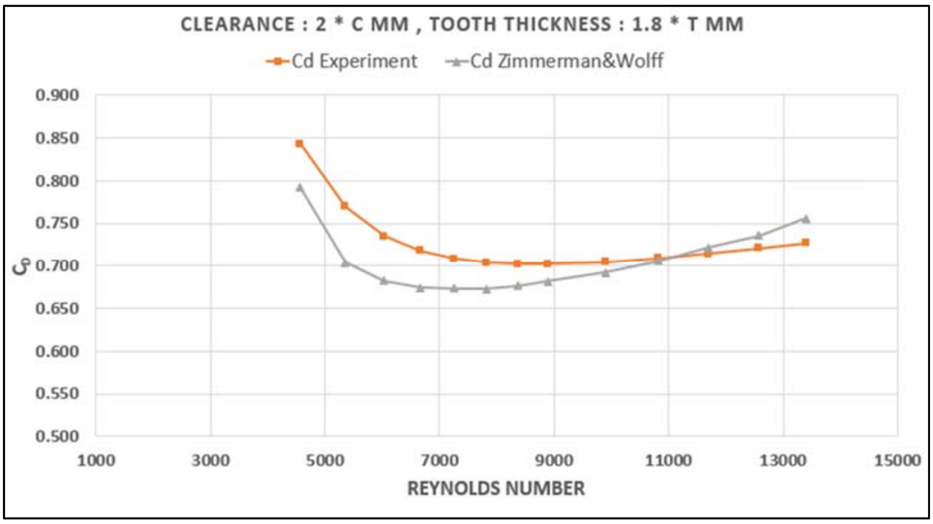

Figure 3.10: Axial Reynolds Number and Discharge Coefficient Comparison with 2*C mm Clearance and 1.8*T mm Tooth Thickness for the Experiment and Zimmerman-Wolff Equation

When Figure 3.11 is examined, it is seen that the trend is similar considering the previous clearances. This indicates that tooth thickness actually causes deviation from the experimental result in the Zimmerman-Wolff one-dimensional correlation.

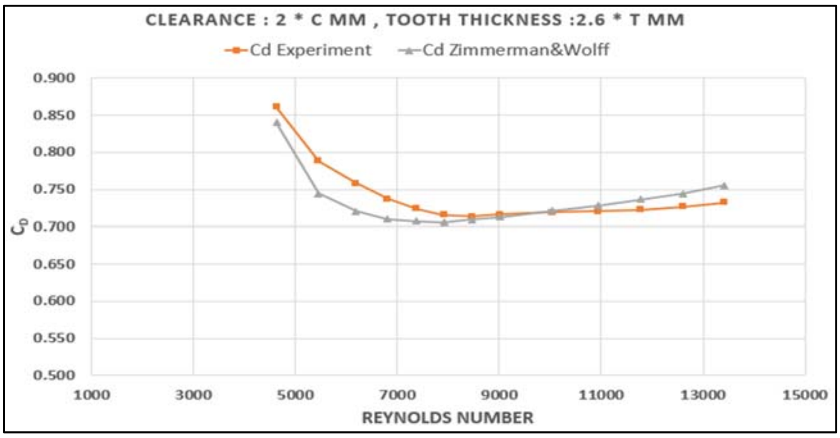

Figure 3.11: Axial Reynolds Number and Discharge Coefficient Comparison with 2*C mm Clearance and 2.6*T mm Tooth Thickness for the Experiment and Zimmerman-Wolff Equation

In general, the conclusions from the experiments are summarized as follows.

- The one-dimensional Zimmerman-Wolff correlation deviates from the experimental result especially at low axial reynolds numbers with low tooth thicknesses.
- Generally, the difference between the experimental results and the one-dimensional correlation decreased as the axial reynolds number increased.
- The effect of tooth thickness on the discharge coefficient is critical to understanding the amount of leakage flow.
- Since fixed pitch and number of teeth were used in the experiment, no comment can be made on the effect of the carry-over coefficient on the contrary ctt ratio is more critical in the experiment.
- Considering the cases, the error rates can reach up to 18% and it seems that an improvement can be made in the correlation.
- When the all results were examined, it was seen that the ctt ratio should be taken as a main correction while improving the correlation.
- It is seen that a separate experimental study is required to examine the pitch effect.

4. NUMERICAL METHOD

The physics of flow in labyrinth seals is complex and includes phenomena such as jet formation, vortex formation, turbulence, circulation, expansion, vena contracta, etc. Nowadays, analytical solutions for all these complex flows are not possible, and they can be solved numerically using Computational Fluid Dynamics (CFD). In CFD conservation of mass, momentum and energy equations solved using the finite volume approach. Table 4.1 represents vector notation of governing equations and in order to apply finite volume approach it should be written in integral form and in the

Table 4.2 integral form of these equations is given. Detailed information is beyond the scope of this thesis.

Table 4.1: Governing Equations - Vector Notation

Continuity Equation	$\frac{\partial \rho}{\partial t} + \nabla.(\rho V) = 0$
X- Momentum Equation	$\frac{\partial(\rho u)}{\partial t} + \nabla.(\rho V u) = \nabla.(\mu \nabla u) - \frac{\partial P}{\partial X} + S_X$
Y- Momentum Equation	$\frac{\partial(\rho v)}{\partial t} + \nabla.(\rho V v) = \nabla.(\mu \nabla v) - \frac{\partial P}{\partial Y} + S_Y$
Z- Momentum Equation	$\frac{\partial(\rho w)}{\partial t} + \nabla.(\rho V u) = \nabla.(\mu \nabla w) - \frac{\partial P}{\partial Z} + S_Z$
Energy Equation	$\frac{\partial(\rho h)}{\partial t} + \nabla.(\rho V h) = \nabla.\left(\frac{k}{C_p}\nabla h\right) + S_h \quad h = C_p(T)$

Table 4.2: Governing Equations - Integral Form

Continuity Equation	$\frac{\partial}{\partial t}\iiint \rho d\forall + \iint V.dA = 0$
X- Momentum Equation	$\frac{\partial}{\partial t}\iiint \rho u d\forall + \iint \rho u(V.dA)$ $= \iint \mu\nabla u.dA + \iiint S_X d\forall$

Tablonun Devamı

Y- Momentum Equation	$\frac{\partial}{\partial t}\iiint \rho v d\forall + \iint \rho v(V.dA) = \iint \mu \nabla v.dA + \iiint S_Y d\forall$
Z- Momentum Equation	$\frac{\partial}{\partial t}\iiint \rho w d\forall + \iint \rho w(V.dA) = \iint \mu \nabla w.dA + \iiint S_Z d\forall$
Energy Equation	$\frac{\partial}{\partial t}\iiint \rho h d\forall + \iint \rho h(V.dA) = \iint \mu \nabla h.dA + \iiint S_h d\forall$, $h = C_p(T)$

Turbulent flow is encountered in real life. It has random fluctuations and it causes further mixing of transport quantities. Currently following major turbulence models can be used for numerical modelling and each of these approaches has both advantages and disadvantages.

- Reynolds Averaged Navier-Stokes Equations (RANS) equation.
- Large Eddy Simulations (LES)
- Direct Numerical Simulation (DNS)

Computational effort of these methods increases from top to bottom. In RANS approach flow variables are considered to be average and variable quantity and the equation 4.1 can be used.

$$\overline{\mu}(x_i , t) = \frac{1}{T}\sum\nolimits_{0}^{T} f(x_i , t)dt \qquad 4.1$$

$$\frac{\partial(\rho\overline{u_i})}{\partial t}+\frac{\partial(\rho\overline{u_i u_j})}{\partial x_j} = -\frac{\partial\overline{p}}{\partial x_j} + \frac{\partial}{\partial x_j}\left[\mu\left(\frac{\partial\overline{u_i}}{\partial x_j}+\frac{\partial\overline{u_j}}{\partial x_i}-\frac{2}{3}\delta_{ij}\frac{\partial\overline{u_m}}{\partial x_m}\right)\right] + \frac{\partial}{\partial x_j}\left(-\boldsymbol{\rho}\overline{\boldsymbol{u}_i'\boldsymbol{u}_j'}\right) \quad 4.2$$

The modified version of the Navier-Stokes equation using the equation 4.1 is given by the equation 4.2. Reynold stress term $-\rho\overline{u_i'u_j'}$ is a symmetric, second order tensor and it comes frome averaging the convective acceleration term in the momentum equation. Reynold stress tensor represents a combination of mixing due to turbulent fluctuation and smoothing by averaging. In order to close the RANS equations, the Reynold stress tensor must be modeled. Eddy viscosity models used in this study which introduce eddy viscosity (or turbulent viscosity) given with equation 4.3. This turbulent viscosity needs to be calculated. The basic equations expressing the turbulent viscosity of the turbulence models used in this study are given in the following sections.

$$-\rho\overline{u_i'u_j'} = \boldsymbol{\mu_t}\left(\frac{\partial\overline{u_i}}{\partial x_j}+\frac{\partial\overline{u_j}}{\partial x_i}\right) - \frac{2}{3}\delta_{ij}\left(\rho k + \boldsymbol{\mu_t}\frac{\partial\overline{u_m}}{\partial x_m}\right) \quad 4.3$$

4.1. Assumptions

Several assumptions have been employed to the computational aspect for this research. Details of these assumptions has been showed in the following sections. These assumptions are:

- For stationary 2D analysis the flow is taken as an axisymmetric which have helped to reduce the flow from three dimensional to two dimensional and for the 2D dynamic analysis axisymmetric with swirl approach has been used.
- Fluid-structure interaction (FSI) has not been included in the analysis to address the influence of surface roughness on the seal geometry. Additionally, the potential impact of lateral surface vibrations resulting from the dynamics of the rotating shaft has been disregarded due to their minimal contribution to fluid turbulence intensity.
- In the present turbulent flow simulations, the widely-used commercial solver FLUENT has been applied to solve the fundamental governing equations.
- Finite-Volume-Method (FVM) have been used to discretized the partial differential equations and turbulence flow modeled using k-ε Realizable model with enhanced wall function in the near wall region to resolve viscous sub-layer.
- In the context of 2D-3D dynamic cases where the energy equation is solved, and temperature varies, Sutherland's viscosity law has been employed.

4.2. K -ε Realizable Turbulence Model

Among the eddy viscosity models shown in previous section, the k-ε turbulence model family, frequently used in the literature for labyrinth seals [24][26]. Equation 4.4 describes the change in turbulent kinetic energy of the fluid. Kinetic energy is related to the square of the velocity of the turbulent motion. Equation 4.5 explains the energy loss of turbulent motion. It shows how the energy of turbulence decreases.

$$\frac{\partial(\rho\kappa)}{\partial t}+\frac{\partial(\rho\kappa u_j)}{\partial x_j}=\frac{\partial}{\partial x_j}\left[\left(\mu+\frac{\mu_t}{\sigma_\kappa}\right)\frac{\partial\kappa}{\partial x_j}\right]+G_k+G_b-\rho\varepsilon-Y_M+S_k \tag{4.4}$$

$$\frac{\partial(\rho\varepsilon)}{\partial t}+\frac{\partial(\rho\varepsilon u_j)}{\partial x_j}=\frac{\partial}{\partial x_j}\left[\left(\mu+\frac{\mu_t}{\sigma_\varepsilon}\right)\frac{\partial\varepsilon}{\partial x_j}\right]+C_{1\varepsilon}\frac{\varepsilon}{k}(G_k+C_{3\varepsilon}G_b)-C_{2\varepsilon}\rho\frac{\varepsilon^2}{k}+S_\varepsilon \tag{4.5}$$

Turbulent viscosity μ_t should not be confused with conventional viscosity μ. Under the influence of turbulence, the viscosity of the fluid can increase. This turbulent viscosity is used to model the fluid becoming more viscous under the influence of turbulence. The relationship between turbulent viscosity k and ε is given by equation 4.6.

$$\mu_t = \rho C_\mu \frac{\kappa^2}{\varepsilon} \tag{4.6}$$

G_k is the generation of turbulence kinetic energy from main flow field due to mean velocity gradients, G_b is the generation of turbulence due to buoyancy, Y_M represents contribution by dilation to the overall dissipation rate in compressible fluid flow. σ_κ , σ_ε are the turbulent Prandtl numbers for κ and ε. In k-ε Realizable turbulence model C_μ is no longer constant (not 0.09) and function of mean strain and rotation rates. Other coefficients and details of the k-ε Realizable turbulence model with detail explanation of this coefficients can be found in related books. [27][28]

4.3. K- ω SST Turbulence Model

K-ω SST (Shear Stress Transport) turbulence model is another advanced turbulence model widely employed in fluid dynamics analyses. This model offers an approach that combines the advantages of both the k-ε and k-ω models to calculate and predict turbulence effects within a fluid flow. The turbulence kinetic energy (k) and specific dissipation rate (ω) obtained from the equation 4.7 and 4.8 respectively.

$$\frac{\partial(\rho\kappa)}{\partial t} + \frac{\partial(\rho\kappa u_j)}{\partial x_j} = \frac{\partial}{\partial x_j}\left[\left(\mu + \frac{\mu_t}{\sigma_\kappa}\right)\frac{\partial\kappa}{\partial x_j}\right] + G_k - Y_k + S_k \tag{4.7}$$

$$\frac{\partial(\rho\omega)}{\partial t} + \frac{\partial(\rho\varepsilon\omega_j)}{\partial x_j} = \frac{\partial}{\partial x_j}\left[\left(\mu + \frac{\mu_t}{\sigma_\omega}\right)\frac{\partial\omega}{\partial x_j}\right] + G_\omega - Y_\omega + D_\omega + S_\omega \tag{4.8}$$

The turbulent viscosity for k-ω SST turbulence model is represented with equation 4.9. Same reference in the previous section can be used for detailed information about other coefficients and detail explanations.

$$\mu_t = \frac{\rho k}{\omega} \frac{1}{\max\left[\frac{1}{\alpha^*}, \frac{SF_2}{\alpha_1 \omega}\right]} \quad 4.9$$

4.4. 2D Axisymmetric Flow Approach

This approach simplifies the analysis by considering the flow in a two-dimensional (2D) plane, assuming that the flow patterns repeat around a central axis. There are no gradients in the circumferential direction. However, this does not mean that there are no swirl velocities. Swirl velocity refers to the rotational component of the fluid's velocity, which can exist even within an axisymmetric flow. The addition of swirl refers to the rotational or angular momentum component of the fluid flow, often seen in systems like jets, cyclones, or rotating machinery. The tangential momentum equation for 2D swirling flows can be written with equation 4.10.

$$\frac{\partial(\rho w)}{\partial t} + \frac{1}{r}\frac{\partial}{\partial x}(r\rho u w) + \frac{1}{r}\frac{\partial}{\partial r}(r\rho v w) = \frac{1}{r}\frac{\partial}{\partial x}\left[r\mu\frac{\partial w}{\partial x}\right] + \frac{1}{r^2}\frac{\partial}{\partial r}\left[r^3\mu\frac{\partial}{\partial r}\left(\frac{w}{r}\right)\right] - \rho\frac{vw}{r} \quad 4.10$$

4.5. Sutherland’s Law of Viscosity

Sutherland's law of viscosity, is an empirical equation that describes the temperature-dependent variation of dynamic viscosity in gases. It is particularly relevant to ideal gases and helps predict how the viscosity of a gas changes with temperature. Sutherland's law with three coefficients is given by the equation 4.11. μ_0 is the reference viscosity (1.716e-5), T_0 is the reference temperature 273.11 K and $\boldsymbol{S}$ is the sutherland constant which is 110.56 K.

$$\mu = \mu_0 \left(\frac{T}{T_0}\right)^{3/2} \frac{T_0 + \boldsymbol{S}}{T + \boldsymbol{S}} \quad 4.11$$

4.6. Mesh Independency

Meshing is a critical step in the simulation process that involves discretizing the geometry of a computational domain into a grid or mesh of smaller elements, such as triangles, quadrilaterals, tetrahedra, or hexahedra as in shown with Figure 4.1.

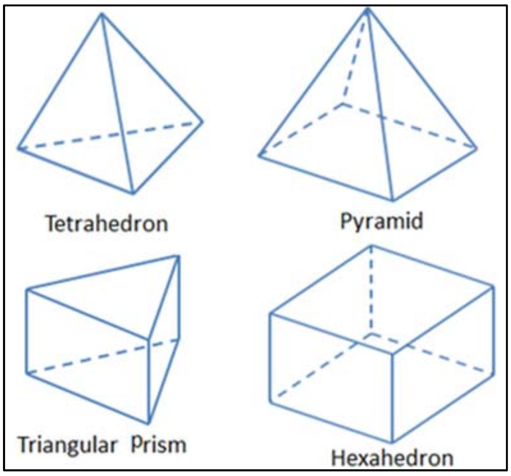

Figure 4.1: Types of Mesh Structures

The quality of the mesh plays a significant role in the accuracy, convergence, and efficiency of CFD simulations. The accuracy of a CFD simulation heavily depends on how well the mesh represents the geometry and flow physics. A fine mesh is necessary to capture high gradients regions. A well-designed mesh also helps simulations converge faster. In labyrinth seals maximum pressure ratio and minimum clearance values were used as an input for the mesh creation process. By creating a mesh with sufficient resolution, at the maximum axial reynolds number that can be reached, it can be ensured that the results at other points will also be reliable. It has been attempted to maintain an appropriate y+ value for different meshes to ensure that the mesh structure is not influenced by the y+ value. To achieve this, the y+ value is always kept at 1 or below. Figure 4.2 shows the results of the mesh independence study for 2D cases. Solution time is (on the 2nd axis) based on the leakage flow rate. As seen in Figure 4.2, the 3rd mesh is the best option in terms of engineering judgment. The 3rd mesh has almost the same leakage flow rate as the 4th and 5th meshes, but can be resolved in a shorter time. Figure 4.3 shows the 2D mesh details of the 3rd mesh.

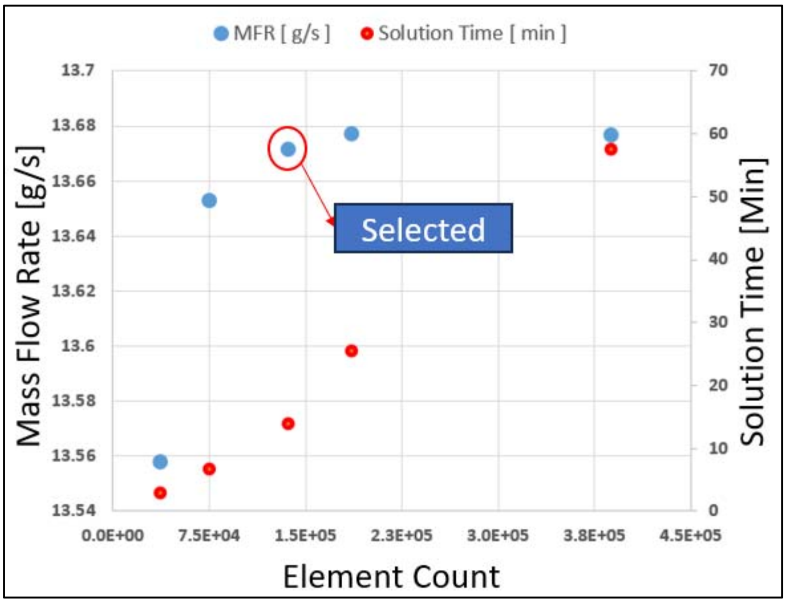

Figure 4.2: Mass Flow Rate and Solution Time with Different Element Counts for Straight Through Labyrinth Seals without Honeycomb Lands

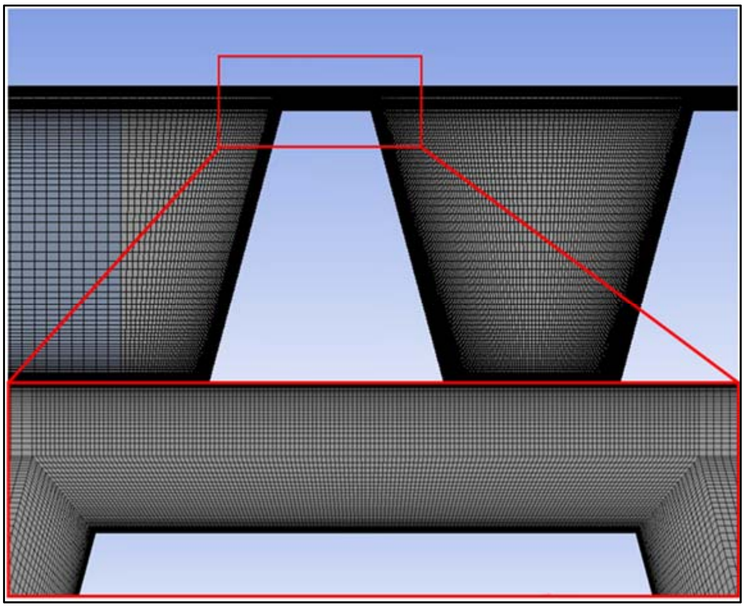

Figure 4.3: Straight Through Labyrinth Seals without Honeycomb Lands 2D Final Mesh

For 3-D analysis, the honeycomb structure must also be meshed correctly. In order to prepare a structured mesh, the the labyrinth seal is divided into two different parts. The first part is for the labyrinth seal and the other part is for the honeycomb land structure. The interface boundary condition is used for the interface between both parts. The closeness of the cell sizes for each part, reduces the numerical error thus dimensions of the elements used in this region are kept close to each other. Mass flow rate are taken main mesh independency parameter for the stationary cases where as the total temperature and the swirl ratio at the exit are also added for the dynamic cases. Figure 4.4 shows mass flow rate and element count comparison. It can be seen that after point 3 there is no significance change in the mass flow rate, but due to y+ requirement point 4 is selected. The mesh structure shown in Figure 4.5 is prepared entirely using structured elements. The region marked in red indicates the interfacial region. In the selected mesh structure, the change of flow properties in the interface region should be as continuous as possible and should not contain non-physical behaviours such as high discontinuity. For this reason, the selected mesh structure was solved and the variation of the axial velocity at the interface plotted for three different lines and it is shown in Figure 4.6. It can be seen that axial velocity along the interfaces are smooth enough thus selected mesh is also appropriate for the interface region. Additionally, it is worth noting that the maximum y+ value is 1.4 for the minimum clearance and maximum pressure ratio, and y+ is generally below 1 in 99% of the grids, ensuring accurate modeling in the wall regions.

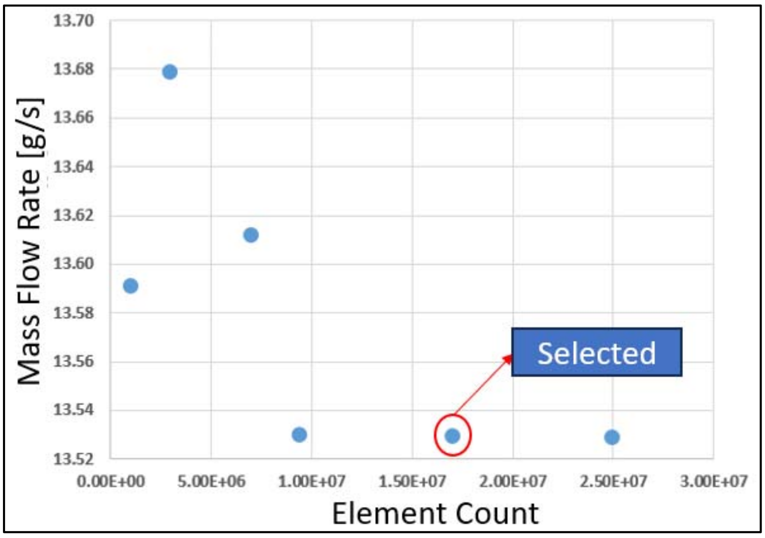

Figure 4.4: Mass Flow Rate with Different Element Counts for Straight Through Labyrinth Seals with Honeycomb Lands

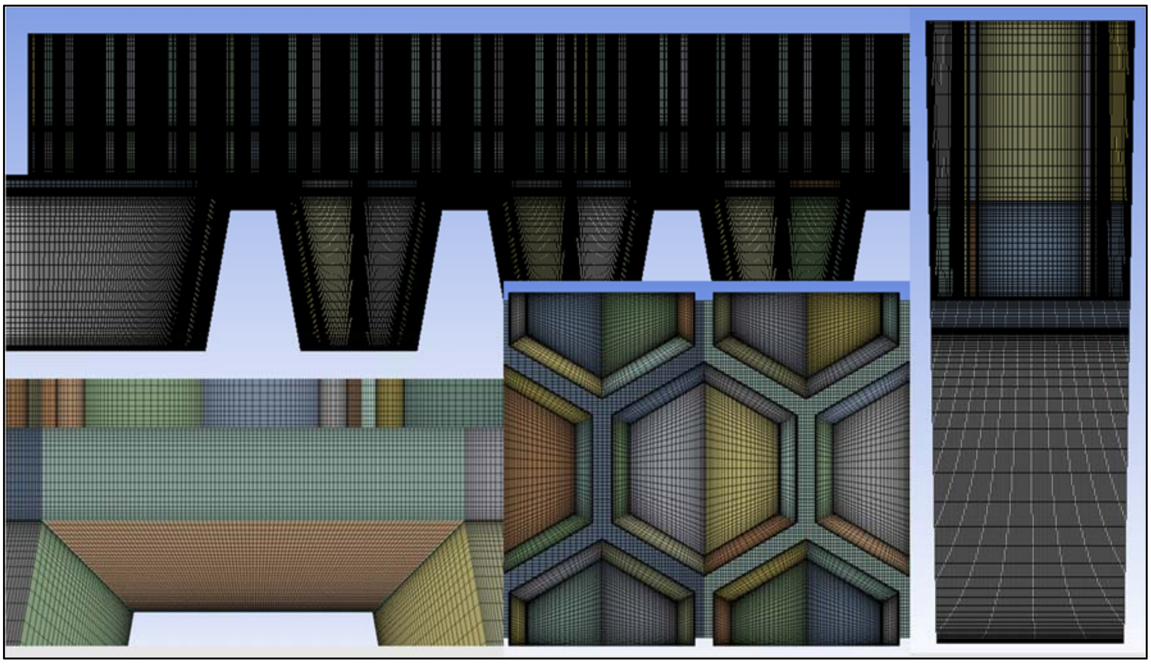

Figure 4.5: Straight Through Labyrinth Seals with Honeycomb Lands 3D Final Mesh

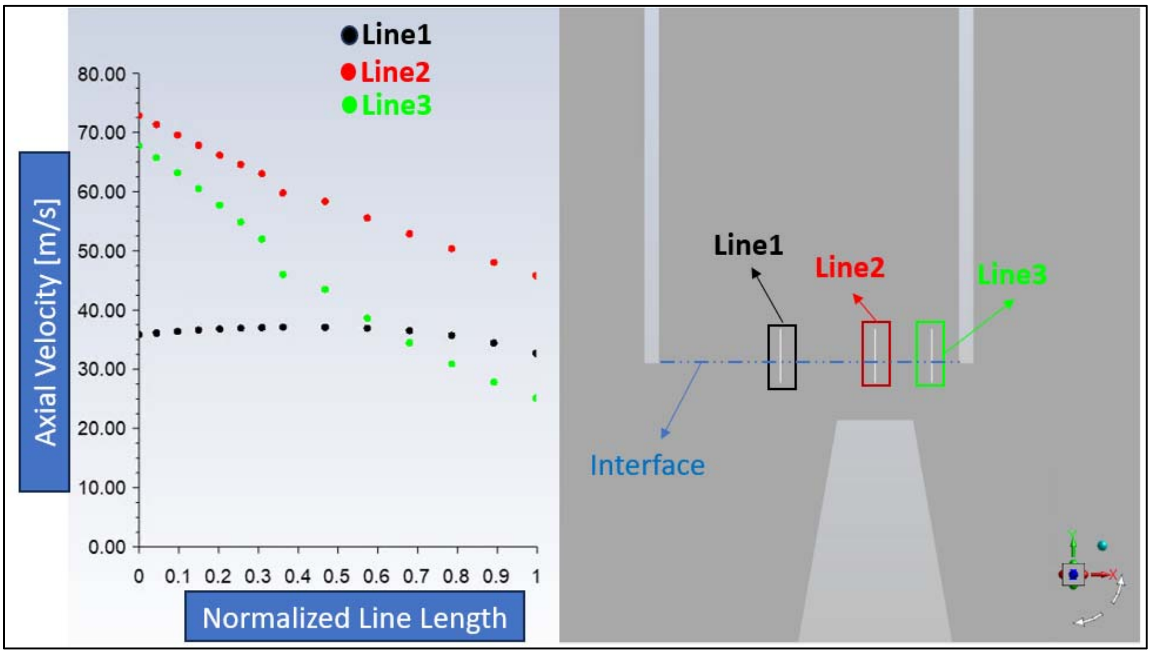

Figure 4.6: Axial Velocity Along the Interface

4.7. Boundary Conditions

Boundary conditions are essential components of CFD simulations as they define how the fluid interacts with the boundaries of the computational domain. The importance of CFD boundary conditions can be understood through several key aspects. Boundary conditions mimic real-world conditions at the boundaries of the computational domain. They help replicate the behavior of fluid flow and heat transfer as they occur in actual systems, making the simulation results more accurate and meaningful. Proper boundary conditions are crucial for achieving accurate and converged simulation results. Incorrect or poorly defined boundary conditions can lead to unrealistic predictions, numerical instability, or difficulties in reaching a converged solution. Inflow boundary conditions prescribe the characteristics of the fluid entering the domain, such as velocity, pressure, and temperature. Outflow conditions define the behavior of the fluid leaving the domain. Accurate inflow and outflow conditions are essential for accurately capturing flow patterns and preventing unphysical reflections of waves. Wall boundary conditions define the interaction between the fluid and solid surfaces. These conditions include no-slip conditions (fluid velocity matches the wall velocity), temperature profiles, and roughness effects. Proper wall treatments are critical for capturing boundary layer behavior and heat transfer at solid surfaces. Symmetry and periodic boundary conditions are used when only a portion of the domain needs to be simulated. These conditions reduce computational costs and enable the study of flow phenomena in a smaller domain while preserving the relevant physics. Table 4.3 shows the boundary conditions used in labyrinth seal for with and without honeycomb analysis. The specified boundary conditions were used in all analyzes in the following sections. Only the parameters whose values need to be changed have been changed, e.g. inlet pressure. Figure 4.7 illustrates the boundary conditions applied in the absence of a honeycomb, while Figure 4.8 depicts the boundary conditions with a honeycomb present within the labyrinth seal. Since the ideal gas is used as the fluid, the energy equations are also solved.

Table 4.3: Boundary Conditions for Labyrinth Seals

Boundary Conditions	
Inlet	Total Pressure [Pa] and Total Temperature [K] with %5 Turbulence Intensity and %10 Turbulence Viscosity Ratio
Outlet	Static Pressure [Pa]
Dummy Walls	Adiabatic with Slip Wall Condition
Walls	Adiabatic with No Slip & Rotational (RPM) & Periodicity (3D)

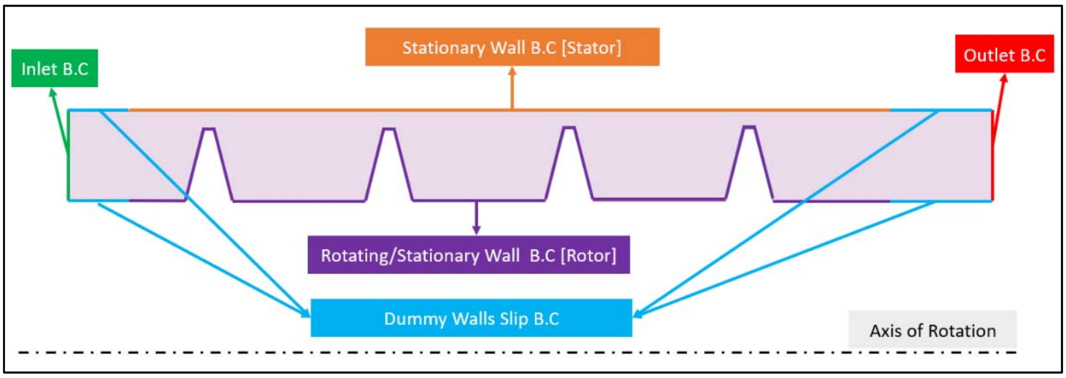

Figure 4.7: 2D Straight Through Labyrinth Seal without Honeycomb Land Axisymmetric Model Boundary Condition Details

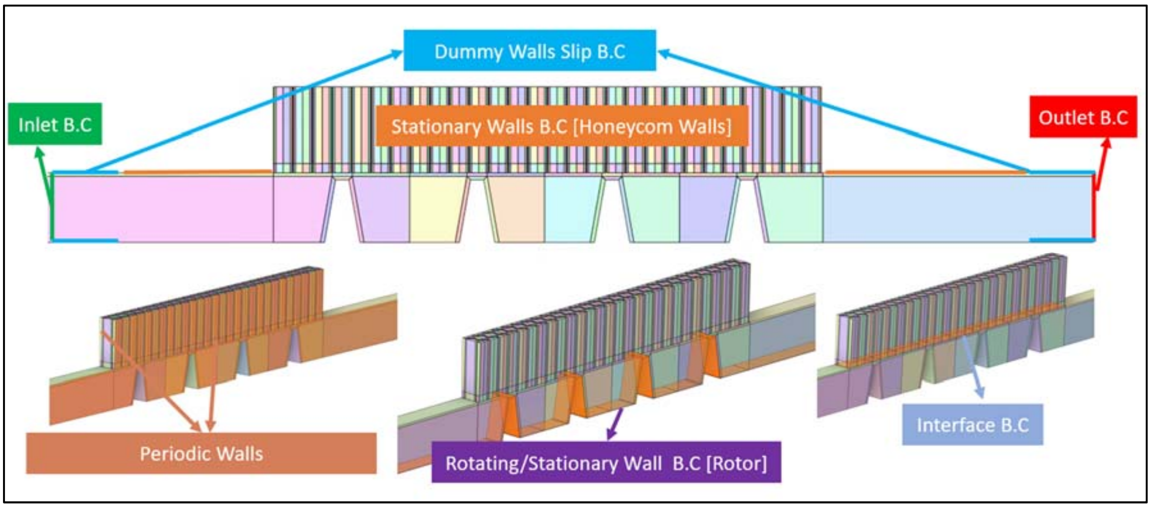

Figure 4.8: 3D Straight Through Labyrinth Seal with Honeycomb Land Boundary Condition Details

4.8. Numerical Convergence

Numerical convergence in CFD analysis is the process of ensuring that the solution to the governing equations is accurate and independent of the discretization of the domain. There are two main types of convergence in CFD analysis:

- Spatial convergence is achieved by increasing the number of grid cells. This reduces the discretization error, which is the error introduced by discretizing the governing equations.
- Temporal convergence is achieved by decreasing the time step. This reduces the numerical error, which is the error introduced by solving the governing equations over a finite time interval.

Only steady-state analyzes were performed in this research so spatial convergence type was followed and mesh independency study has been done which is shown in the following section. Since residuals not enough to ensure convergence in CFD analysis, some interested flow field properties such as mass flow rate, swirl ratio, total temperature (It varies according to the type of analysis) also tracked with different locations. Figure 4.9 represents the 2D axisymmetric geometry and tracked locations properties for to ensure numerical convergence satisfied. The mass-weighted average was used to obtain flow properties and for the 2-D static and dynamic analyzes, the convergence criteria shown in Table 4.4 were examined. For 3D analysis, same process used, however "plane" was used instead of "line".

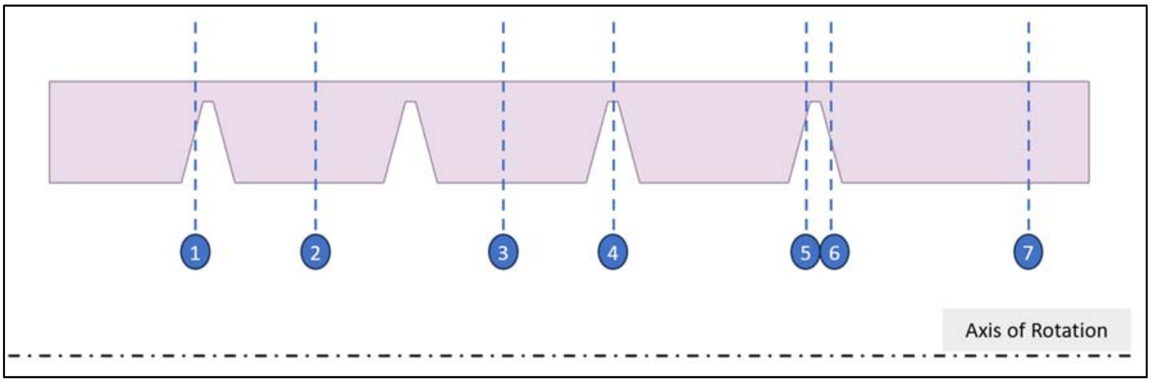

Figure 4.9: 2D Axisymmetric Geometry Numerical Convergence Tracked Flow Properties Locations

Table 4.4: Convergence Criteria Definitions

Location	**Model Type**	**Tracked Property**	**Convergence Level**
1,3,4,5,6	2D Axisymmetric Static	Axial Velocity	1e-6
2		Static Pressure	
7		Mass Flow Rate	
1,4,5,6	2D Axisymmetric Dynamic	Axial Velocity	1e-6
7		Mass Flow Rate & Swirl Ratio & Total Temperature	
2,3		Static Pressure	

5. PROBLEM DESCRIPTION AND VALIDATION

Two different problems were introduced, and each problem was subsequently solved and examined in detail in the following sections. Firstly, conventional straight-through labyrinth seals were analyzed in both 2D and 3D as static cases without a honeycomb structure, utilizing the axisymmetric approach for the 2D analyses. Next, the effect of rotation was investigated without the honeycomb structure, and 2D axisymmetric analyses were solved with the swirl approach, as explained in the numerical method section. Lastly, the honeycomb structure was added to the labyrinth seals, and both static and dynamic 3D analyses were performed to examine the leakage flow rate, swirl, and windage heating effects. Additionally, the flow field was thoroughly discussed in great detail for each problem. A summary of the problems examined is provided in Table 5.1.

Table 5.1: Problem Types

Dimension	Type	Honeycomb Lands
2-D	Static Axisymmetric	No
2-D	Dynamic Axisymmetric with swirl	No
3-D	Static Periodic	Yes

In the 2-D and 3-D static analyses without honeycomb lands, the main objective is to improve the Zimmerman-Wolff equation to calculate the leakage flow more accurately in line with the experimental findings. Firstly, a sensitivity study has been conducted to understand the important parameters that affect the leakage flow. Then, various analysis matrices have been solved, and the flow field was examined in detail. Additionally, k-ε Realizable and k- ω SST turbulence models have been investigated and compared with the experiments. Furthermore, the numerical model was verified through various validation studies towards to end the improved one-dimensional correlation was compared with experimental results and random CFD analysis.

5.1. Comparison of Leakage with Experimental and 2D Numerical Models

Before commencing the development of the CFD-based correlation, it is essential to verify the numerical model through comparisons with existing literature studies and experimental data. In the following sections, 2D numerical models were created and solved for each comparative case, with a specific focus on leakage flow. Three different studies were examined, including Stocker experiments [18], TEI experiments, and the work by Dogu et al. [29] from the open literature.

5.2. Stocker Experiment Comparison with 2D Numerical Model

Experimental studies on labyrinth seals with and without honeycomb lands were conducted by Stocker. 2D Axisymmetric model dimension position given with Figure 5.1 and the values are given with Table 5.2. The tooth thickness was not clearly specified, so a value of 0.31 mm, which is the average of the given range, was used in the CFD analyses. The flow function was used as the comparison parameter. Three different clearance values were compared and for the mesh independence strategy, solution scheme and boundary conditions described in the sections 4.7, and an example of the final mesh is shown in Figure 5.2. The results are presented Table 5.3, Table 5.4 and Table 5.5 respectively. In order to calculate the deviation between the experiments and the computed values equation 5.1 was used.

$$Err = \frac{Compared\ Value - Computed\ Value}{Compared\ Value} \qquad 5.1$$

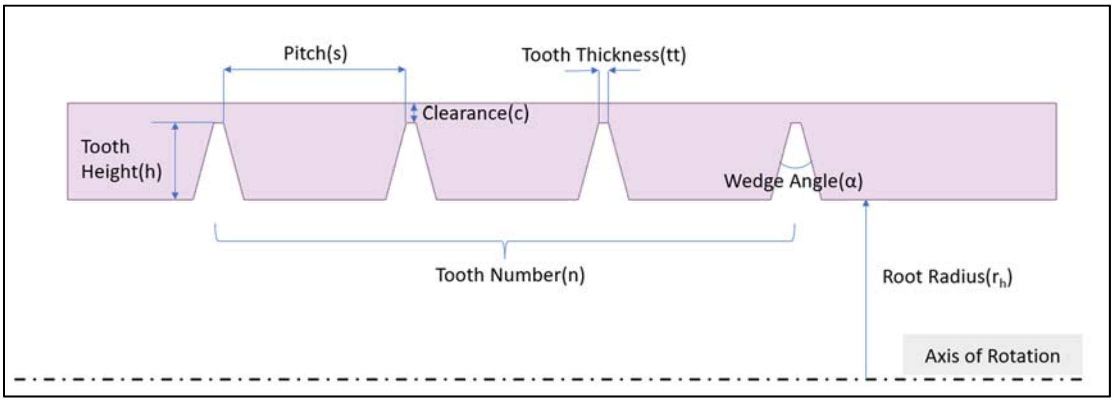

Figure 5.1: Stocker Geometry Parameters

Table 5.2: Stocker Labyrinth Seal Geometrical Parameters

Parameter	Value
Clearance [mm]	0.127- 0.254 - 0.508
Pitch [mm]	2.794
Tooth Height [mm]	2.794
Tooth Number	4
Tooth Wedge Angle [°]	20
Tooth Thickness [mm]	0.250-0.381
Root Radius [mm]	160

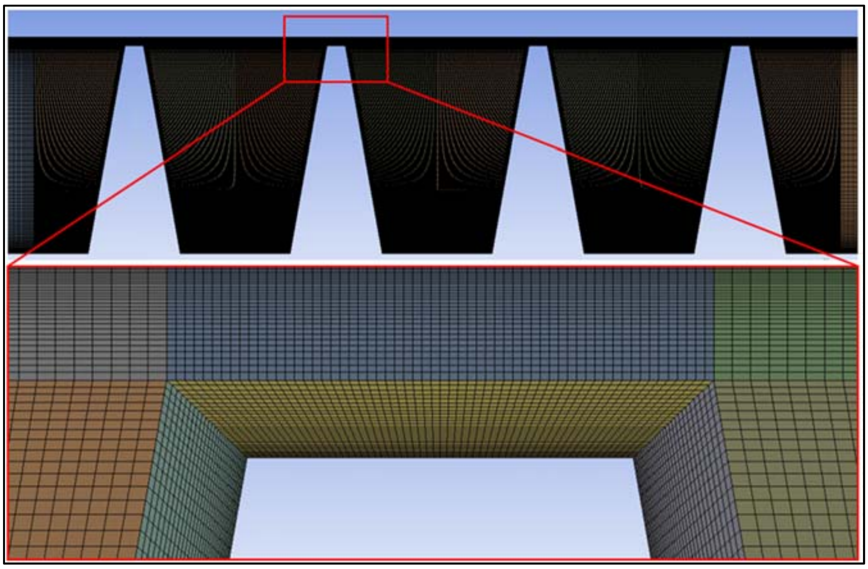

Figure 5.2: Final Mesh Example for Stocker Numerical Model

Table 5.3: Stocker 0.127 mm Clearance Flow Function Comparison with Computed CFD

Clearance [mm]	Pressure Ratio	Φ K-ε Realizable	% Err K-ε Realizable	Φ K- ω SST	% Err K- ω SST	Φ Stocker
0.127	1.19	0.013	16.79	0.0156	3.57	0.016
	1.30	0.016	21.78	0.0185	9.50	0.020
	1.50	0.019	21.68	0.0217	10.17	0.024
	2.00	0.021	22.22	0.0250	9.88	0.027

Table 5.4: Stocker 0.254 mm Clearance Flow Function Comparison with Computed CFD

Clearance [mm]	Pressure Ratio	Φ K-ε Realizable	% Err K-ε Realizable	Φ K- ω SST	% Err K- ω SST	Φ Stocker
0.254	1.30	0.0196	2.00	0.0211	7.25	0.0200
	1.50	0.0230	2.54	0.0240	3.24	0.0236
	2.00	0.0251	3.46	0.0260	3.05	0.0268

Table 5.5: Stocker 0.508 mm Clearance Flow Function Comparison with Computed CFD

Clearance [mm]	Pressure Ratio	Φ K-ε Realizable	% Err K-ε Realizable	Φ K- ω SST	% Err K- ω SST	Φ Stocker
0.508	1.30	0.0245	16.80	0.0257	22.50	0.0210
	1.50	0.0280	16.82	0.0289	20.37	0.0240
	2.00	0.0321	13.42	0.0330	16.61	0.0283

When the computed analysis results were compared with Stocker experiments, it was seen that the k-ε Realizable turbulence model had an error of 20% at 0.127 mm clerance values, however the k-ω SST turbulence model was usualy below 10%. For high clearance value with 0.508 mm clearance still k-ε Realizable closer to the experimental result but it can reach up to 16.82% error. There may be errors of up to 5% during the transfer of experimental results to numerical values. This is due to the poor quality of the document.

In the Stocker experimental study, there is no detailed information about the flow field, since no measurement was made other than the flow rate. In Figure 5.3 CFD results can be seen and the fluid accelerated with the vena contract effect in the entrance area thus static pressure is decreases and velocity increases. Taking into consideration that a portion of the total pressure is lost due to irreversibility, the static pressure decreases as a result of the amplified dynamic pressure caused by the increase in velocity. Consequently, this reduction in static pressure leads to a decrease in the fluid's density. Most of the fluid exiting the tooth tip moves in close proximity to the stator surface, ultimately reaching the last tooth and exiting the system. However, a portion of the fluid enters the cavities and becomes part of the vortex flow. Indeed, what should be emphasized here is that the accurate calculation of the separated boundary layer during the initial interaction has an impact on both the pressure loss in the first stage and the behavior of the fluid in subsequent stages.

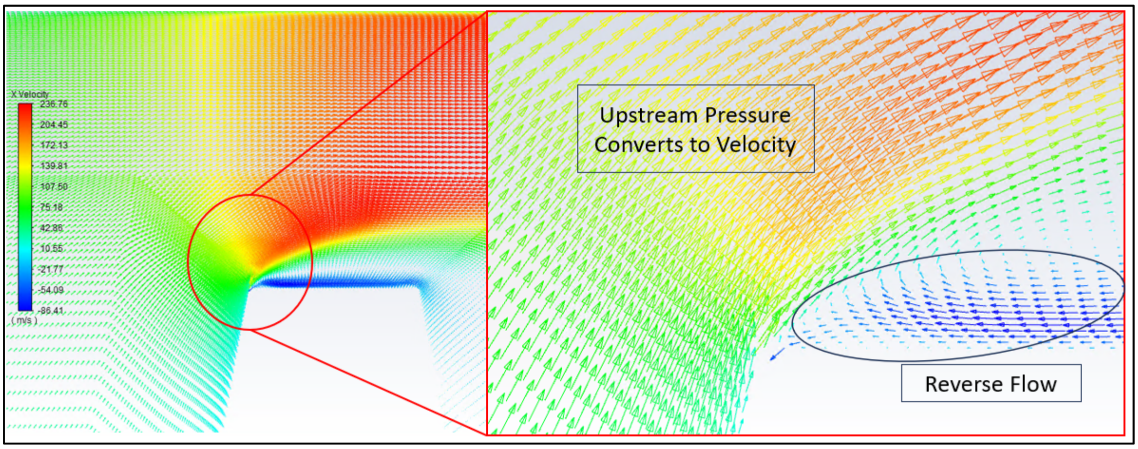

Figure 5.3: 0.508 mm Clearance and 1.5 Pressure Ratio with k-ε Realizable Turbulence Model Axial Velocity Vectors

The static pressure distribution across the labyrinth seal is depicted in Figure 5.4. Notably, the most significant reduction in static pressure occurs at the first tooth. This phenomenon primarily stems from the orifice effect. Initially, the flow area at the first teeth decreases abruptly, causing a substantial increase in velocity. This heightened velocity, in turn, leads to a sudden decrease in static pressure within the vena contracta region.

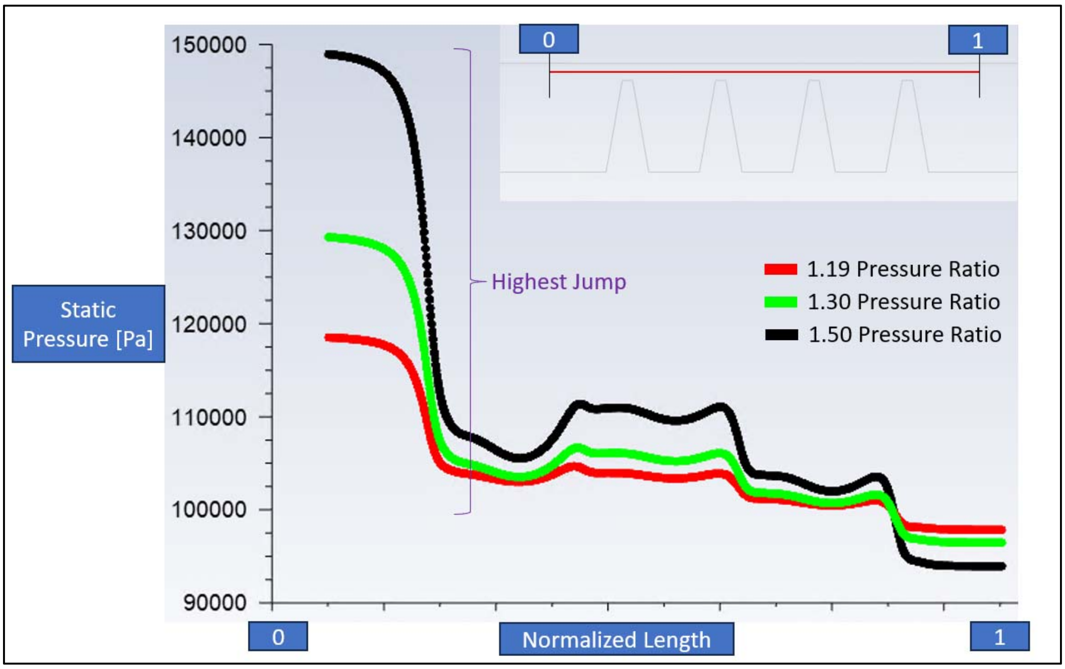

Figure 5.4: 0.508 mm Clearance and 1.5 Pressure Ratio with k-ε Realizable Turbulence Model Static Pressure Drop Along the Labyrinth Seal

The Flow Function can be expressed for various two-dimensional flows and proves valuable for plotting streamlines, outlet lines, and trajectories that illustrate the paths of particles in steady flow. Upon examining Figure 5.5, it becomes evident that the vortex regions and the jet flow area within the labyrinth felt are clearly discernible. Figure 5.6 shows the change in Mach number. The sudden acceleration of the fluid in the jet region caused it to reach up to Mach 0.73. This value is lower in gas turbine engines due to higher temperature conditions thus mach number is generally around 0.5.

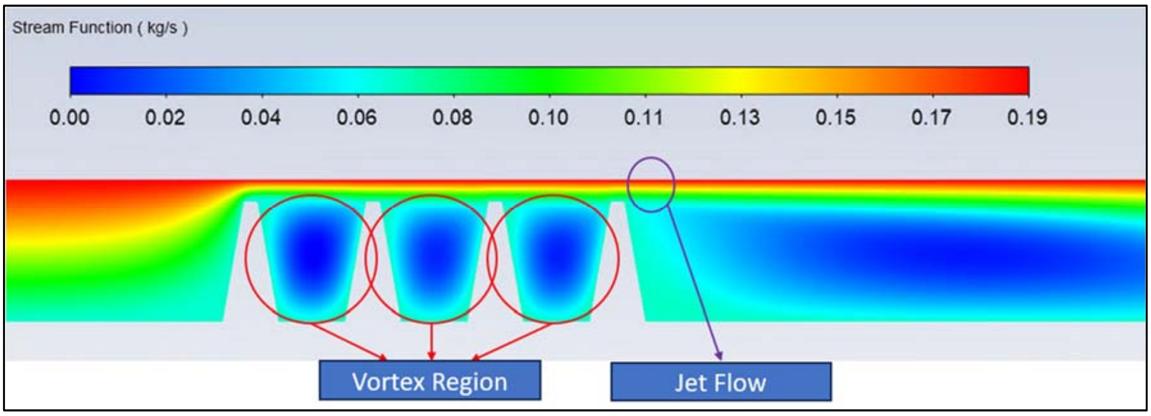

Figure 5.5 Labyrinth Seal Stream Function Contour

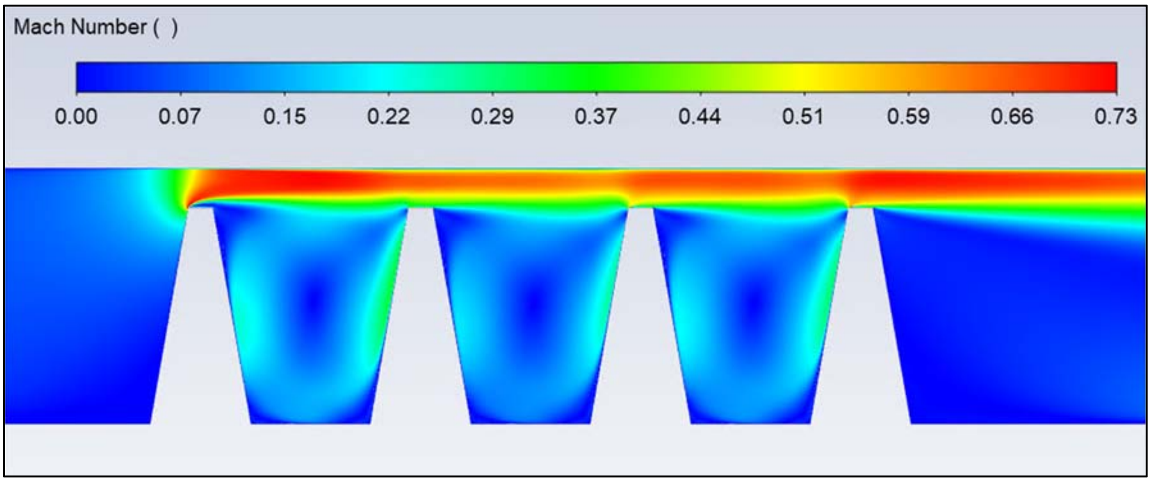

Figure 5.6 Labyrinth Seal Mach Number Contour

5.3. TEI Experiment Comparison with 2D Numerical Model

The tests conducted within the TEI were detailed in section 3. A comparison was made, and critical aspects were highlighted in connection with the one-dimensional Zimmerman-Wolff correlation. This section provides a comprehensive analysis of the results obtained from the numerical model, utilizing the internal k-ε Realizable and k-ω SST turbulence models. Since the flow field is similar to the previous section, it has not been examined again. The purpose here is to just observe the amount of leakage flow obtained by the two different turbulence models used. The results of the tightest clearance with different tooth thicknesses are shown in Figure 5.7, Figure 5.8 and Figure 5.9. It has been observed that the Cd trend is quite in agreement with both turbulence models. However, it was seen that the k- ω SST Turbulence model was more compatible with the experimental results in general.

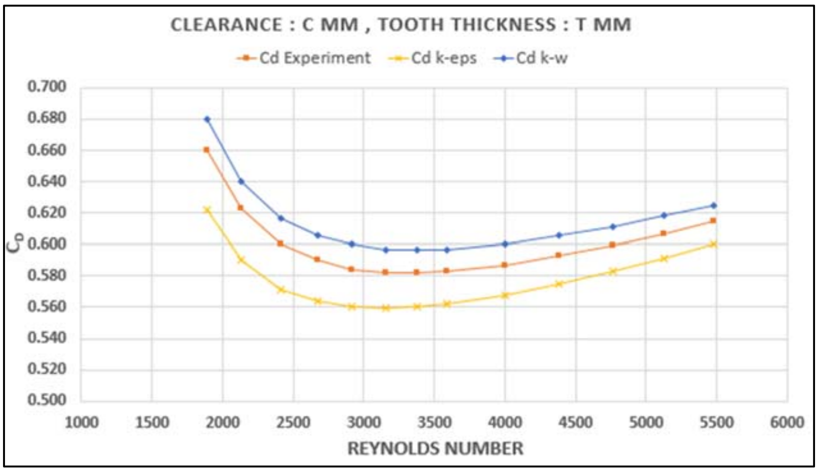

Figure 5.7: Axial Reynolds Number and Discharge Coefficient Comparison with C mm Clearance and T mm Tooth Thickness for the Experiment, k- ε Realizable and k- ω SST Turbulence Model

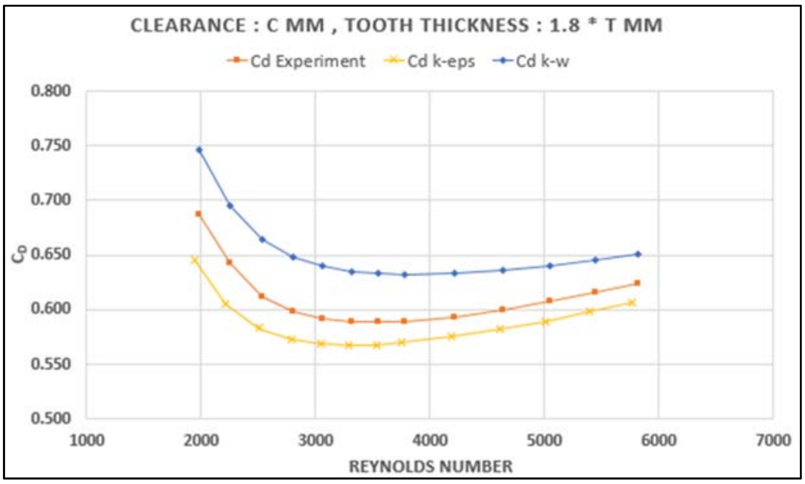

Figure 5.8: Axial Reynolds Number and Discharge Coefficient Comparison with C mm Clearance and 1.8 * T mm Tooth Thickness for the Experiment, k- ε Realizable and k- ω SST Turbulence Model

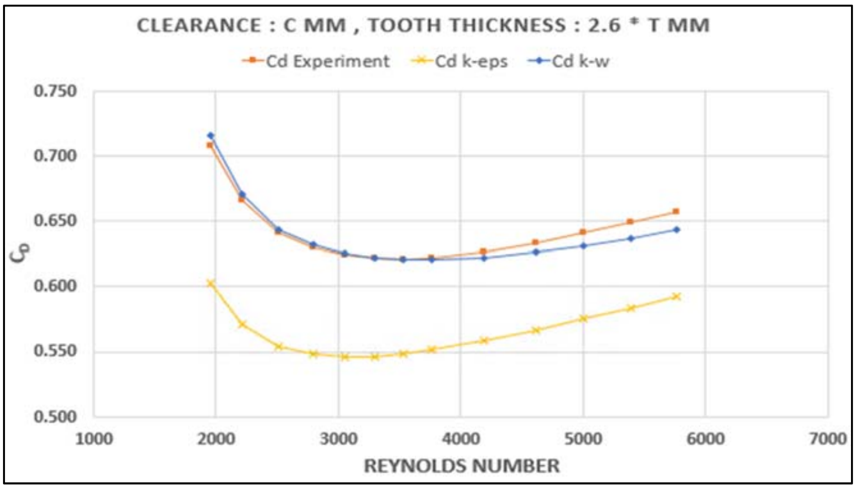

Figure 5.9: Axial Reynolds Number and Discharge Coefficient Comparison with C mm Clearance and 2.6 * T mm Tooth Thickness for the Experiment, k- ε Realizable and k- ω SST Turbulence Model

The clearance has been slightly increased and the numerical models have been re-solved. The results obtained are given in Figure 5.10, Figure 5.11 and Figure 5.12. Again, The Cd trend is in agreement with the experimental results. It has been observed that the k- ω SST Turbulence model is generally closer to the experimental results.

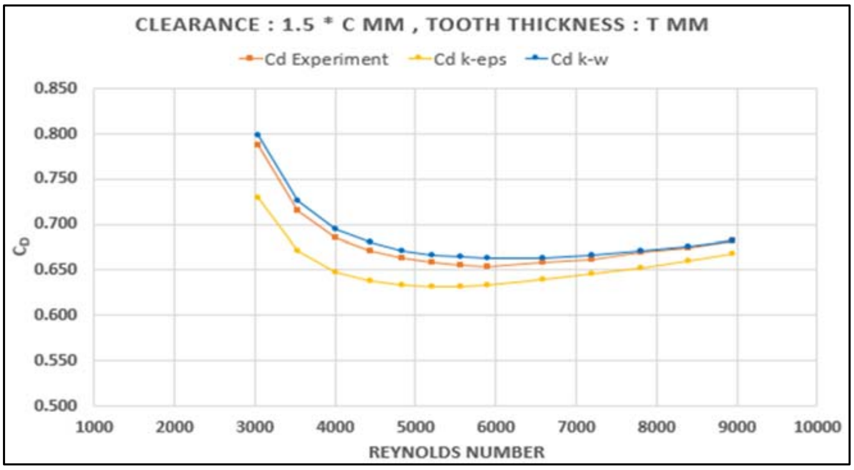

Figure 5.10: Axial Reynolds Number and Discharge Coefficient Comparison with 1.5 * C mm Clearance and T mm Tooth Thickness for the Experiment, k- ε Realizable and k- ω SST Turbulence Model

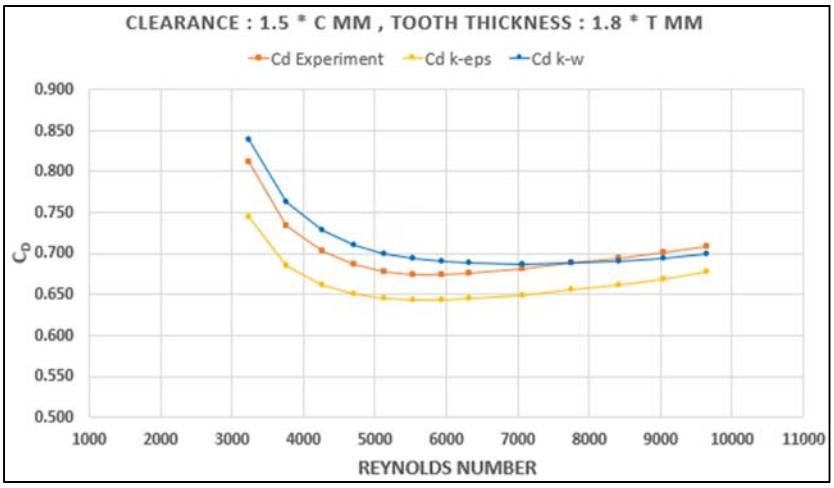

Figure 5.11: Axial Reynolds Number and Discharge Coefficient Comparison with 1.5 * C mm Clearance and 1.8 * T mm Tooth Thickness for the Experiment, k- ε Realizable and k- ω SST Turbulence Model

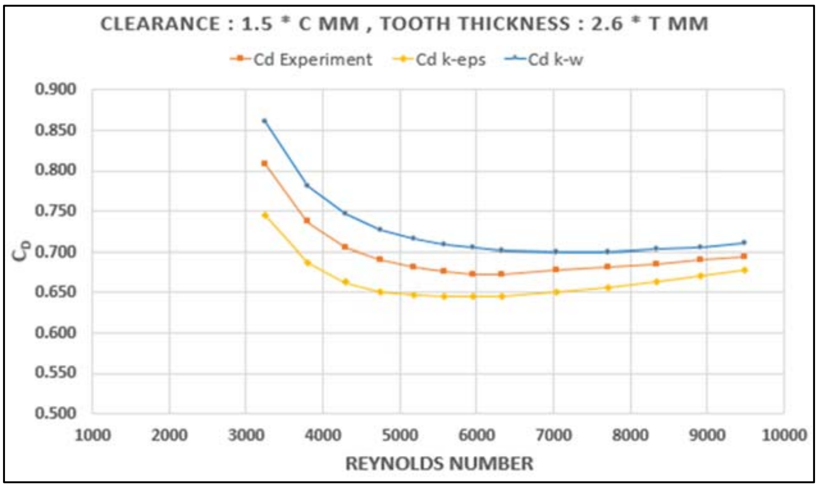

Figure 5.12: Axial Reynolds Number and Discharge Coefficient Comparison with 1.5 * C mm Clearance and 2.6 * T mm Tooth Thickness for the Experiment, k- ε Realizable and k- ω SST Turbulence Model

Finally, analyzes were performed again for the highest clearances. The results are shown in Figure 5.10, Figure 5.11 and Figure 5.12. When the results are examined, the k-ε Realizable turbulence model instead of the k- ω SST turbulence model is now quite compatible with the experimental results.

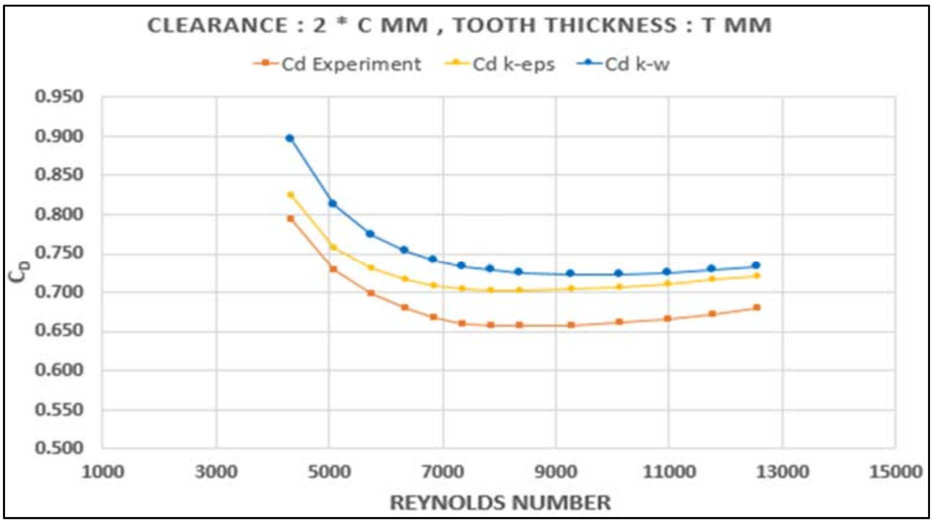

Figure 5.13: Axial Reynolds Number and Discharge Coefficient Comparison with 2 * C mm Clearance and T mm Tooth Thickness for the Experiment, k- ε Realizable and k- ω SST Turbulence Model

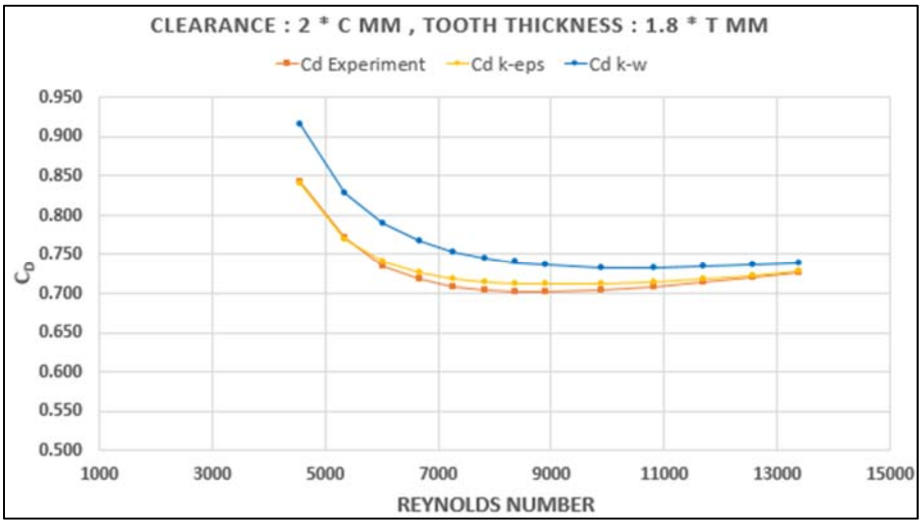

Figure 5.14: Axial Reynolds Number and Discharge Coefficient Comparison with 2 * C mm Clearance and 1.8 * T mm Tooth Thickness for the Experiment, k- ε Realizable and k- ω SST Turbulence Model

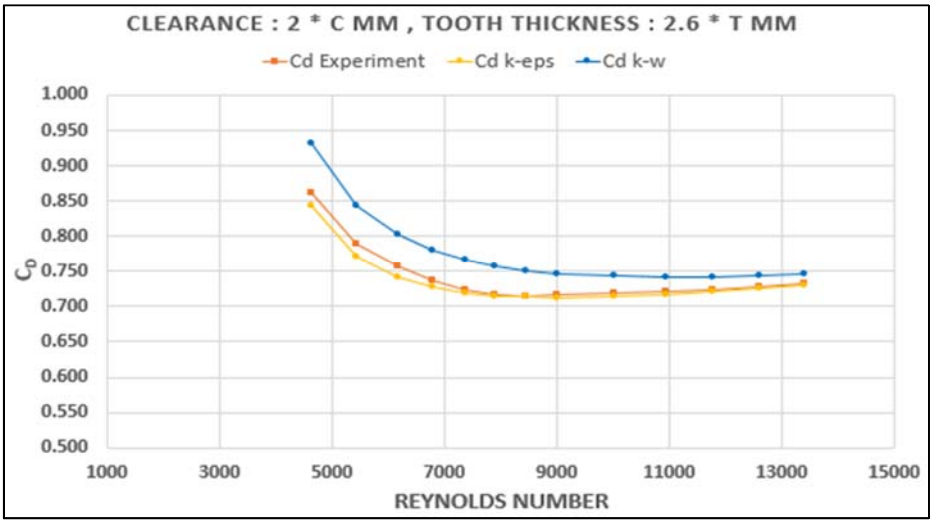

Figure 5.15: Axial Reynolds Number and Discharge Coefficient Comparison with 2 * C mm Clearance and 2.6 * T mm Tooth Thickness for the Experiment, k- ε Realizable and k- ω SST Turbulence Model

Upon reviewing the outcomes from both turbulence models across various clearances and tooth thicknesses, a consistent C_d trend was generally observed. However, it became evident that adjustments to the turbulence model were necessary to attain values that closely aligned with experimental results. In order to understand the difference between k-ε Realizable and k- ω SST turbulence models, more detailed studies are done in the following sections.

5.4. Literature Comparison with 2D Numerical Model

The numerical study conducted by Doğu et al. [29] was utilized, as it provides a clear summary of the geometry and boundary conditions. The geometric features details for this study are readily available from their study and its shown with Figure 5.16. The flow field were investigated for 1.5, 2.5 and 3.5 pressure ratios with 0 RPM.

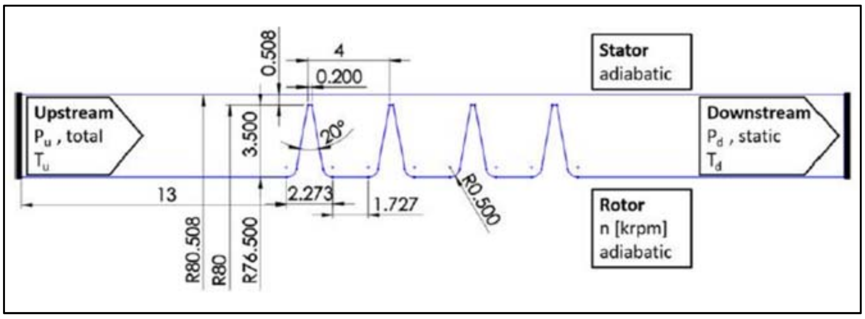

Figure 5.16: Analysis Geometry from Dogu et al.

The flow function was used to compare analyzes which is defined in introduction section. The mesh independence and analysis solution scheme were used as described in the numerical model section. Fillet radii at the root of the rotor were not modeled because it has negligible effect and main parametric model needs to be preserved. The flow coefficient results are shown in

Table 5.6. The velocity contours for two different turbulence models are depicted in Figure 5.17. Noticeably distinct velocities were calculated within the initial vena contracta region for these two models. This discrepancy in velocities carried through to subsequent stages, resulting in varying rates of leakage flow. This difference is related with the different turbulence model coefficients used in the boundary layer solution.

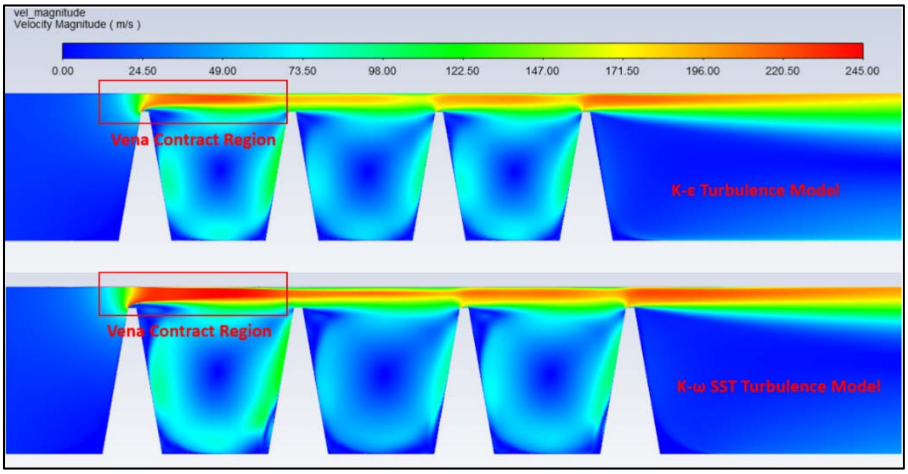

Figure 5.17: Velocity Magnitude Contour of k-ε Realizable and k- ω SST Turbulence Models at 1.5 Pressure Ratio

Table 5.6: Literature Study Flow Coefficient Results for Different Pressure Ratios with k-ε Realizable and k- ω SST Turbulence Models

Pressure Ratio	Φ K-ε Realizable	Φ K- ω SST	Φ Literature
1.50	0.0256	0.0265	0.0250
2.50	0.0295	0.0296	0.0290
3.50	0.0299	0.0300	0.0295

When the results of the analysis were examined, the following results were obtained.

- The k-ε Realizable turbulence model obtained less leakage flow compare to the k-ω SST turbulence model and was more compatible with the literature. The main reason for this is the literature study used the k-ε turbulence model in the analysis.
- It was determined that at low pressure ratios, the k-ε Realizable and k-ω SST turbulence models flow field were different in the 1st tooth location and this affects the leakage flow rate significantly.
- The analysis in the literature was not confirmed by any experimental data, thus which turbulence model is suitable in the real not known but comparison of CFD demonstrates the suitability of the methodology which was used in this thesis.

5.5. Comparison of Leakage, Swirl and Windage Heating

In this section, a numerical model prepared for the validation of labyrinth seal which is used in compressor sealing and was studied in 2016 both numerically and experimentally by Kong et al. [25] Kong et al. focused on investigating the flow characteristics and temperature effects in the stator well of a compressor. They utilized a test rig with varying rotational speeds and pressure ratios, designed based on a simplified model of the labyrinth seal. By measuring the leakage flow rate, change in total temperature, and swirl ratios, they aimed to understand the swirl development and the precise working tip clearance. Additionally, they conducted 2D, axisymmetric numerical simulations to further analyze the flow characteristics and compared the computational results with the experimental measurements, specifically in terms of discharge coefficient, windage heating, and swirl ratio. Figure 5.18 shows the experiment measurement locations and Figure 5.19 represents the geometry with dimensions.

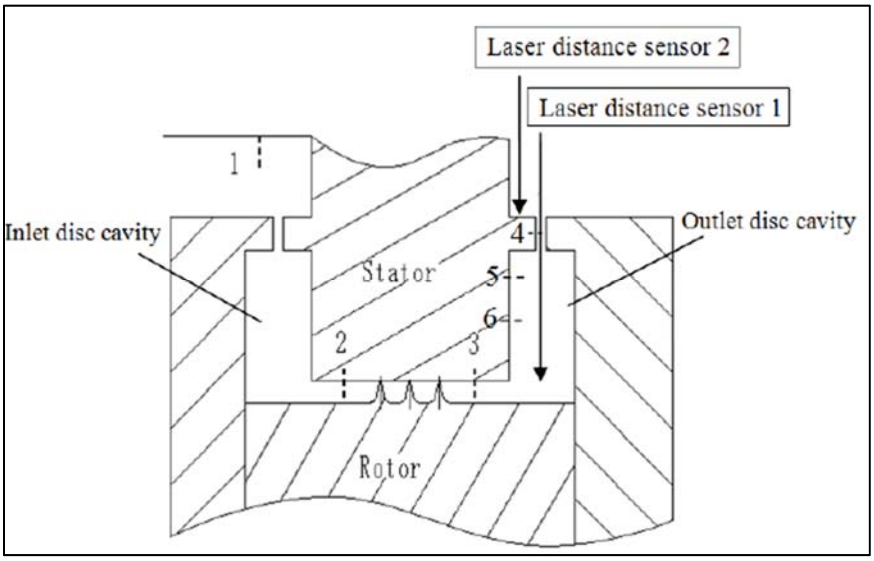

Figure 5.18: Experimental Setup Measurement Distributions

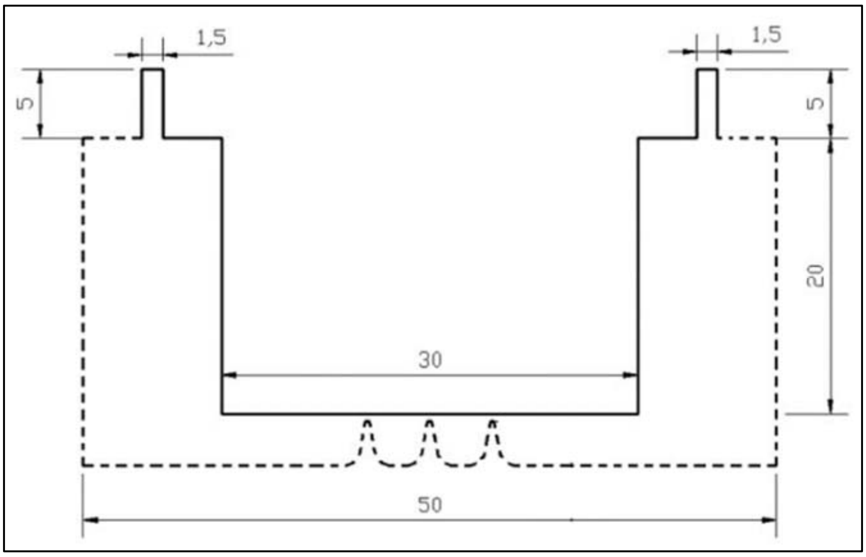

Figure 5.19: Numerical Model Dimensions for Kong.et al[30]

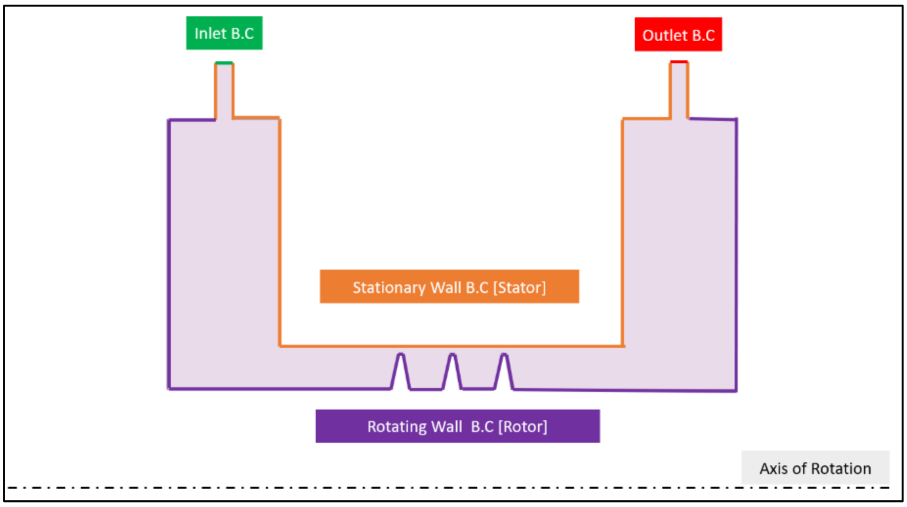

Figure 5.20: Numerical Model Boundary Condition Locations

Table 5.7: Numerical Model Boundary Condition Values

Location	Boundary Condition	Value
Inlet	Total Pressure Total Temperature	132.000 Pa 300K
Outlet	Static Pressure	120.000 Pa
Rotor	Rotational Wall	5100,6000,6600,7000,7500,8100 RPM
Stator	Stationary Wall	No Slip Condition

In Figure 5.20 locations of boundary conditions are given and in Table 5.7 boundary condition values are shown. Final mesh model has been shown with Figure 5.21. C_d, total temperature at the exit and the swirl ratio has been investigated for the comparison.

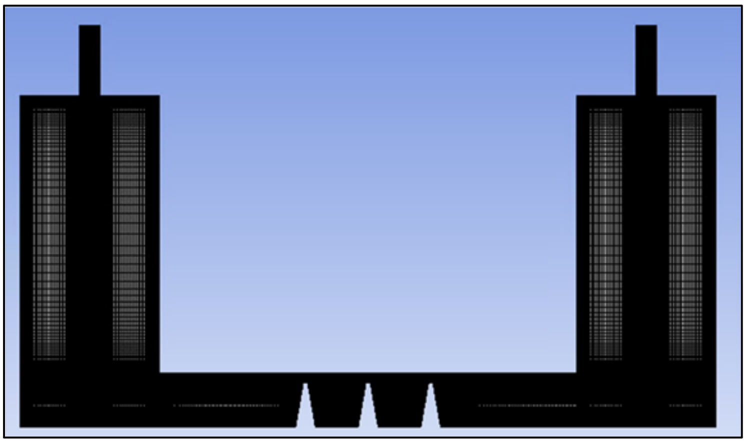

Figure 5.21: Numerical Model Final Mesh

First of all, the amount of leakage flow obtained at different RPMs was calculated. The C_d value obtained using the formula in the Table 1.1 and it was compared with the experimental results. In Figure 5.22 it has been observed that as RPM increases, C_d tends to decrease. The primary reason for this phenomenon is that the rise in tangential velocity component leads to an impact on the axial velocity component, subsequently influencing the flow rate. Consequently, the reduction in the amount of leakage flow occurs, resulting in a decrease in the C_d value.

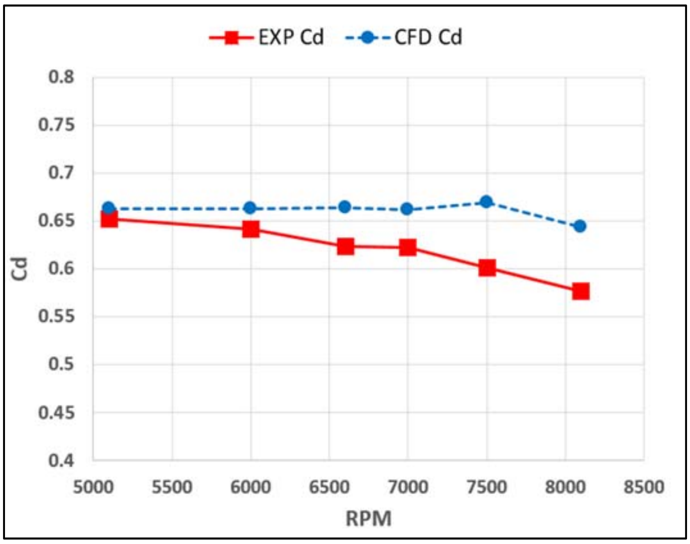

Figure 5.22: Experimental C_d vs CFD C_d for 1.1 PR with variable RPM

Accurately estimating the overall temperature rise is critical for gas turbine engines because thermal expansions will affect the clearances, thus affecting engine performance. In this numerical model viscous work which is generated with the rotational walls causes the total temperature increase and total temperature comparison shown with Figure 5.23, it can be seen that variation almost same but a slightly shifted in temperature. This is mainly explained with adiabatic wall boundary condition in the CFD model. Since heat transfer is restricted in the CFD it is acceptable to find higher temperatures compare to the experiment. Also, as the RPM increase, heat transfer increases and the temperature difference increase accordingly. The comparison for the swirl ratio is given in Figure 5.24 and CFD is in generally good agreement with the experiment. As the rotor speed increases, the tangential velocity of the fluid likewise increases, resulting in a higher swirl ratio. Increasing the swirl ratio of the fluid in the system will indeed enhance turbulence density, consequently leading to an increase in the heat transfer coefficient, which, in turn, results in higher exit temperatures. This validation demonstrates that the results obtained from the computational fluid dynamics (CFD) simulations closely align with the experimental findings in terms of windage heating, swirl ratio, and leakage flow.

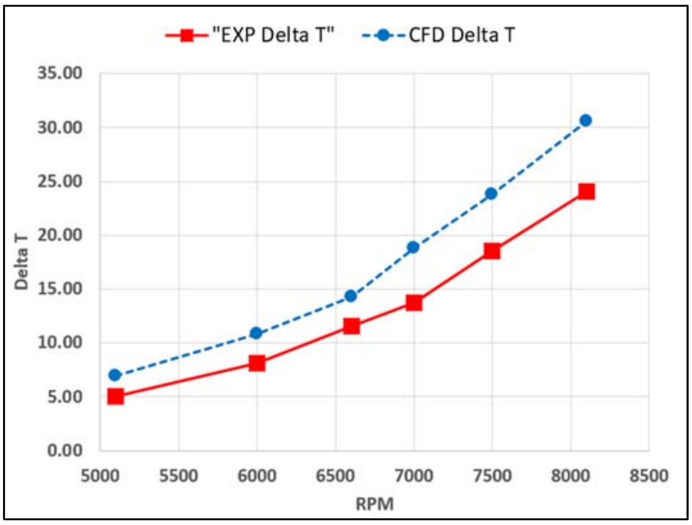

Figure 5.23: Experimental Total Temperature Comparison with CFD for 1.1 PR

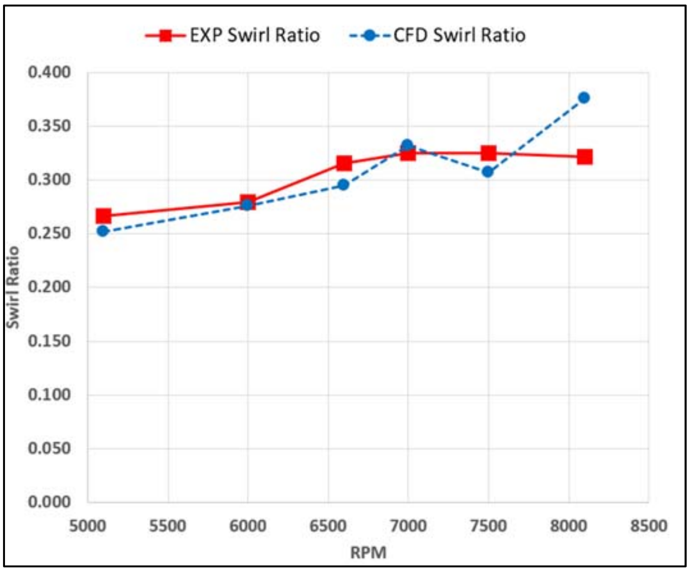

Figure 5.24: Experimental Swirl Ratio Comparison with CFD for 1.1 PR

5.6. Experimental and 3D Numerical Model with Honeycomb Lands

In order to validate 3D numerical model, a study conducted by Stocker [18] was employed. Stocker utilized different honeycomb cell sizes (Hcs) and compared them without honeycomb lands. Comparisons were made for two different clearances and pressure ratios using the 1/32 inc Hcs with numerical modeling approach in section 4. Boundary conditions and the final mesh independency study are followed as in showed in section 4. Flow coefficient has been used for the comparison parameter. The comparison results for 0.254 mm and 0.508 mm clearances are given in Table 5.8 and Table 5.9 respectively.

Table 5.8: 0.254 mm Clearance with 1/32 Honeycomb Cell Size Stocker & Numerical Model Comparison

Clearance [mm]	**Pressure Ratio**	**Φ K-ε Realizable**	**% Err K-ε Realizable**	**Φ K- ω SST**	**% Err K-ω SST**	**Φ Stocker**
0.254	1.30	0.01680	4.01	0.01821	-4.03	0.01751
	1.50	0.01981	2.90	0.02086	-2.22	0.02041

Table 5.9: 0.508 mm Clearance with 1/32 Honeycomb Cell Size Stocker and Numerical Model Flow Coefficient Comparison

Clearance [mm]	**Pressure Ratio**	**Φ K-ε Realizable**	**% Err K-ε Realizable**	**Φ K- ω SST**	**% Err K-ω SST**	**Φ Stocker**
0.508	1.30	0.02050	-9.48	0.02167	-15.70	0.01873
	1.50	0.02353	-9.77	0.02377	-10.90	0.02144

The CFD results were found to be close to the experimental results obtained at a clearance of 0.254 mm. However, at a clearance of 0.508 mm, the k-ε Realizable turbulence model provided the closest result, but the error rate was around 10%. The reduction amount of the honeycomb land on the leakage flow can be defined as the reduction rate by equation 5-2. Reduction rate values are shown in Table 5.10 since analyzes also performed without honeycomb structure in section 5.1.1.

$$Reduction\ Rate = \frac{\dot{m}_{without\ honeycomb} - \dot{m}_{with\ honeycomb}}{\dot{m}_{without\ honeycomb}} \tag{5-2}$$

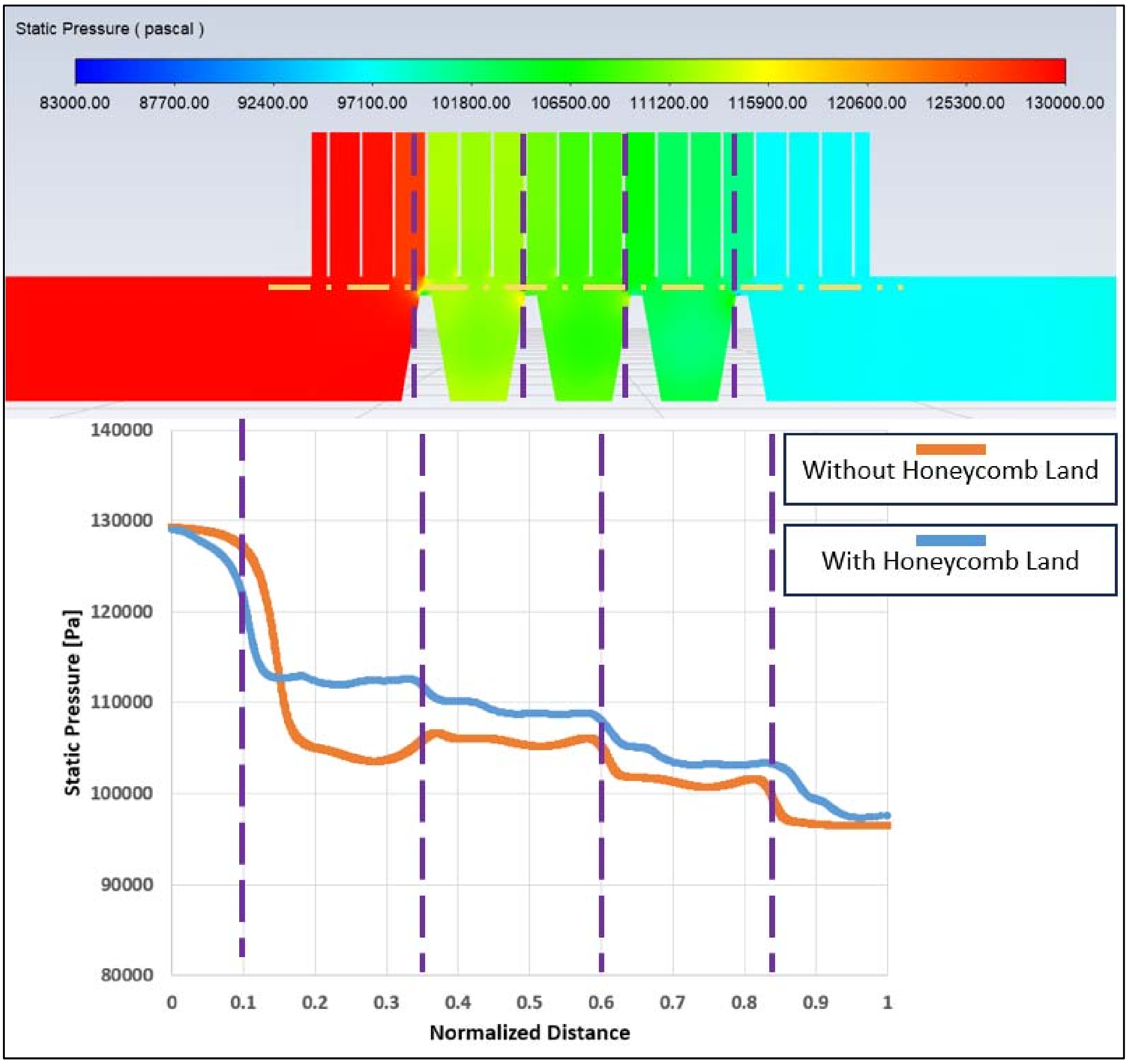

Figure 5.25: Stocker 0.508 mm Clearance Model with and without 1/32 inc Honeycomb Land Static Pressure Distribution

Table 5.10: 0.254 and 0.508 mm Clearance Stocker and Numerical Model Reduction Rate Comparison

Clearance [mm]	**Pressure Ratio**	**Stocker Reduction Rate %**	**K-ε Realizable Reduction Rate %**	**K- ω SST Reduction Rate**
0.254	1.30	10.98	14.09	13.65
	1.50	13.55	13.85	14.40
0.508	1.30	10.72	16.32	15.52
	1.50	10.70	16.09	17.78

When the reduction values obtained for both turbulence models were examined, approximately 5% difference was observed for 0.508 mm clearance. In general, the error rate of the numerical model was found to be below 10% and following results were observed:

1. For a clearance of 0.508 mm without honeycomb land, the k-ε realizable turbulence model overestimated the leakage flow rate by approximately 15%, as indicated in section 5.1.1. However, with honeycomb, the error decreased to about 10%, while still resulting in an overestimated leakage flow rate.
2. With a clearance of 0.254 mm, both turbulence models were in agreement with the Stocker experiment, displaying an error of approximately 4%, both with and without honeycomb land.
3. When considering the reduction rate, close results were obtained for the 0.254 mm clearance configuration. However, a 5% higher reduction rate was calculated using CFD for the 0.508 mm clearance case. The k-ω SST turbulence model consistently predicted higher leakage flow in all analyses, without exception

6. LABYRINTH SEAL WITHOUT HONEYCOMB LAND

In this section, labyrinth seals are examined in detail without honeycomb lands. The existing Zimmerman-Wolff correlation, as shown in equation 2.7, has been refined through the incorporation of experimental studies outlined in section 3, along with CFD-based parametric analyses. Furthermore, the impact of swirl and windage heating number was investigated through a full factorial analysis matrix.

6.1. 2D Axisymmetric Parametric Model

A two-dimensional, fully parametric model has been developed to facilitate parametric simulations using Computational Fluid Dynamics (CFD) for a straight-through labyrinth seal, as shown in Figure 6.1. The yellow section indicates the segment that will be replicated when there's a need to increase the number of teeth. This geometric modeling approach ensures that both the geometry and mesh structure are entirely parametric.

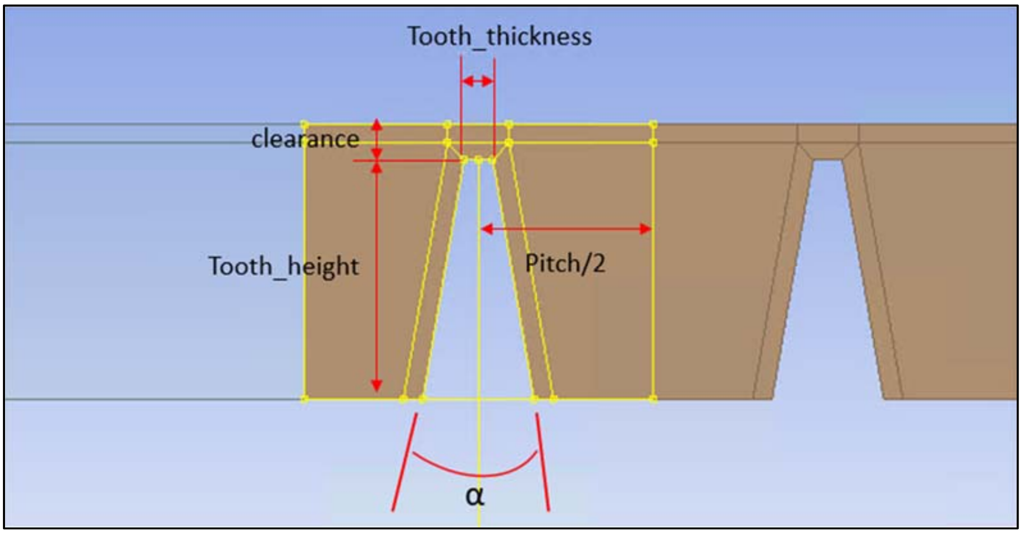

Figure 6.1: Straight Through Labyrinth Seal 2D Axisymmetric Parametric Geometry

6.2. Sensivity Study for Parameter Importance on Leakage Flow Rate

A sensitivity study was conducted to assess the influence of various geometric parameters on the leakage flow of labyrinth seals. The investigation involved a literature search, the utilization of correlated equations, and the consideration of experimental results. It was determined that clearance, pitch, tooth number, and tooth thickness are the primary parameters significantly affecting the leakage flow of labyrinth seals. To ensure mesh independence, a mesh was generated using the same methodology outlined in section 4. The results of the mesh independence study are presented in Figure 6.2, and further details of the mesh configuration are illustrated in Figure 6.3. Within Figure 6.3, the mass flow rate an essential parameter of interest is represented in blue, while the total number of elements is indicated in red. The results clearly demonstrate that the mass flow rate converges after the fifth case, which utilized an approximate total of 990,000 elements. To achieve a converged solution, the same procedure as described in section 4 was followed. Details of full factorial analysis and selected parameters are given in Table 6.1.

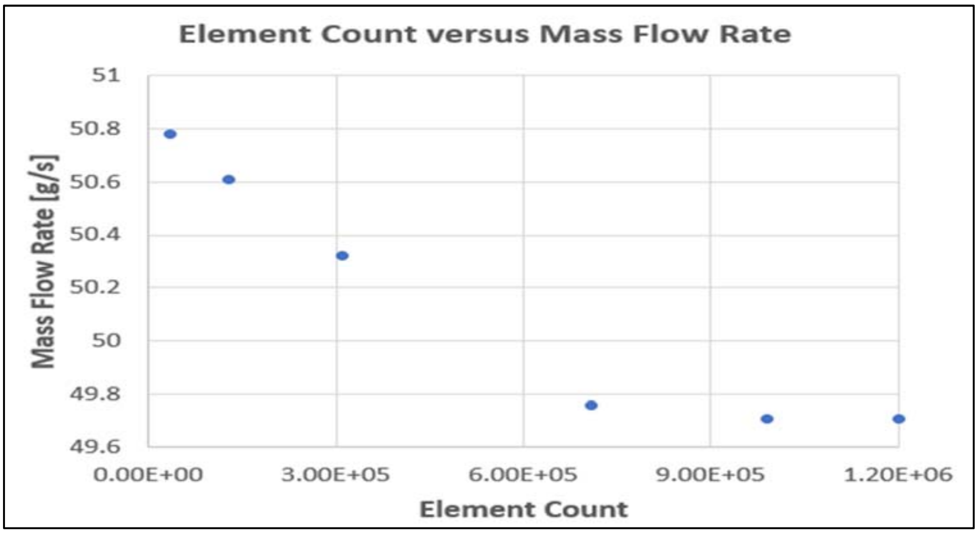

Figure 6.2: Mesh Independency for Sensivity Analysis

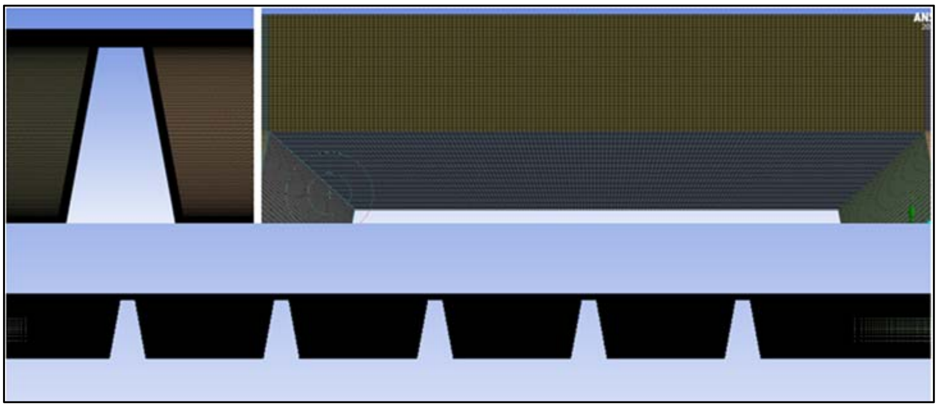

Figure 6.3: Sensivity Study Selected Mesh

Table 6.1: Sensivity Study Parametric Analysis Details

Parameter	Values
Clearance [mm]	0.15-0.30-0.45
Tooth Thickness [mm]	0.4-0.6-0.8
Pitch [mm]	4-6-8
Tooth Number	3-4-5
Tooth Height [mm]	2.794
Tooth Wedge Angle [°]	20°
Root Radius [mm]	40

Clearance, tooth thickness, pitch, and tooth number were identified as the variable parameters. Pressure ratio, tooth height, tooth wedge angle, and root radius were kept constant. Three different values were assigned to each variable parameter, resulting in a total of 81 analyses. The outcomes of these analyses were examined using the Minitab statistical tool to identify the parameters influencing leakage flow. Pareto charts were created for both turbulence models. However, since the results were quite similar and our primary goal is to understand parameter importance, the results from the k-ε realizable turbulence model are presented in Figure 6.4. The findings confirmed the expected dominance of clearance as the key parameter affecting the leakage flow rate. The Pareto chart also revealed that both pitch and tooth number had almost indistinguishable effects. However, this observation should be approached cautiously, considering that increasing the number of teeth could inherently influence the model's size and incorporate certain pitch-related effects into the tooth number effect. This actually shows that the pitch parameter is more effective compared to the tooth number. Therefore, when examining the parameters individually, clearance, pitch, tooth number, and tooth thickness were found to be the significant factors, with clearance having the most significant impact on the leakage flow rate, followed by pitch, tooth number, and tooth thickness.

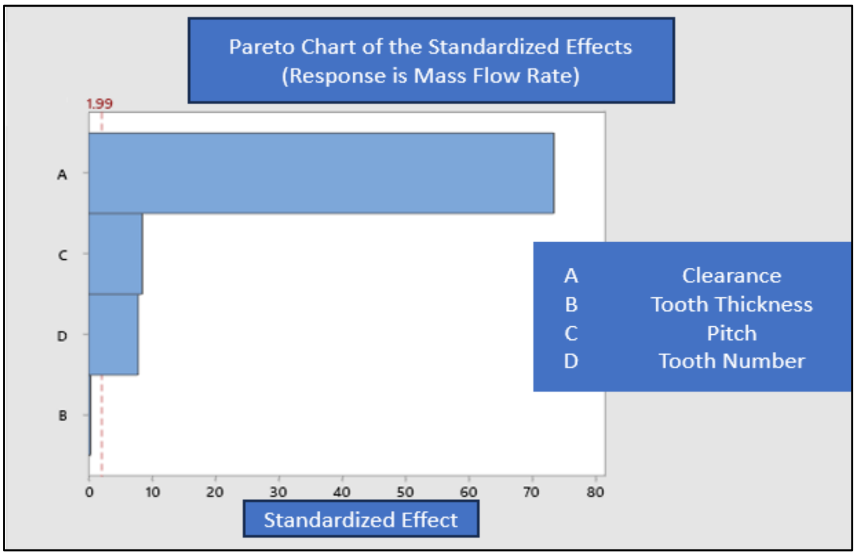

Figure 6.4: Parameter Importance on Leakage Flow Rate for Straight Through Labyrinth Seal with k-ε Realizable Turbulence Model

The subsequent phase involved investigating the cross-effects among the parameters, and the resultant Pareto chart is presented in Figure 6.5. The analysis unveiled that the interactions between clearance/tooth thickness and pitch/clearance had a more pronounced impact on the leakage flow rate compared to the number of teeth.

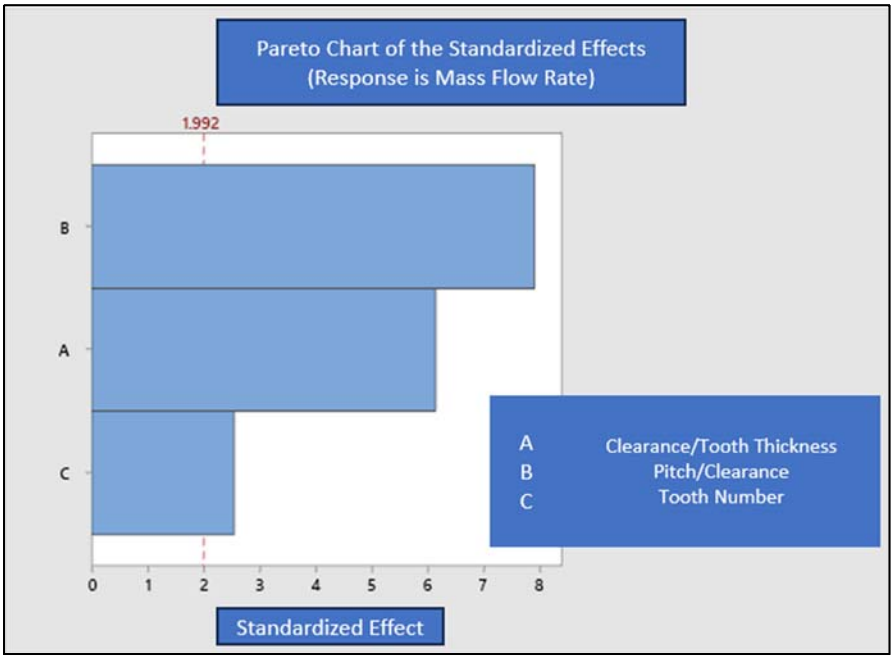

Figure 6.5: Cross-Effect Importance on Leakage Flow Rate for Straight Through Labyrinth Seal with k-ε Realizable Turbulence Model

6.3. Detail Flow Field Investigation for Static Labyrinth Seals

In a labyrinth seal, the leakage flow rate is mainly determined by two flow types and the first flow type is known as the "Vena Contracta" effect, which occurs at the first interaction of the tooth, as shown in Figure 6.6. This effect refers to the phenomenon that happens when a fluid flows through a small orifice, such as a labyrinth seal, where the cross-sectional area of the flow is reduced, causing a constriction in the flow. This results in an increase in fluid velocity and a corresponding decrease in pressure. The location of the point of maximum velocity and minimum pressure is known as the "Vena Contracta" point. The correct resolution of the boundary layer in this region is essential, as it significantly affects the flow rate.

Another important flow characteristic in labyrinth seals is the "Lid Driven Cavity" flow. As the flow passes through each pocket in the seal, the flow field is similar to the lid-driven cavity flow. The coexistence of these complex flow structures in labyrinth seals makes the solution more complicated. Therefore, the sensitivity of the solution to turbulence models becomes more important in this context. Figure 6.7 is an example of lid-driven cavity which is shown on the left and labyrinth seal flow field on the right.

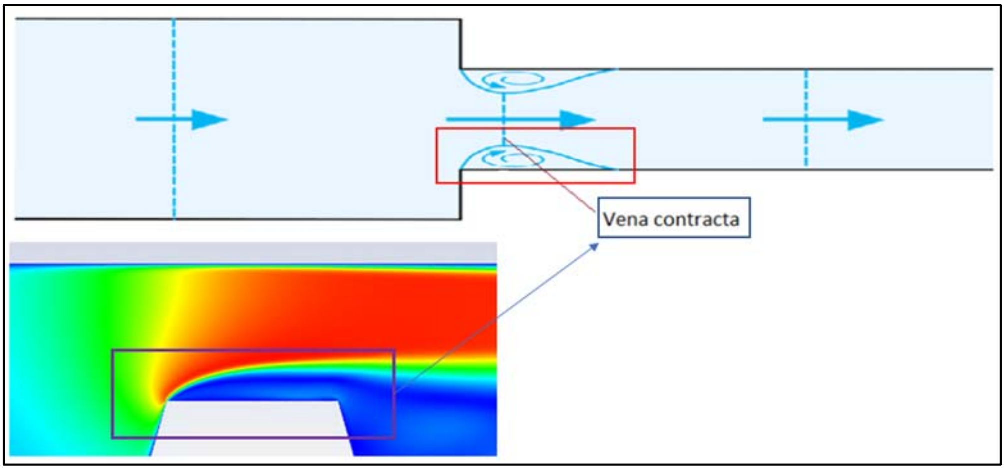

Figure 6.6: Labyrinth Seal Vena Contracta Flow

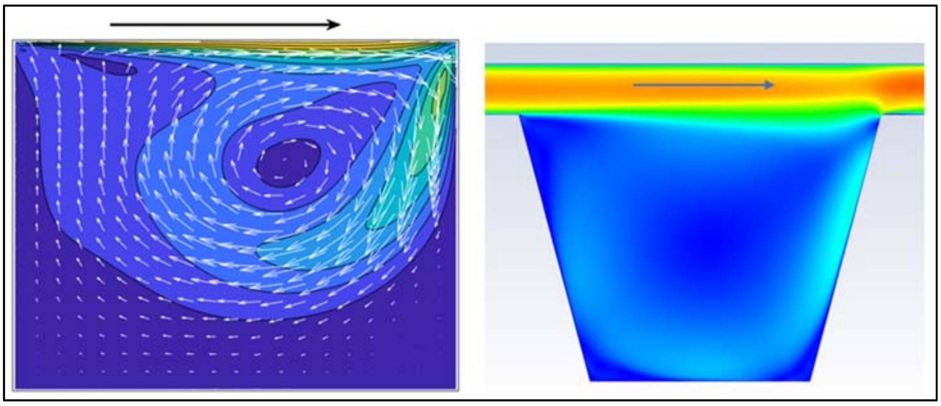

Figure 6.7: Labyrinth Seal Lid Driven Cavity Flow

It is critical to understand the behavior of the k-ε Realizable and k- ω SST turbulence models determined in both flow structures. In the next section, submodels for both flow physics will be established and the flow field will be discussed in detail.

6.4. Sub Model for Vena Contracta Effect

In order to understand vena contracta effect a sub model has been prepared and solved for k-ε Realizable and k- ω SST turbulence models. Figure 6.8 represents the sub model geometry and final mesh for the vena contracta effect.

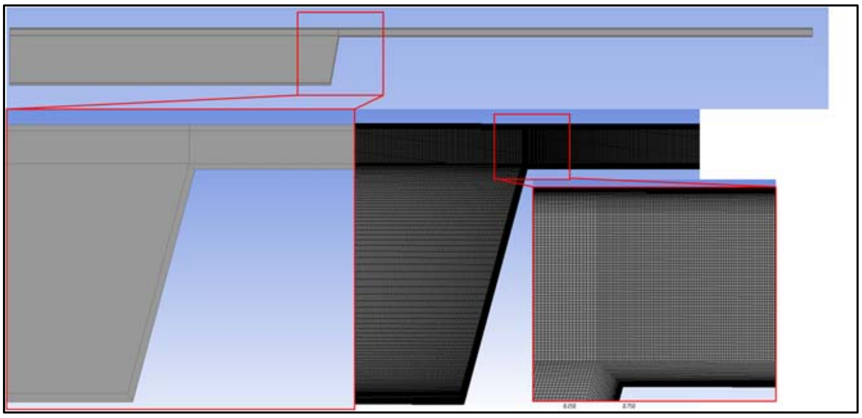

Figure 6.8: Sub Model Geometry and Mesh for Vena Contracta Effect

The axial velocity magnitude contour graph shown in Figure 6.9 and it clearly shows that the k-ω SST and k-ε turbulence models resolve the vena contract effect differently, and in the k-ω SST turbulence model, the boundary layer separates more clearly and the jet velocity of the fluid is higher.

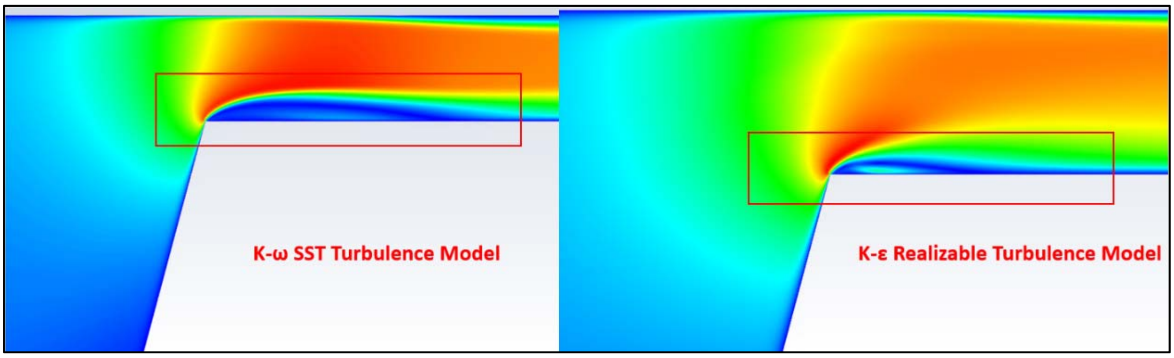

Figure 6.9: Axial Velocity Contour for Vena Contract Flow Field with k-ε and k-ω SST Turbulence Models

The difference between these two turbulence models depends on the approach used for the solution in the near-wall region. It has been observed that the axial velocity varies by 10-15% according to the two turbulence models. This stuation directly effects the amount of leakage flow rate. In addition, considering the flow in the labyrinth seal, the increase in the jet velocity directly affects the penetration into the cavity regions. This situation actually shows that the pressure loss in the cavity regions will be less in the solutions obtained with the k- ω SST turbulence model.

6.5. Sub Model for Lid-Driven Cavity

The sub-model geometry and mesh set up to understand the Lid-Driven flow are given in Figure 6.10. The objective of this model was to understand the cavity pressure loss for both turbulence models under similar conditions. Highest clearance value was selected for this sub model and the reason for this is the main focus was on the penetration of the fluid into the cavities rather than the jet velocity. Figure 6.10 shows both k-ε Realizable and k-ω SST turbulence models axial velocity contour. Two lines are compared according to the pressure loss, it has been seen that the difference between pressure losses were 1%. This sub model shows that if two velocities before the cavity are close to each other than there is no significant difference for these turbulence models.

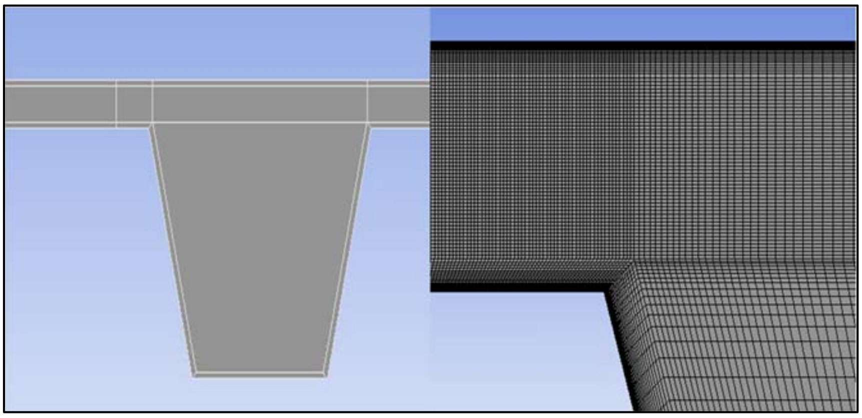

Figure 6.10: Sub Model Geometry and Mesh for Lid-Driven Cavity Effect

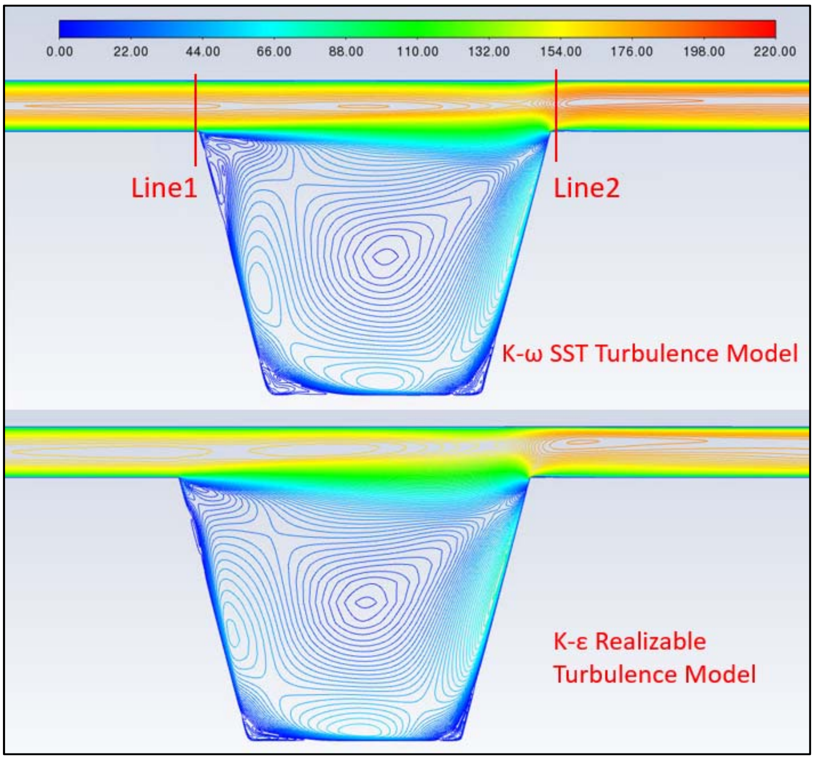

Figure 6.11: Axial Velocity Magnitude Contour for k-ε realizable and k-ω SST Turbulence Models

The first sub model is more critical because it also affects the jet flow and thus the possible penetration into the cavity in the later stages. However, this does not mean that the cavity flow is totaly not effective because its importance will increase as the size and number of cavities increases.

6.6. Improved Zimmerman-Wolff Equation

Zimmerman and Wolff's research demonstrated that the kinetic energy carry-over factor (k_2) is closely related to clearance, pitch and tooth number. To determine the C_d and the k_2, they suggested using Figure 2.2 and Figure 2.3 respectively. To improve the accuracy of the empirical correlation, three stages were undertaken.

Firstly, new coefficients k_{ctt}, k_{sc}, k_n introduced based on critical parameters that affects the leakage flow rate. Secondly, full factorial analysis matrices were created for each coefficient. Details of the matrix created for each coefficient are given in the following sections. The parameter levels were carefully selected considering the result of the TEI experiment. The k-ω SST turbulence model was used for tight clearances (≤ 0.30 mm), and the k-ε Realizable turbulence model was selected for higher clearances (>0.30 mm) which is based on TEI experiments results. Finally, with the new coefficients, aim is to improve the existing Zimmerman-Wolff correlation by using numerical analysis matrix with hybrid turbulence model selection approach.

6.6.1. Improved Zimmerman-Wolff Equation k_{ctt} Coefficient

Equation 6.1 represents the Zimmerman-Wolff equation multiplied by the k_{ctt} coefficient. To determine k_{ctt} coefficient equation 6.2 is used. This coefficient basically represents the CFD leakage flow result divided with Zimmerman-Wolff equation result. The aim here is to make a correction to approximate the Zimmerman-Wolff equation to the computed CFD result. To find k_{ctt} coefficient first fully factorial analysis matrix created and it is given with

$$\dot{m}_{kctt} = k_{ctt} * C_{dzim} \; * \; k_2 * A \; * Pt_0 * \sqrt{\frac{1-(\frac{p_n}{p_{t0}})^2}{RT_{t0} * [n + ln\, ln \left(\frac{p_{t0}}{p_n}\right)]}} \qquad 6.1$$

$$k_{ctt} = \frac{\dot{m}_{CFD}}{\dot{m}_{Zim}} \qquad 6.2$$

All analysis was 2D axisymmetric and rotation effect has not been considered. Rotational effect has been added in the later sections. For each geometry pressure ratio range was 1.1-2.0 with 0.1 step size and other geometrical parameters kept fixed for the k_{ctt} analysis matrix and given in

Table 6.3. With this approach, only the effect of clearance to tooth thickness ratio on the leakage flow rate was examined and the k_{ctt} coefficient was obtained. When k_{ctt} equals 1.0 it means that Zimmerman-Wolff correlation result and CFD computation are match each other. When $k_{ctt} <1$ it means Zimmerman-Wolff correlation calculate higher leakage flow rate and for $k_{ctt}> 1$ Zimmerman-Wolff correlation calculate less leakage flow rate. The variation of the k_{ctt} coefficient for different clearance to tooth thickness ratios for 0.15-0.30 mm clearance values is shown in Figure 6.12, Figure 6.13, Figure 6.14 and Figure 6.15. It should be noted that the pressure ratio changes in 0.1 steps from top to bottom.

Table 6.2: K_{ctt} Analysis Matrix Variable Parameter Details

Clearance [mm]	Clearance/Tooth Thickness	Turbulence Model
0.15	0.2-0.6	K-ω SST
0.20	0.3-0.8	
0.25	0.4-1.0	
0.30	0.4-1.2	
0.35	0.5-1.4	K-ε Realizable
0.40	0.6-1.6	
0.45	0.6-1.8	

Table 6.3: K_{ctt} Analysis Matrix Fixed Geometrical Parameters

Parameter	Value
Pitch [mm]	3
Tooth Height [mm]	2
Root Radius [mm]	40
Wedge Angle	20°
Tooth Number	4

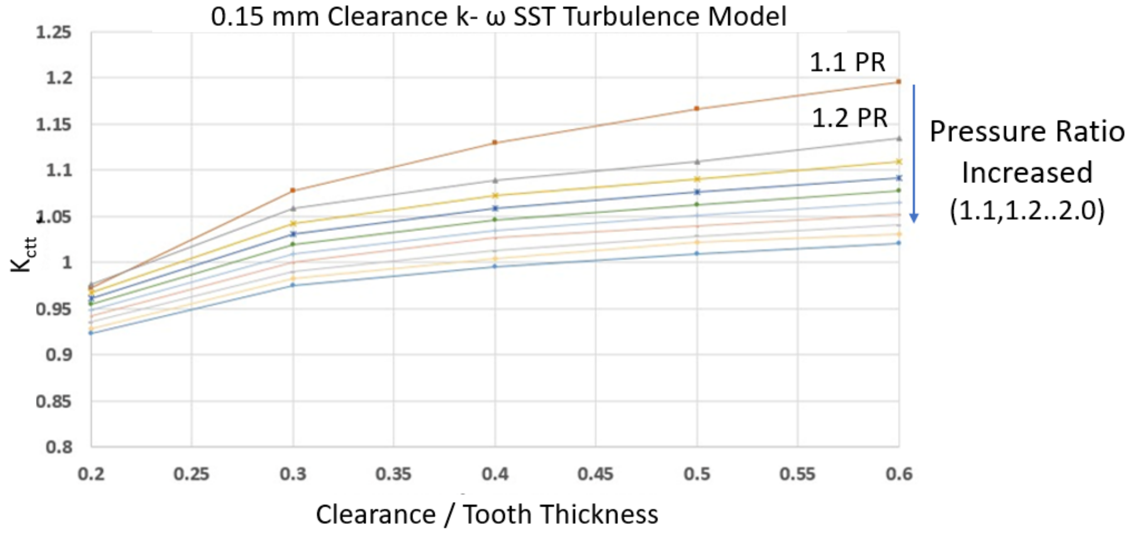

Figure 6.12: 0 K_{ctt} Coefficient Change for 0.15 mm Clearance with Different Clearance to Tooth Thickness and Pressure Ratio based on k- ω SST Turbulence Model

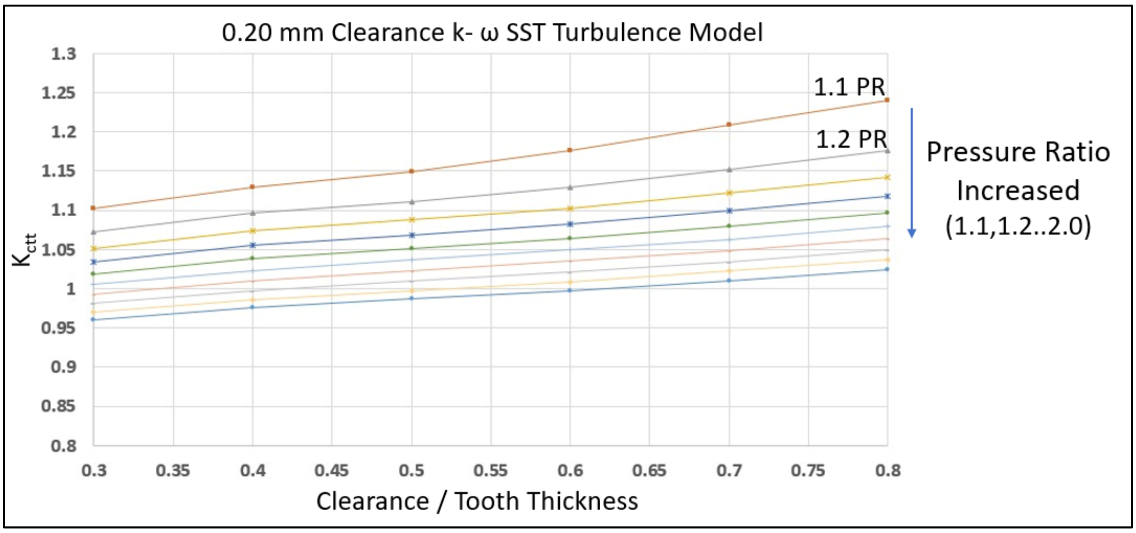

Figure 6.13: Kctt Coefficient Change for 0.20 mm Clearance with Different Clearance to Tooth Thickness and Pressure Ratio based on k- ω SST Turbulence Model

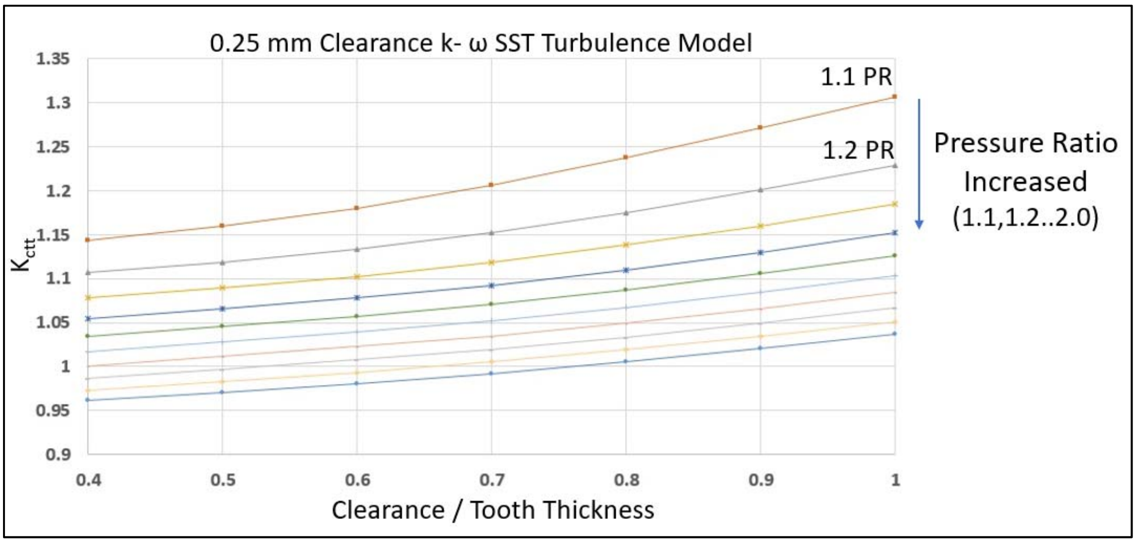

Figure 6.14: Kctt Coefficient Change for 0.25 mm Clearance with Different Clearance to Tooth Thickness and Pressure Ratio based on k- ω SST Turbulence Model

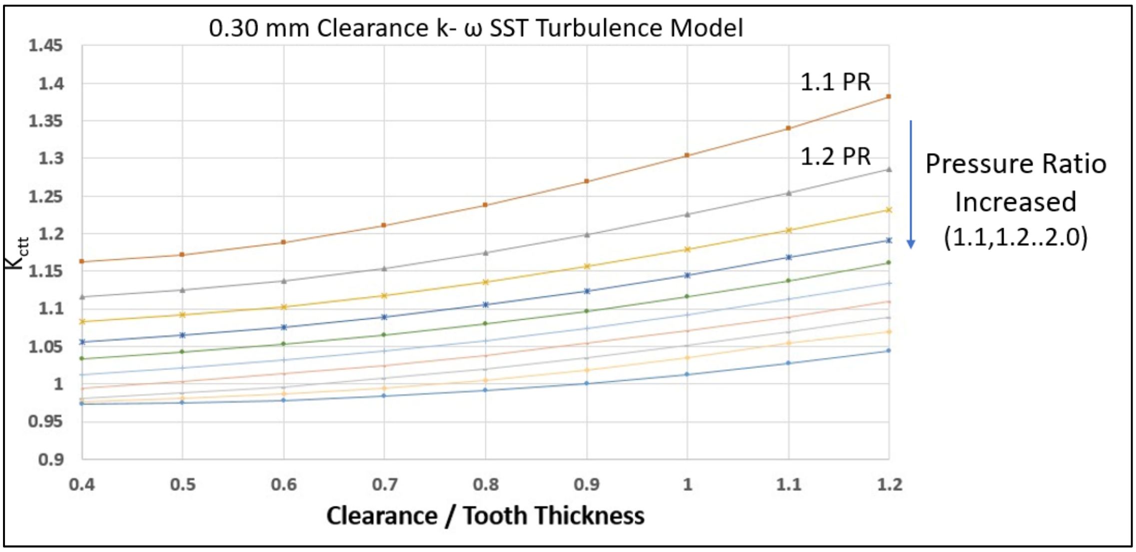

Figure 6.15: Kctt Coefficient Change for 0.30 mm Clearance with Different Clearance to Tooth Thickness and Pressure Ratio based on k- ω SST Turbulence Model

In general, when K_{ctt} considering Figure 6.12 to Figure 6.15 a certain variaty is observed for all clearances. For all ctt values, the K_{ctt} coefficient increases as the clearance increases. This indicates that as the clearance increases and the tooth tip thickness is constant, the flow rate obtained with CFD is greater than that obtained with the Zimmerman-Wolff equation. At the same time, it means that as the constant clearance maintain and tooth tip thickness decreases, the flow rate obtained with CFD is higher. Also, as the pressure ratio increases, the increase of the k_{ctt} coefficient has a lower slope which means especially at lower pressure ratios significant differences arises between CFD and Zimmerman-Wolff equation. For example, at low pressure ratios, k_{ctt} coefficient, a change of up to 40% is can be observed on the leakage flow rate. (0.30 mm clearance, 1.1 PR)

There are two methods that can be employed to utilize the k_{ctt} coefficient. The first method involves converting all the k_{ctt} figures into fitting polynomials that are suitable. The second approach is to seek a means of expressing all these polynomials as a single function with an acceptable level of error. Naturally, having a single function along with a related, practical non-dimensional number is more advantageous, although it presents a greater challenge. The clearance-to-tooth thickness ratio, pressure ratio, and clearances stand as the primary parameters for expressing the k_{ctt} coefficient. In the pursuit of establishing a single function for the kctt coefficient, the subsequent steps are pursued.

1. Each polynomial in Figures 6.6 to 6.9 is approximated as a basic linear function, represented by equation 6.3. The slope and constants are calculated for each clearance value.

$$y = mx + n \qquad 6.3$$

2. The variations in the function slopes (m) and constants (n) of all polynomials are examined for each clearance.
3. Distinct polynomials are formulated to illustrate the variations in the coefficients m and n.
4. Four unique polynomials are established for the coefficient m, and an additional four polynomials are created for the coefficient n. Each set of polynomials corresponds to a different clearance value. (For instance, $m1$ and $n1$ represent a clearance of 0.15 mm.)
5. Figure 6.16 illustrates the variation in the coefficient m for a clearance of 0.20 mm, while Figure 6.17 pertains to the coefficient n.

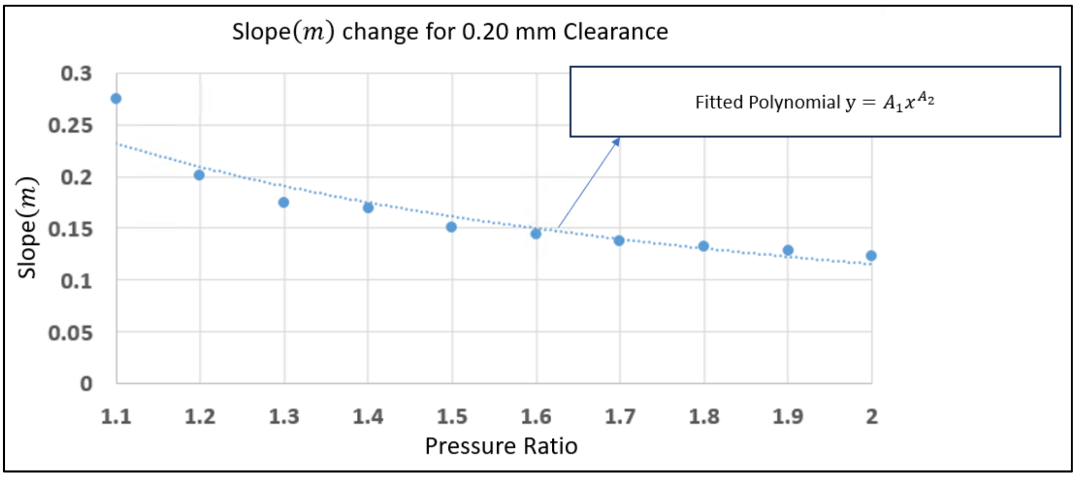

Figure 6.16: k- ω SST Turbulence Model Based K_{ctt} Coefficient Slope Change for 0.20 mm Clearance

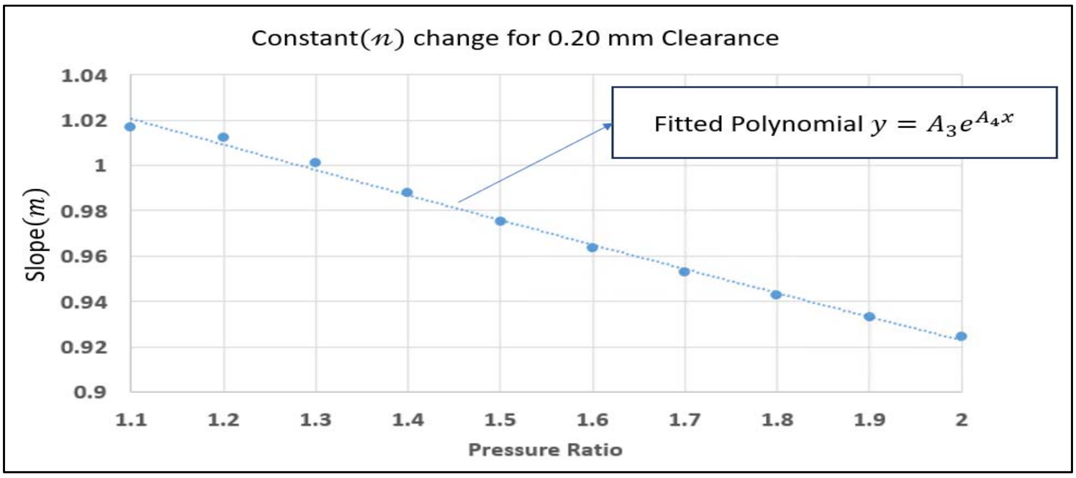

Figure 6.17: k- ω SST Turbulence Model Based K$_{ctt}$ Coefficient Constant Change for 0.20 mm Clearance

The same graphs were created for other clearances. And in step 1, instead of m, which is represented by equation 6.4, equation 6.5, which is fitted to the curves, is added. In order to represent n in equation 6.3, equation 6.5 which is fitted to the curves, is added. With the method followed, all curves were combined and a single equation for k$_{ctt}$ is represented for each clearance values.

$$m = A_1x^{A_2} \qquad 6.4$$

$$y = A_3e^{A_4x} \qquad 6.5$$

Up to know, there are four distinct equations for k$_{ctt}$ coefficient and each of them are belongs to a specific clearance value. Without immediately progressing to the creation of a one single equation that encompasses all clearances, it might be feasible to express all equations using the one of these equations but it should provide the error rate remains within an acceptable level (< 5%). Upon analyzing the outcomes, the equation 6.6, 0.20 mm clearance yielding a maximum error of approximately 1.7% and it can be applied to all clearances. Thus, the equation formulated for a 0.20 mm clearance value, was found as a best option. In addition, the histogram distribution of the error obtained when the equation 6.6 is used is given in Figure 6.18.

$$k_{ctt(0.15-0.30)} = (A_1 Pr^{A_2})\frac{c}{tt} + A_3 e^{A_4 PR} \qquad 6.6$$

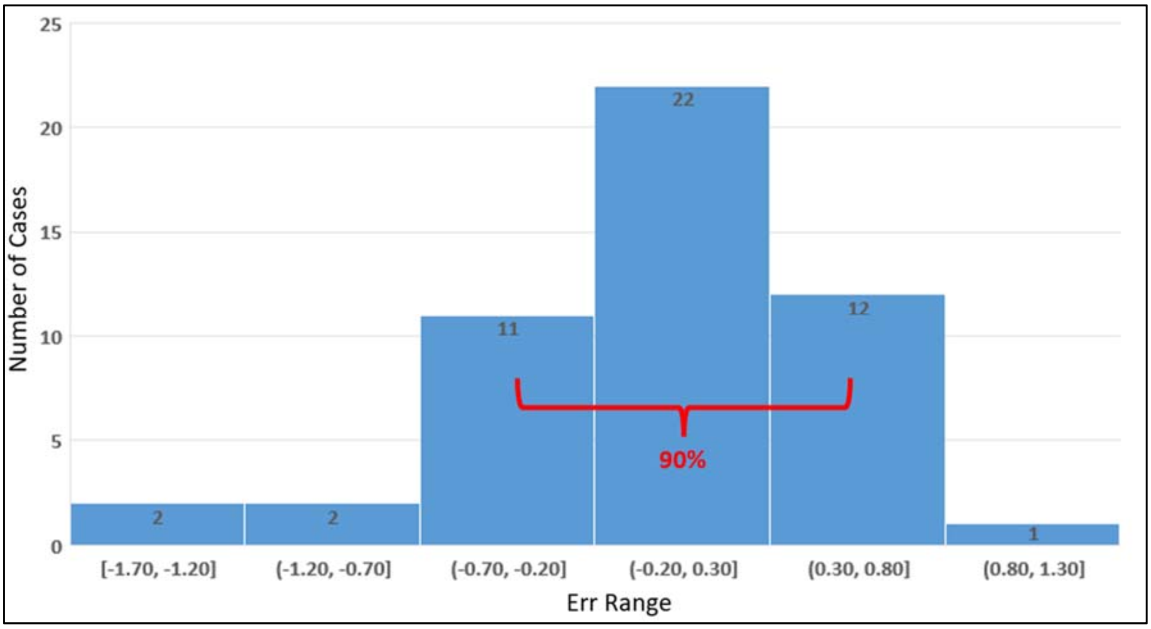

Figure 6.18: K$_{ctt}$ Coefficient for Equation 6.6 Error (Err) Distribution Histogram with Original Polynomials

When the histogram distribution shown in Figure 6.18 was examined, it was observed that the error rate was between -0.7% and +0.8%, as 90%. It should be noted here that while creating the single equation which is given in equation, the lowest pressure ratio was 1.1, the highest was 2.0 and the lowest ctt ratio was 0.3, highest was 1.2 and for both of them step size was 0.1. The user should not use the directly this equation for intermediate values. Instead, it should interpolate the two closest values. For example, considering that a calculation for a pressure ratio of 1.15 and ctt ratio 0.37. Equation 6.6 firstly solved for a pressure ratio of 1.1 with a ctt ratio of 0.3. Then it should be solved for 1.1 pressure ratio and 0.4 ctt ratio, then the same process is repeated for 1.2 pressure ratio, and the final desired value should be obtained by interpolating between these values.

The same procedure was repeated for 0.35-0.45 mm clearance. Single equation obtained with using 0.35 mm clearance was selected due to lower error rates. Figure 6.19 represents slope (m) change where as Figure 6.20 shows constant (n) change for

0.35 mm clearance. The final equation representing the k$_{ctt}$ coefficient for the 0.35-0.45 mm clearances is denoted by equation 6.7.

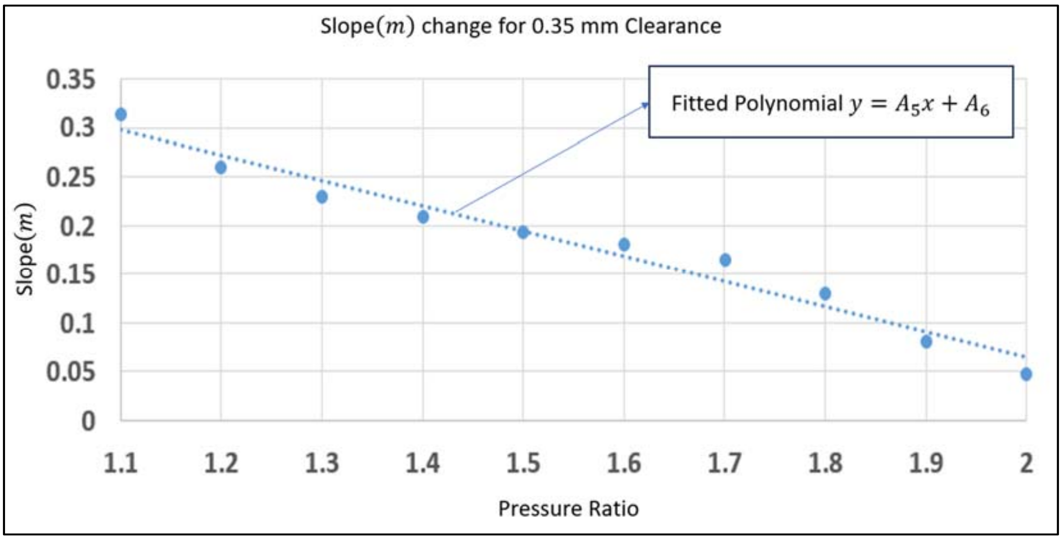

Figure 6.19: k-ε Realizable Turbulence Model Based K$_{ctt}$ Coefficient Slope Change for 0.35 mm Clearance

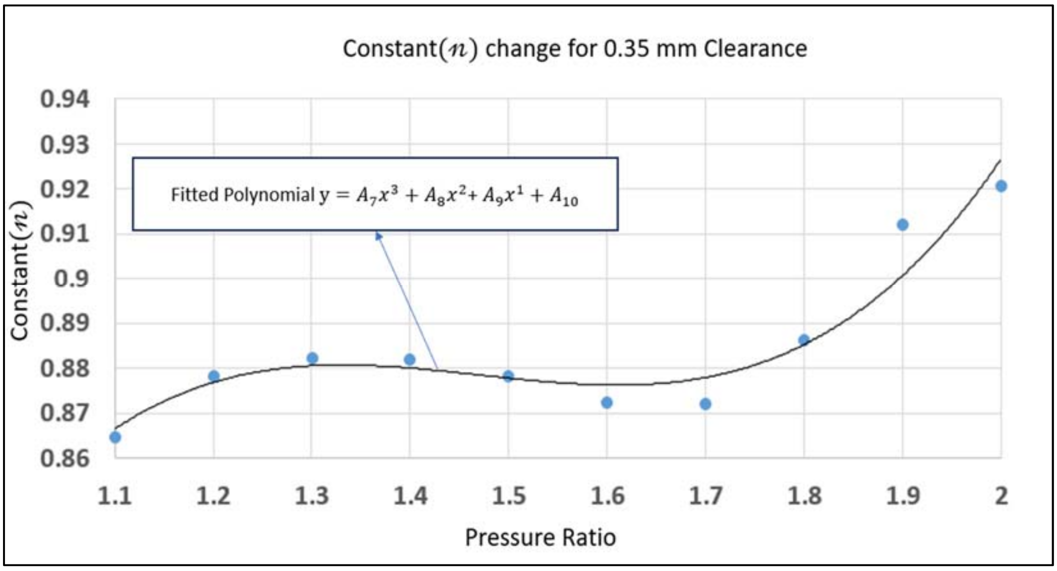

Figure 6.20: k-ε Realizable Turbulence Model Based K$_{ctt}$ Coefficient Constant Change for 0.20 mm Clearance

$$k_{ctt(0.35-0.45)} = (A_5PR + A_5)\frac{c}{tt} + A_7PR^3 + A_8PR^2 + A_9PR^1 + A_{10} \qquad 6.7$$

The histogram distribution of the error obtained when the equation 6.8 is used is given in Figure 6.21. Histogram distribution shows that 87.40% of comparison stays between -0.53% to +2.15% which is quite acceptable.

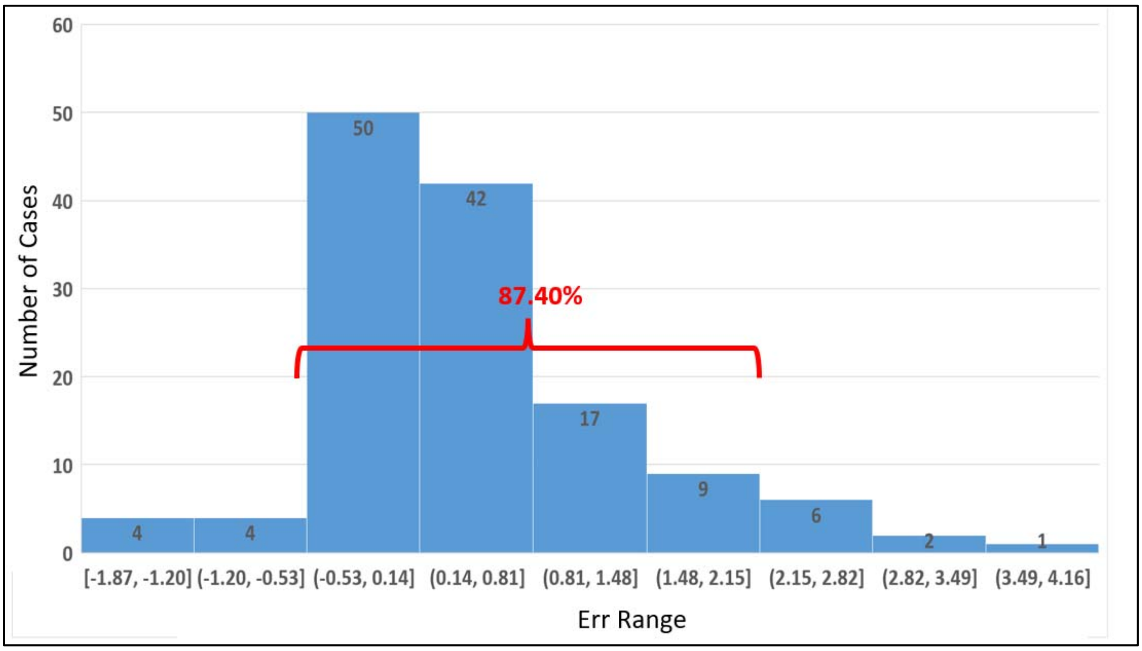

Figure 6.21: K_{ctt} Coefficient for Equation 6.7 Error (Err) Distribution Histogram with Original Polynomials

6.6.2. Improved Zimmerman-Wolff Equation k_{sc} Coefficient

In the previous section, the k_{ctt} coefficient was developed for using the clearance to tooth thickness ratio based on CFD analysis matrix, and using this coefficient, the results obtained from the one-dimensional Zimmerman-Wolff equation were approximated to the CFD results. However, the pitch was taken as constant in the k_{ctt} analysis matrix. In order to examine the influence of pitch on the leakage for labyrinth seals another non-dimensional number was used which is pitch to clearance ratio. When clearance is fixed, increasing pitch reduces the carry-over coefficient, which also reduces to leakage flow rate. The reason for this behaviour is that as the pitch increases, the fluid can penetrate much more into the cavities. It is important to determine an appropriate range for pitch to clearance ratio that can be used in a wide range of engines. A new CFD analysis matrix was created and solved with two different turbulence models as done in the previous section. Equation 6.8 and equation 6.9 shows how k_{sc} coefficient is incorporated into the Zimmerman-Wolff equation.

$$\dot{m}_{kctt,ksc} = k_{ctt} * C_{dzim} * k_{sc} \; * \; k_2 * A \; * Pt_0 * \sqrt{\frac{1-(\frac{p_{se}}{p_{t0}})^2}{RT_{t0} * [n + ln(\frac{p_{t0}}{p_{se}})}} \quad 6.8$$

$$k_{sc} = \frac{\dot{m}_{(kctt)}}{\dot{m}_{CFD}} \quad 6.9$$

When the pitch size is changed according to the first analysis matrix, which is fixed with 3 mm, the leakage flow rate changes according to the CFD results. This relationship is shown for 0.15 to 0.30 mm clearance values in Figure 6.22. These curves represent the $\dot{m}_{\text{deviation}}$, which is described in equation 6.10. In the new analysis matrix, the pitch to clearance ratio was taken into account and the range of 10 to 30 was selected.

$$\dot{m}_{\text{deviation}} = \left(\frac{\dot{m}_{(kctt)} - \dot{m}_{(CFD)}}{\dot{m}_{(kctt)}}\right) \quad 6.10$$

Equation 6.10 was calculated at the end of each analysis. When the results obtained for different clearance values and different pressure ratios are examined, it is seen that the results with the same clearance value are close to each other regardless of the pressure ratio. Since $\dot{m}_{\text{deviation}}$ values are close to each other it makes easy to fit it in a different polynomial equations based on different clearance values. It was observed that $\dot{m}_{\text{deviation}}$ values deviated seriously from the average especially after 1.5 pressure ratio. At this point, it was decided to update the equation pressure ratio range between 1.1-1.5. This approach comes with a mean deviation approximation now has a minimum error rate of -1.3% and a maximum error rate of +2.5% up to a pressure ratio value of 1.5. Also, it limits the correlation range for pressure ratio around 1.1 to 1.5. In Figure 6.22 $\dot{m}_{\text{deviation}}$ for 0.15 to 0.30 mm clearance values are shown.

It also lacks of 10 and 15 pitch to clearance ratio values for 0.15 mm and 10 pitch to clearance ratio for 0.20 mm clearance values. The reason for this is that a seal of that size is unlikely to be used, so it is not included in the analysis matrix. In Figure 6.22 it can be seen that four different fitted polynomial equations mainly has two different coefficients for each clearance value. Since these coefficients are change indices has been used for to define coefficients (B, C). The variation of slope (B) and constant (C) coefficients are shown in Figure 6.23 and Figure 6.24.

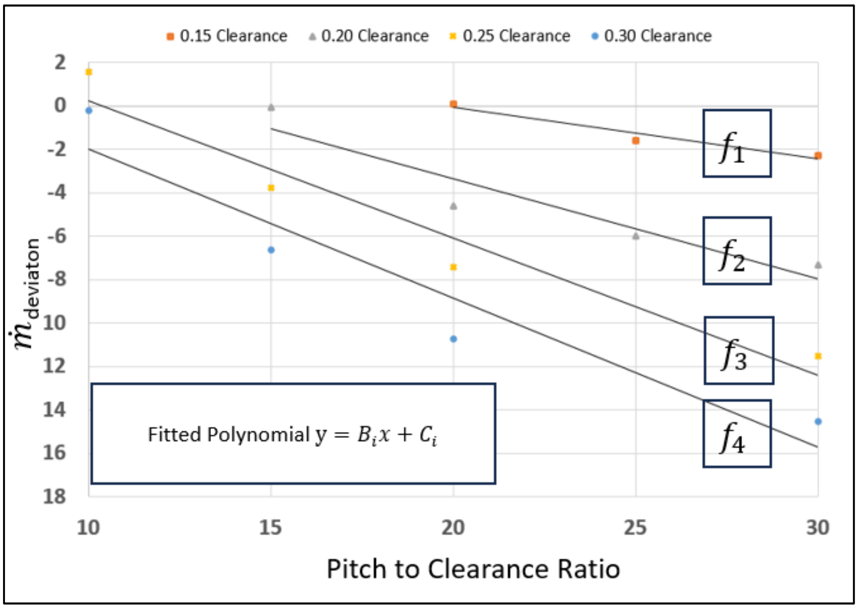

Figure 6.22: $\dot{m}_{\text{deviation}}$ for Pitch to Clearance Ratio with 0.15 mm to 0.30 mm Clearance Values

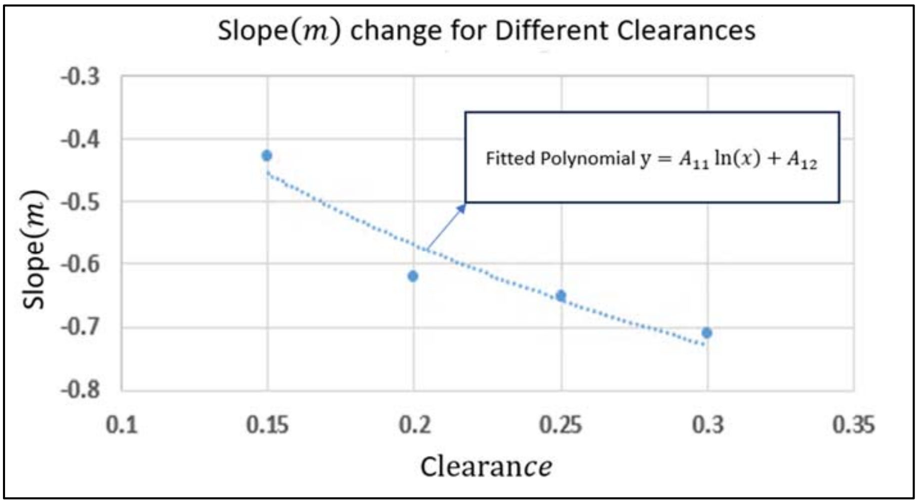

Figure 6.23: k- ω SST Turbulence Model Based K_{ctt} Coefficient Slope Change for Different 0.15-0.30 mm Clearances

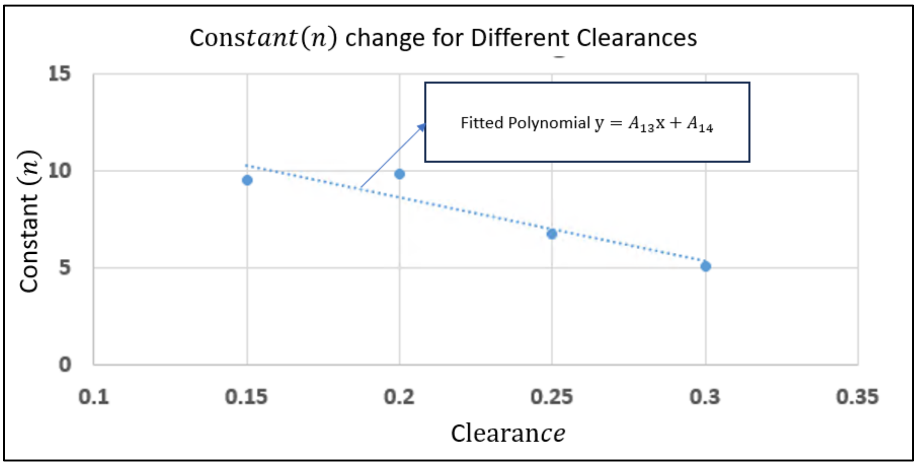

Figure 6.24: k- ω SST Turbulence Model Based K_{ctt} Coefficient Constant Change for Different 0.15-0.30 mm Clearances

Equation 6.11 can be used to describe the k_{sc} values for clearance values in the range of 0.15-0.30 mm. It should be noted again here intermediate values such as 0.17 clearance or 12 pitch to clearance ratios should not directly used in the equation 6.11. On the contrary, necessary interpolation operations should be done as it shown in previous section.

$$k_{sc\ (0.15-0.30)} = (A_{11} * \ln(c) + A_{12}) * \frac{s}{c} + (A_{13} * c + A_{14}) \qquad 6.11$$

In Figure 6.19 the result of mdeviation and pitch to clearance ratio for 0.35 mm to 0.45 mm clearances are shown. Since it cannot be expressed linearly for the appropriate R^2 value, it is expressed with a quadratic polynomial. Fitted polynomial this time has three different coefficient and in order to apply same procedure as shown in before, all of these coefficient's variation needs to be fitted another linear function.

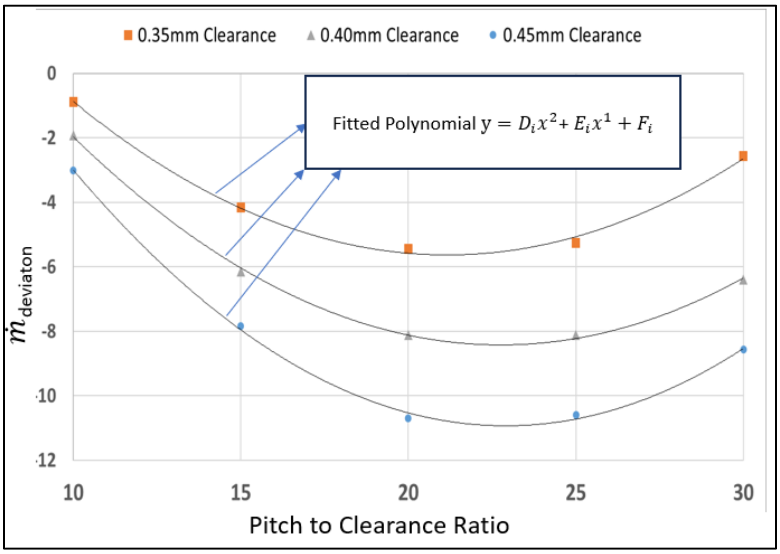

Figure 6.25: $\dot{m}_{\text{deviation}}$ for Pitch to Clearance Ratio with 0.35 mm to 0.45 mm Clearance Values

Fortunately, these coefficients (D, E, F) have linear relationship and variation of coefficients shown in Figure 6.20, Figure 6.21 and Figure 6.22 respectively.

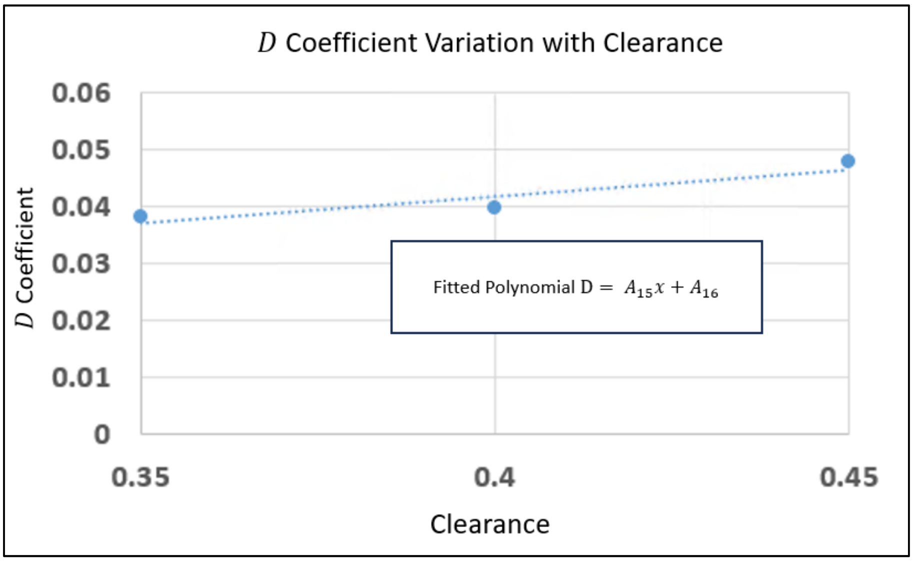

Figure 6.26: D Coefficient Change with Clearance

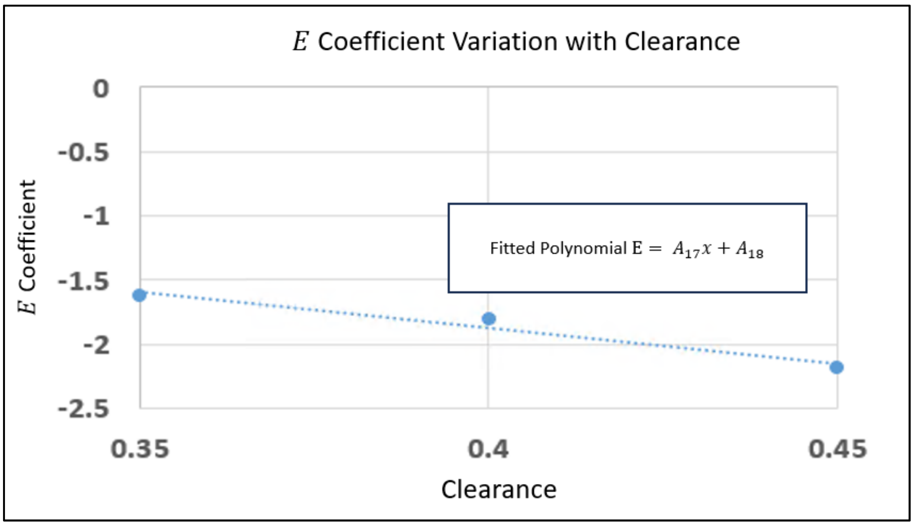

Figure 6.27: E Coefficient Change with Clearance

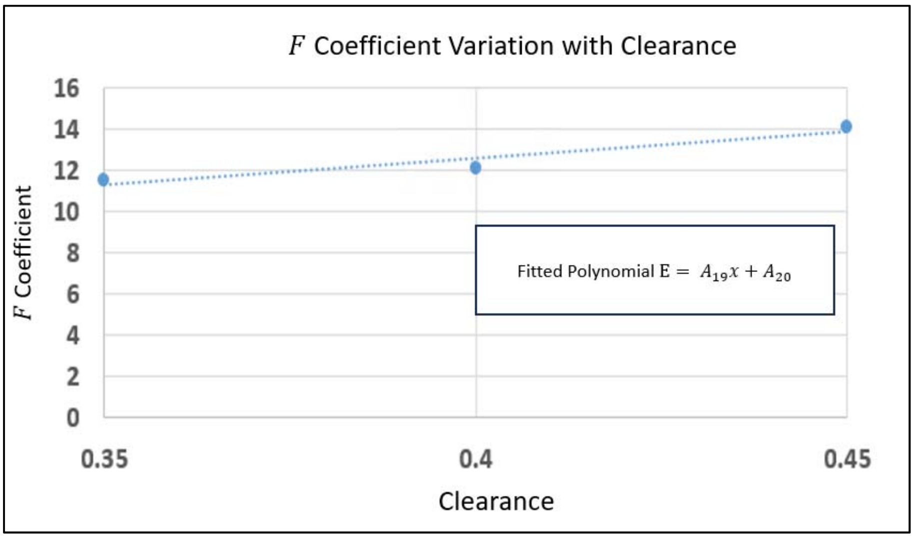

Figure 6.28: F Coefficient Change with Clearance

For the k_{sc} coefficient covering the range of clearance values of 0.35-0.45 mm, all the obtained functions are gathered in a single function and the equation is represented by equation 6.12.

$$k_{sc\,(0.35-0.45)} = (A_{15} * c + A_{16}) * \frac{s^2}{c} + (A_{17} * c + A_{18}) * \frac{s}{c} + (A_{19} * c + A_{20}) \qquad 6.12$$

6.6.3. Improved Zimmerman-Wolff Equation k_n Coefficient

While generating the analysis matrices for the k_{ctt} and k_{sc} coefficients, the number of teeth was kept constant at 4. Initially, analyses were conducted for both the 3-tooth and 5-tooth configurations, involving variations in the pressure ratio within the range of 1.1 to 1.5. The K_n coefficient for the 40 distinct analyses carried out for the 3-tooth configuration is presented in Figure 6.29, while the corresponding results for the 5-tooth configuration are displayed in Figure 6.30. Remarkably, despite the varying pressure ratios, the observed changes in the k_n coefficient remained below 1%. For this reason, analyzes were performed for 3 to 9 teeth by choosing a constant pressure ratio of 1.3. The relationship obtained for the Kn coefficient between 3 and 9 teeth is shown in Figure 6.31. Equation 6.12 and 6.13 used to find k_n coefficient for each analysis.

$$\dot{m}_{kctt,kcn} = k_{ctt} * C_{dzim} * k_n \; * \; k_2 * A \; * Pt_0 * \sqrt{\frac{1-(\frac{p_{se}}{p_{t0}})^2}{RT_{t0} * [n + ln(\frac{p_{t0}}{p_{se}})}} \qquad 6.13$$

$$k_n = \frac{\dot{m}_{(kctt)}}{\dot{m}_{CFD}} \qquad 6.14$$

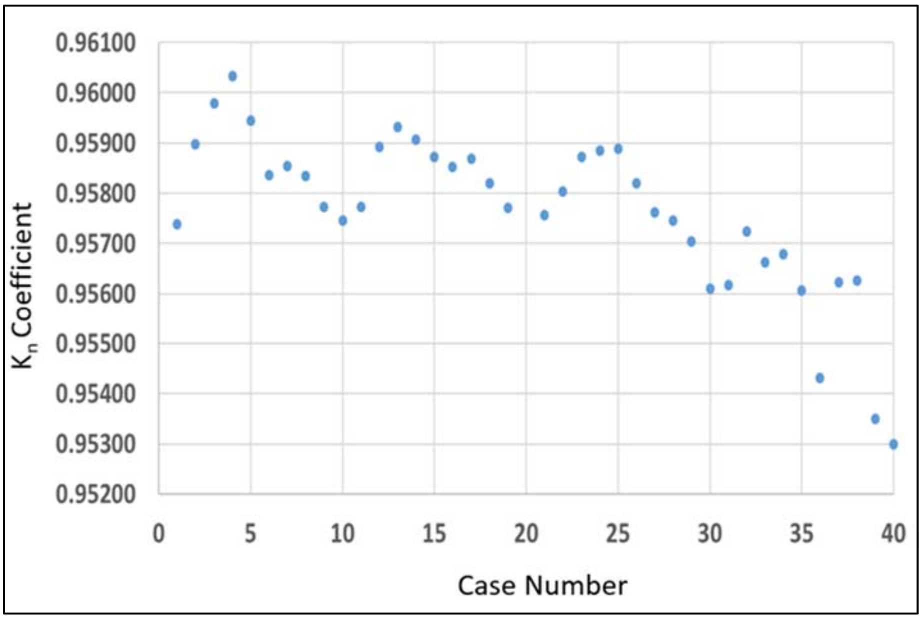

Figure 6.29: 3 Teeth Configuration K$_n$ Coefficient Change with 1.1 to 1.5 Pressure Ratios

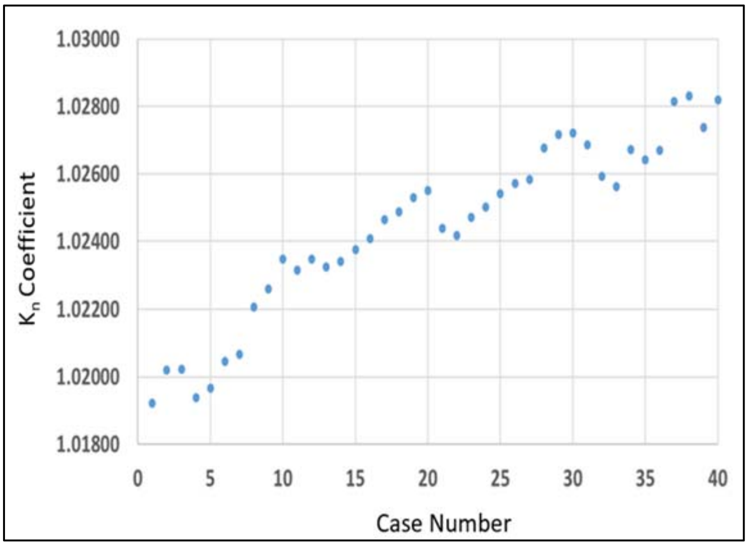

Figure 6.30: 5 Teeth Configuration K$_n$ Coefficient Change with 1.1 to 1.5 Pressure Ratios

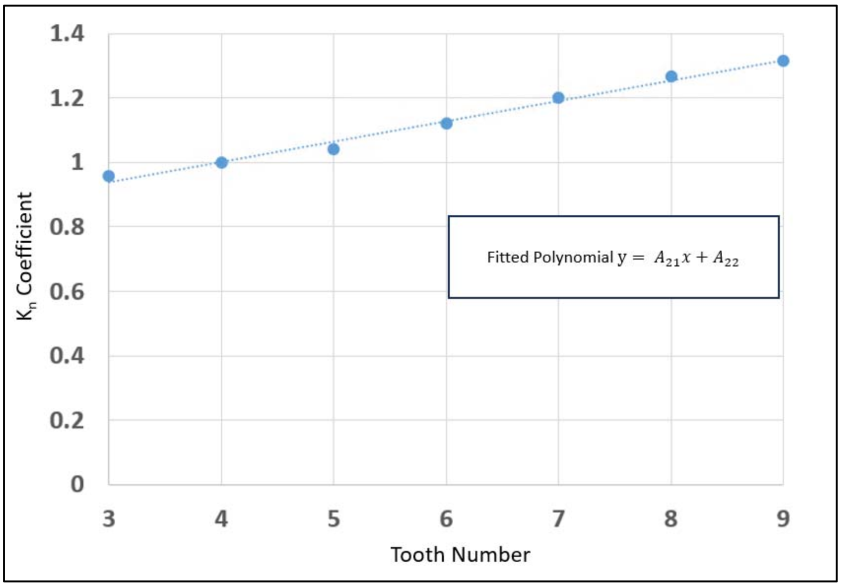

Figure 6.31: K_n Coefficient Change for 3-9 Teeth Number

Equation 6.15 represents the K_n coefficient and it can be used for 0.15 mm to 0.45 mm clearance values.

$$k_{n\,(0.15-0.45)} = (A_{21} * n + A_{22}) \tag{6.15}$$

In summary, certain assumptions are made and outlined below in order to determine the k_{ctt}, k_{sc} and k_n coefficients.

- New correlation applicable for 0.15 mm to 0.45 mm clearance values with 1.1 to 1.5 pressure ratio.
- Due to the distinct kctt and ksc coefficients for clearances within the range of 0.15 to 0.30 mm and 0.35 to 0.45 mm, both correlations can be employed for clearance values ranging from 0.30 to 0.35 mm. However, to obtain a more accurate result, it is recommended to take the average of the values obtained from the two correlations.

6.7. Improved Equation Comparison with Experiment

In this section, the comparison has been made for the experimental results with the original Zimmerman-Wolff equation, improved Zimmerman-Wolff equation, k-ε Realizable turbulence model-based solution and k-ω SST turbulence model-based solution.

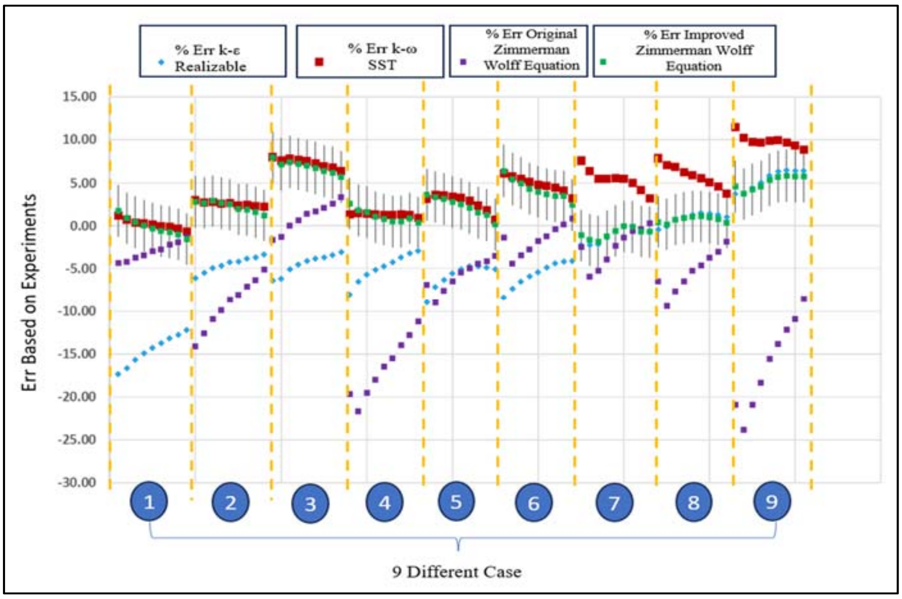

Figure 6.16: Experimental Result Comparison with Original Zimmerman-Wolff Equation, Improved Zimmerman-Wolff Equation, k-ε Realizable and k-ω SST turbulence model-based solutions

It can be seen that the original Zimmerman-Wolff equation has an error rate that can reach up to 25%. The red color represents the k-ω SST turbulence model, and it is close to the experimental results under certain clearance values (0.15-0.30 mm). After that, the k-ε realizable model is somewhat more in line with the experimental results. At this point, when the improved corrected Zimmerman-Wolff equation is examined, and the 5% deviation value added to represent the deviation comes from both CFD and single equation approach also considered. In Figure 6.32, the average error rates of the improved Zimmerman-Wolff equation with the original Zimmerman-Wolff, according to the experimental results are shown.

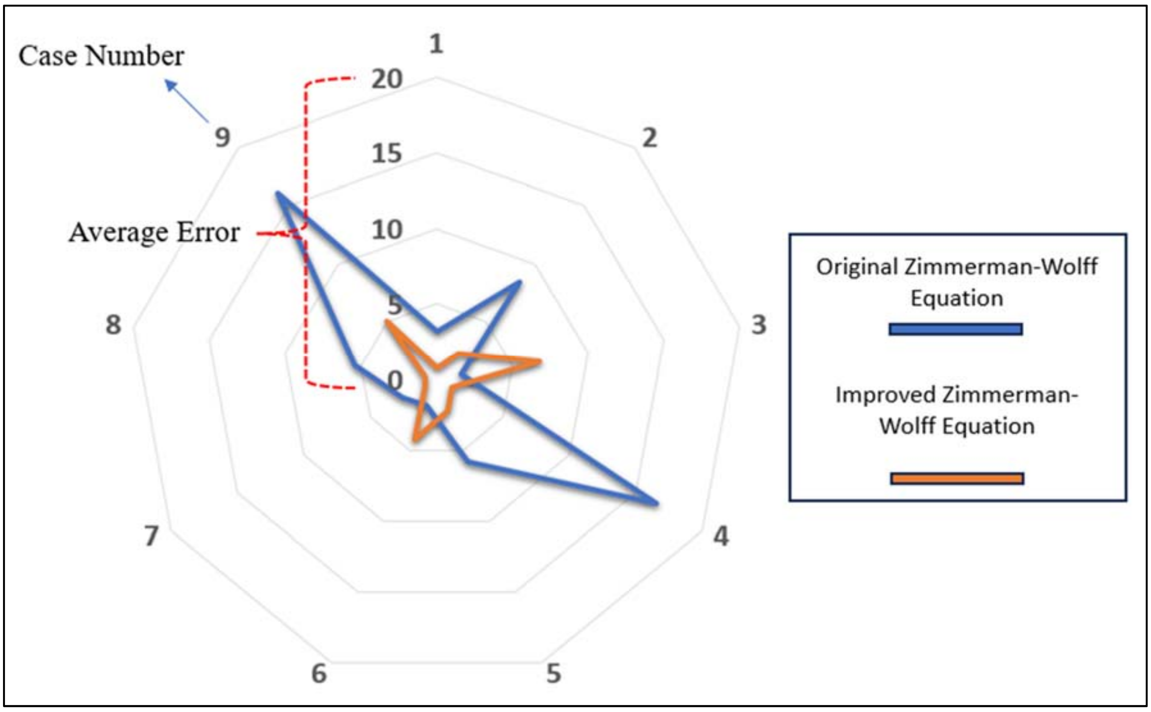

Figure 6.32: Experimental Result Average Error of Original Zimmerman-Wolff Equation and Improved Zimmerman-Wolff Equation

6.8. Detail Flow Field Investigation for Dynamic Labyrinth Seals

The full factorial analysis matrix shown in Table 6.2 was prepared to examine the leakage flow rate, windage heating and the swirl ratio effects in great detail. A total of 972 analyzes were carried out.

Table 6.4: Dynamic Labyrinth Seal Parameters for Full Factorial Analysis Matrix

Parameter	Values
Clearance [mm]	0.15-0.30-0.45
Tooth Thickness [mm]	0.4-0.6-0.8
Pitch [mm]	4-6-8
Tooth Number	3-4-5
RPM [rev/min]	20.000 – 30.000 – 40.000
Tooth Height [mm]	2.794
Tooth Wedge Angle [°]	20°
Root Radius [mm]	40

In labyrinth seals, with the rotor surface gaining a certain speed, the total temperature of the fluid will start to increase due to the viscous work, while the tangential velocity component will also increase. In this section firstly detail flow field has been investigated also the significance of labyrinth seal geometrical parameters concerning the swirl ratio and windage heating, as well as establishing non-dimensional parameter relationships for these variables examined. The order of importance of the parameters for the Windage Heating Number was determined as follows: Clearance, Tooth Number, Pressure Ratio, Pitch, and Tooth Thickness, as depicted in Figure 6.33. The same ordering applies to the swirl ratio, but the standardized effects of the parameters are different as shown in Figure 6.34.

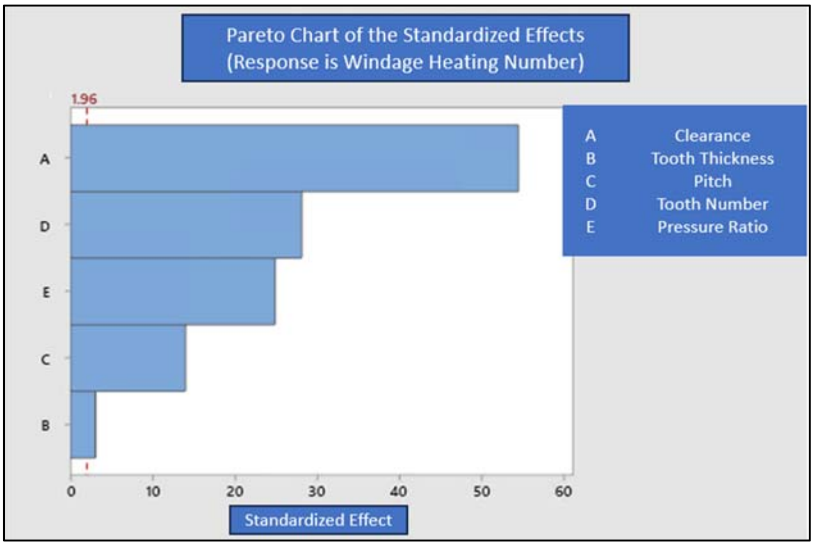

Figure 6.33: Order of Importance of Geometrical Parameters on Windage Heating Number

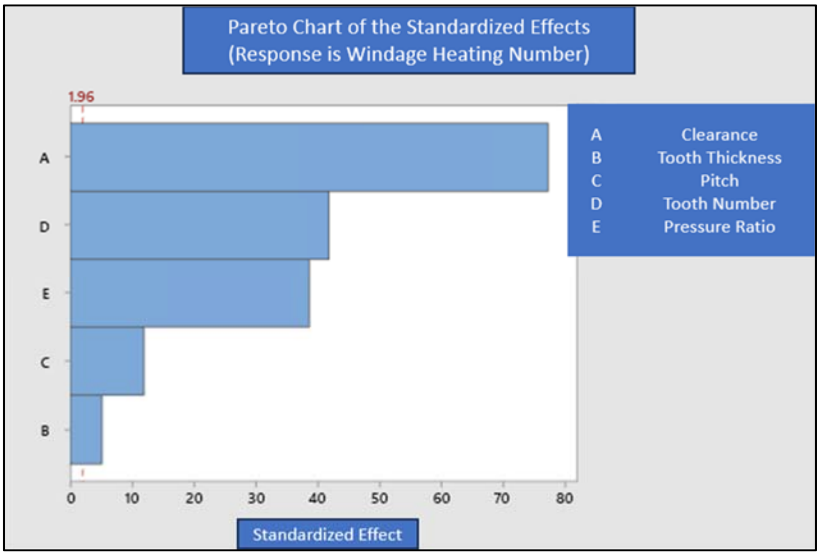

Figure 6.34: Order of Importance of Geometrical Parameters on Swirl Ratio

It is obvious that the swirl ratio and windage heating number will increase as the rotor's contact with the fluid increases. The relationship between flow function and swirl ratio obtained from the analyzes is given in Figure 6.35 for different pressure ratios. It can be seen that as the flow function increases swirl ratio suddenly decreases and the result of swirl ratio could be the same for different pressure ratios, if appropriate geometrical parameters selected. Windage heating is similar to the swirl ratio, but it decreases more rapidly as the flow function increases as it shown with Figure 6.36. It should not be forgotten that the RPM can go up to 40k in the analyzes presented here, it is obvious that the analyzes with the maximum RPM and the minimum pressure ratio will approach the maximum values for windage heating. It has been observed that similar outputs can be obtained up to the case where the windage heating number is 2, if the appropriate geometric parameters are selected for the pressure ratio range of 1.1-1.7.

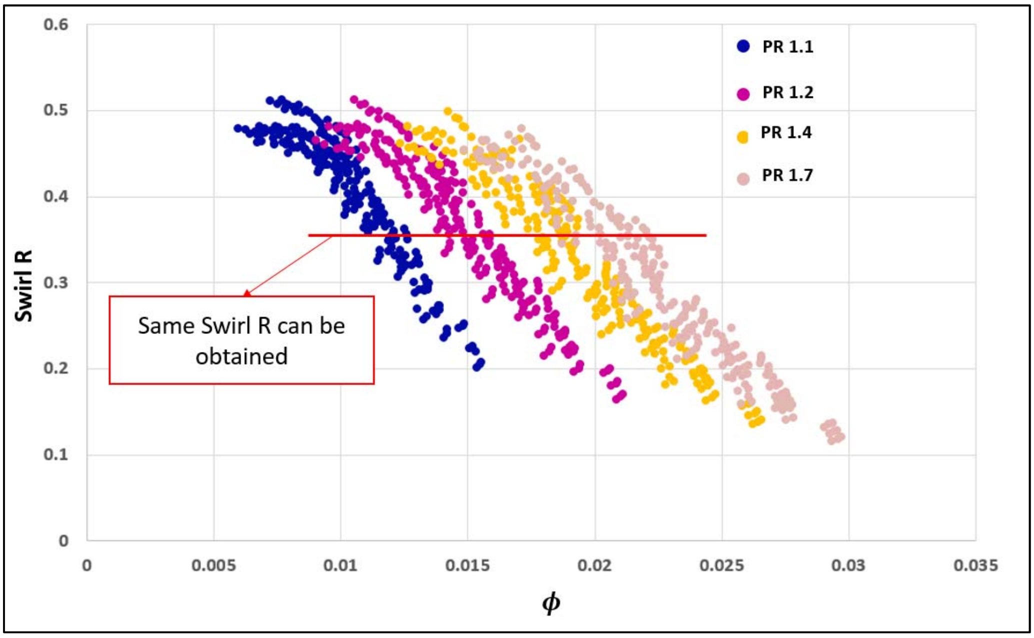

Figure 6.35: Swirl Ratio and Flow Function Relationship for Different Pressure Ratios

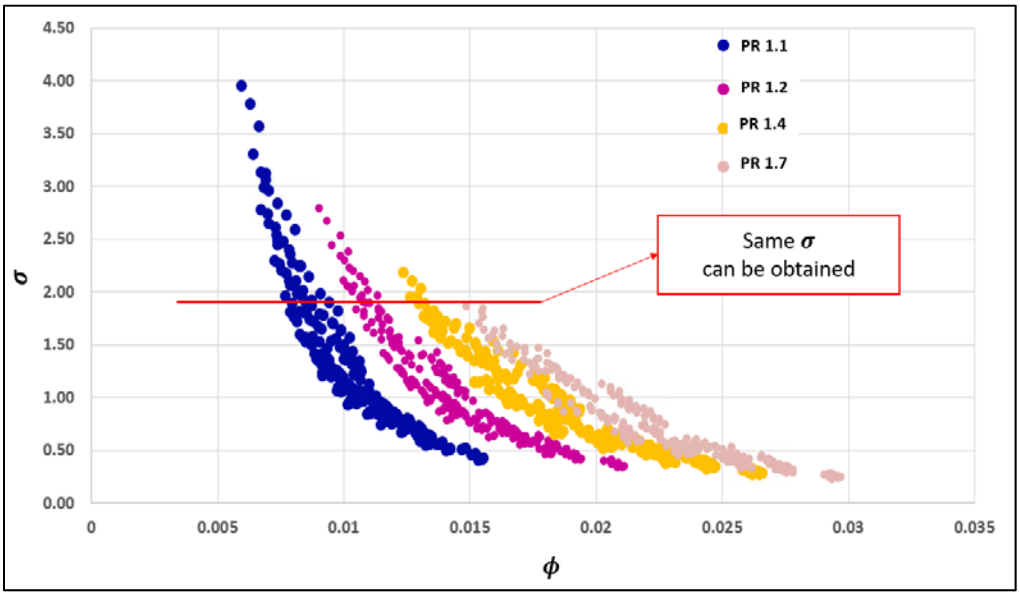

Figure 6.36: Windahe Heating Number and Flow Function Relationship for Different Pressure Ratios

Considering that the inlet temperature is 300K in the analysis matrix created, it will be useful to observe the order of temperature increases in all analyzes. In Figure 6.37, the temperature differences obtained for 972 analyzes are shown, it has been observed that the temperature difference up to 100K has been reached. As expected, this situation was obtained with the maximum rotor surface area (maximum pitch, tooth number, tooth thickness) and RPM with the lowest pressure ratio (1.1) and clearance (0.15). Also, as the RPM increased It was observed that as the rotor RPM value increased, the leakage flow decreased slightly compared to the static situation, and this increased up to 15% in the labyrinth seals with the largest rotor surface area and highest RPM (40k) value.

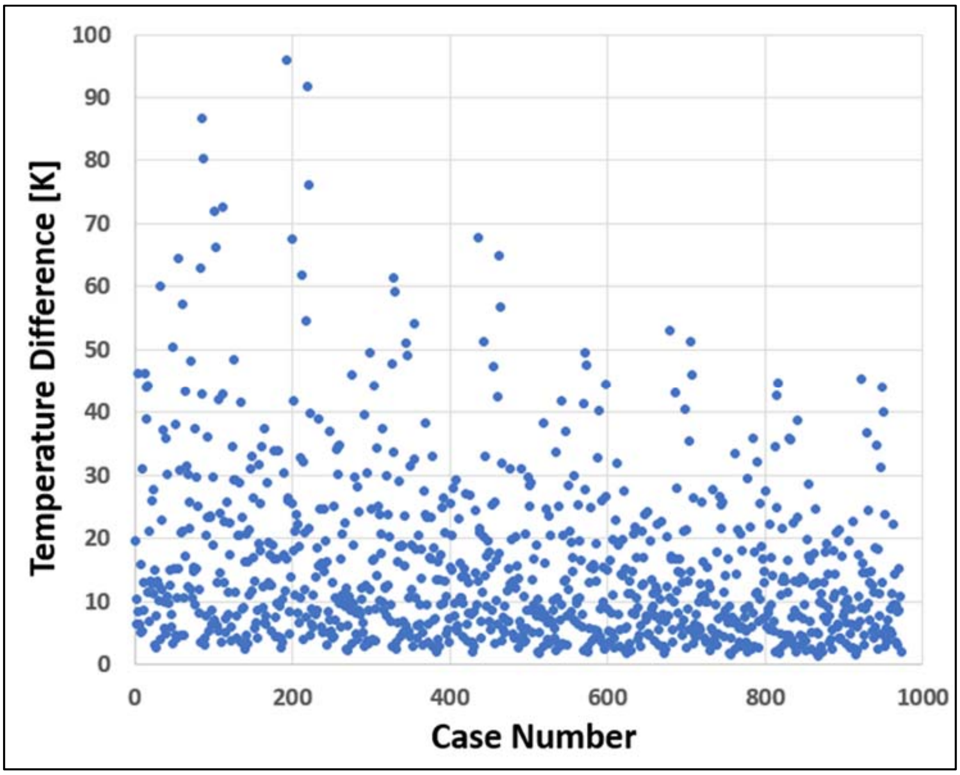

Figure 6.37: Temperature Difference for All Analysis

7. LABYRINTH SEAL WITH HONEYCOMB LAND

The previous sections of the thesis have focused on straight through labyrinth seals without honeycomb lands. However, honeycomb structures are commonly used in gas turbine engines, particularly in aviation. Therefore, this section of the thesis aims to examine straight through labyrinth seals with honeycomb lands. In order to investigate the effect of honeycomb lands on the leakage flow rate, an analyses matrix was prepared and the parameters and values are shown in Table 7.1.

Table 7.1: Analysis Matrix Parameter and Values for Honeycomb Lands Effect

Parameter	Value(s)
Clearance [mm]	0.3 – 0.4 – 0.5
Tooth Thickness [mm]	0.25-0.45-0.65
Pitch [mm]	3-4-5
Pressure Ratio	1.1-1.3-1.5
Honeycomb Depth [mm]	2
Honeycomb Cell Size [inch]	1/32 – 1/16

Since 3D analyzes take a lot of time (3 days for each analysis), design of experiments approaches should be used, and in this direction, the analysis matrix was created with the Taguchi L27 method. All analysis points are given in the appendix. Totally 54 analysis (27+27) has been done for each cell size (1/32 – 1/16). These analyzes were carried out with no rotation and focused on the effect of the honeycomb structure on leakage flow. Firstly, reduction rate investigated as it described with equation 5-2. The reduction rate for 27 analyzes with 1/32 H_{cs} value is given in Figure 7.1. With the honeycomb structure, a minimum 15% and a maximum 22% leakage flow rate reduction was observed.

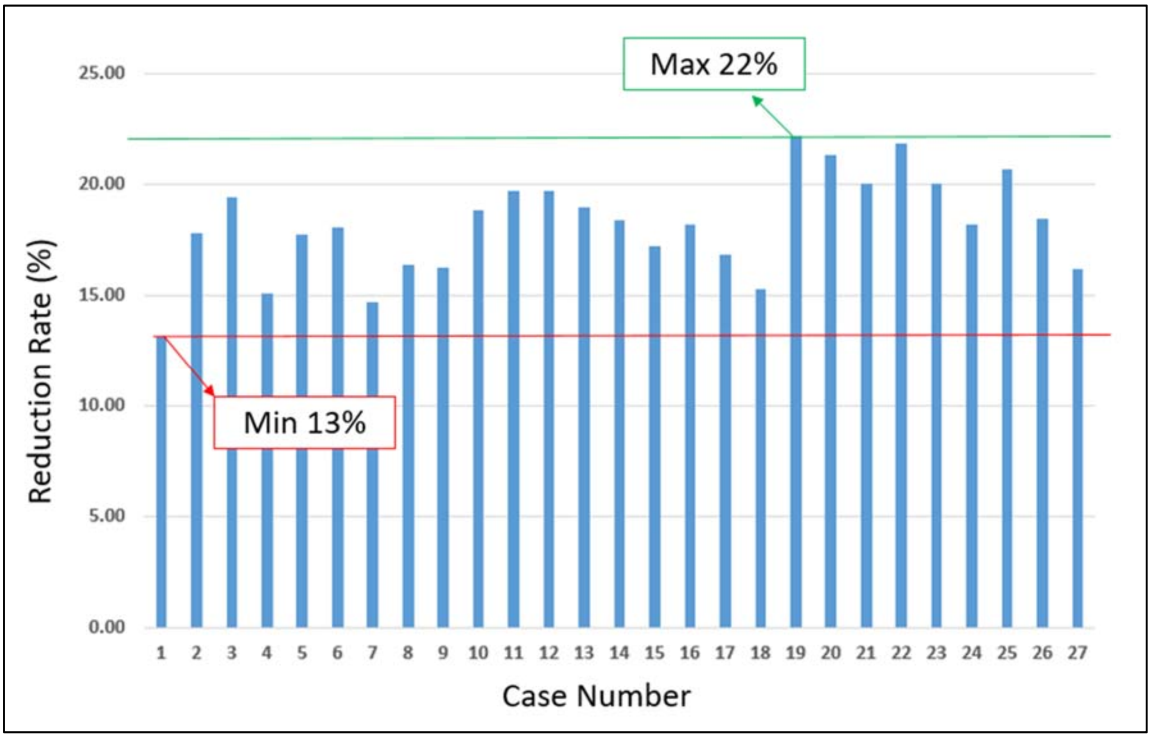

Figure 7.1: Reduction Rate Values for 1/32 H_{cs} for 27 Analysis

Figure 7.2 shows the reduction rate rates of 1/16 H_{cs}. It is obvious that the honeycomb structure used with 1/16 H_{cs} has increased the amount of leakage flow instead of decreasing it. In Figure 7.3 flow in labyrinth seal with 1/16 H_{cs} now proceeds by using the large gaps in the honeycombs and this increases the effective flow area thus the leakage flow increases. This clearly shows that the selection of honeycomb cell size is critical in influencing the amount of leakage flow.

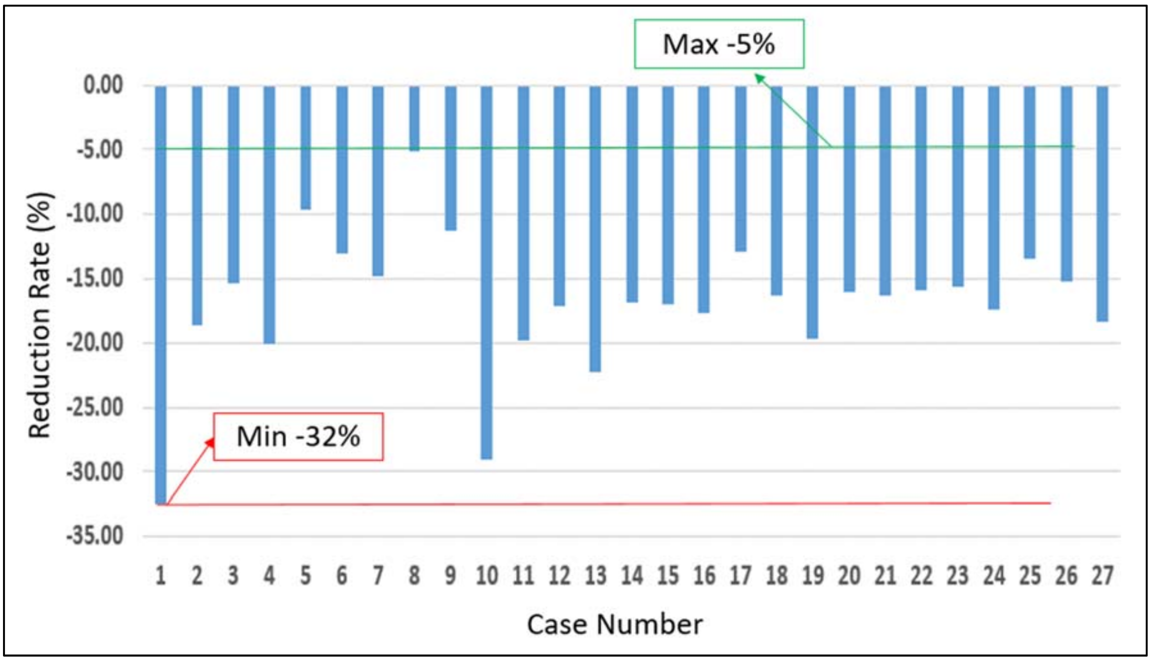

Figure 7.2: Reduction Rate Values for 1/16 H_{cs} for 27 Analysis

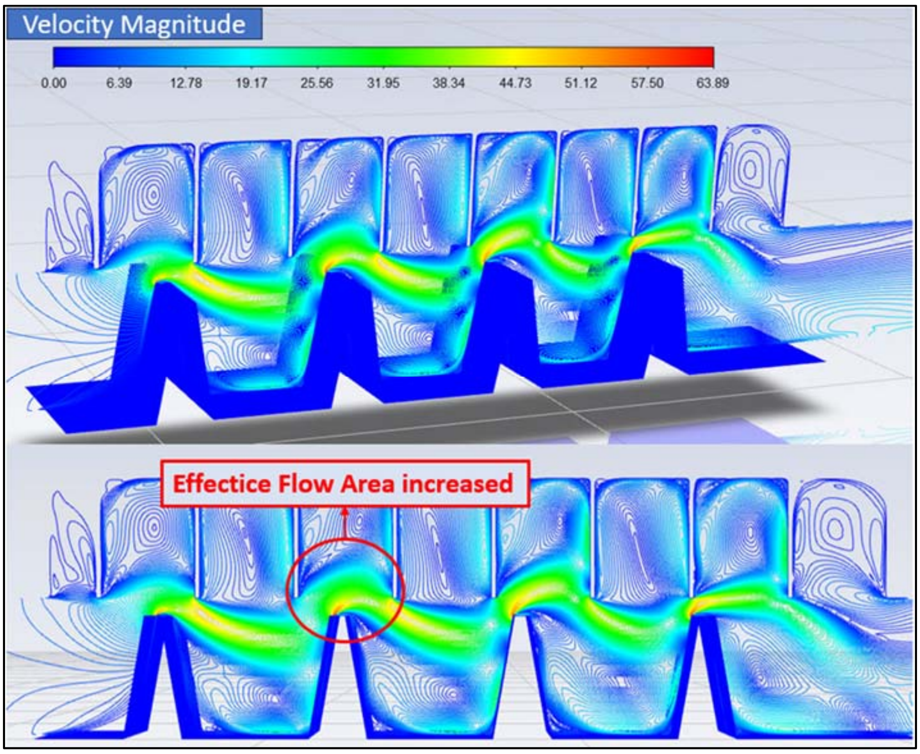

Figure 7.3: Velocity Magnitude Flow Field with 1/16 Hcs

7.1. Reduction Rate Equation for 1/32 Hcs

Minitab statistical program was used to create a CFD-based equation for the reduction rate. In this program, regression analysis was performed and Equation 7.1 was obtained for geometries with 1/32 cell size value. Aim is to find an equation which includes with honeycomb cases. The aim here is to predict how much leakage flow rate will decrease with using 1/32 honeycomb lands without need for CFD analysis. Figure 7.4 is representing the reduction rate result comparison of regression equation and CFD. a maximum deviation of 2% is observed as a value which is acceptable. The resulting equation depends on clearance and tooth tip thickness. Pitch and honeycomb depth effects are not included. In the following two sections, the correction coefficients were obtained according to the changes in pitch and honeycomb depth. In equation 7.1 k_{sc} coefficient needs to be find and in order to find this coefficient the analysis matrix shown in Table 7.2 was created and solved.

$$Reduction\ Rate = (B_1 - B_2 * c - B_3 * PR + B_4 * tt) * k_{sc} \qquad 7.1$$

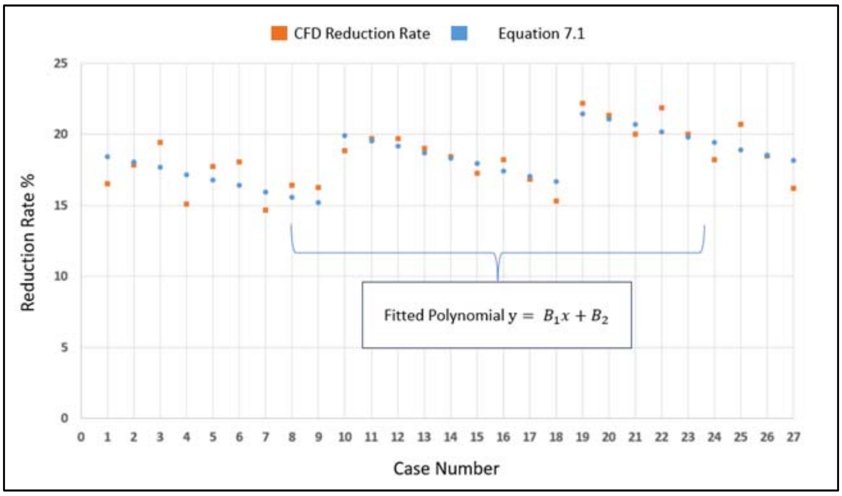

Figure 7.4 Reduction Rate CFD vs Equation 7.1

The variation of the pitch to clearance ratio effect on the reduction rate for different clearance values is shown in Figure 7.5. It can be shown that there is a linear trend between 6-20 s/c ratio. This result can be combined with equation 7.1 and new correction can be added which is indicated as k_{sc}. Equation 7.2 used to find k_{sc} coefficient.

Table 7.2: Analysis Matrix for Pitch Effect on Reduction Rate with 1/32 H_{cs}

Case No	Clearance [mm]	Pitch [mm]
1-4	0.3	3-4-5-6
5-8	0.4	3-4-5-6
9-12	0.5	3-4-5-6

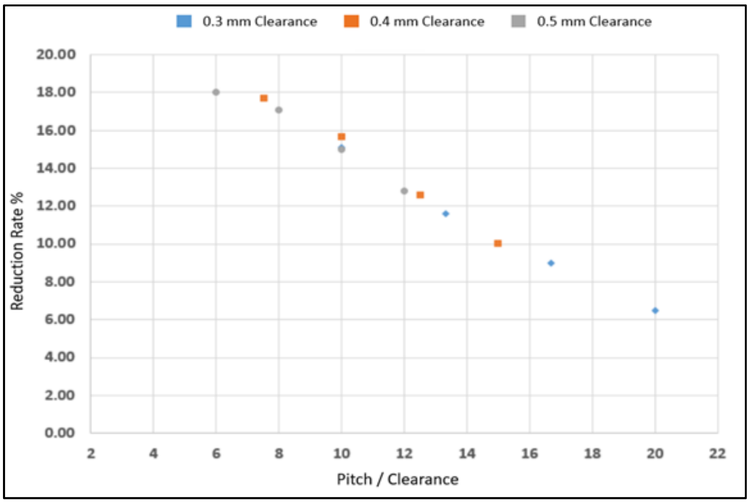

Figure 7.5 Reduction Rate Relationship with Pitch to Clearance Ratio for Different Clearances

$$k_{sc} = B_5 * \frac{s}{c} + B_6 \tag{7.2}$$

8. OPTI-SEAL TOOL

In order to make the obtained correlations usable, a tool was developed to make it easy to use these correlations. Main aim of this tool is to find an optimum seal according to the designer limitations with using one dimensional equation. To achieve this, Microsoft Excel was used with Python. Opti-seal tool allow easy integration of the developed correlations as experiments are conducted, and to enable the solution of multiple seal geometries with and without honeycomb land. An optimization code has been prepared with python language and code mainly using the random search strategy. In order to solve original and new Zimmerman-Wolff equation the secant method has been used due to iterative solution requirements of these equations. The user can set the equation to be solved and the design limitations as shown in Figure 8.1. At the end of the solution opti-seal optimization code will provide a list of the best possible labyrinth seals that meet the designer limitations.

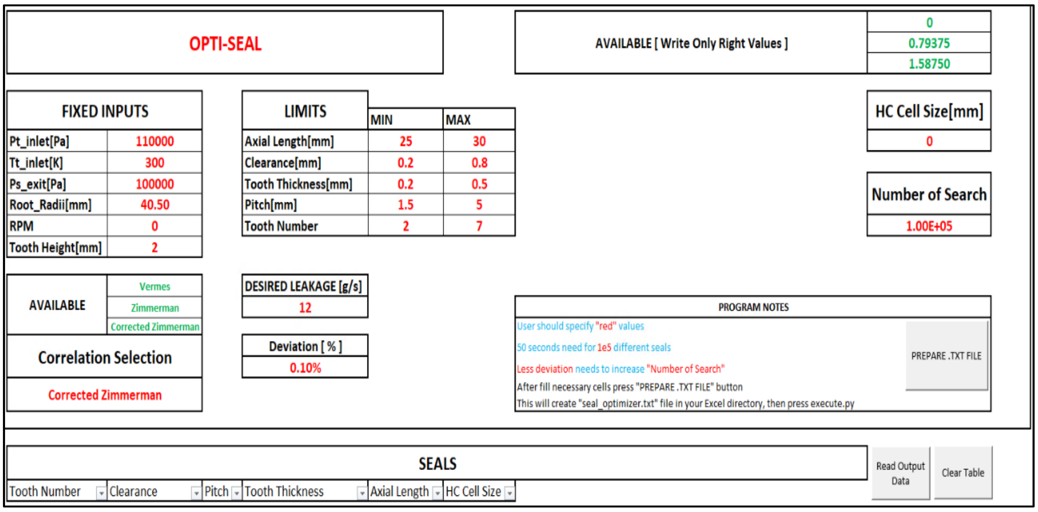

OPTI-SEAL

FIXED INPUTS	
Pt_inlet[Pa]	110000
Tt_inlet[K]	300
Ps_exit[Pa]	100000
Root_Radii[mm]	40.50
RPM	0
Tooth Height[mm]	2

LIMITS	MIN	MAX
Axial Length[mm]	25	30
Clearance[mm]	0.2	0.8
Tooth Thickness[mm]	0.2	0.5
Pitch[mm]	1.5	5
Tooth Number	2	7

AVAILABLE [Write Only Right Values]
0
0.79375
1.58750

HC Cell Size[mm]: 0

Number of Search: 1.00E+05

AVAILABLE
Vermes
Zimmerman
Corrected Zimmerman

Correlation Selection: Corrected Zimmerman

DESIRED LEAKAGE [g/s]: 12

Deviation [%]: 0.10%

PROGRAM NOTES

User should specify "red" values

50 seconds need for 1e5 different seals

Less deviation needs to increase "Number of Search"

After fill necessary cells press "PREPARE .TXT FILE" button

This will create "seal_optimizer.txt" file in your Excel directory, then press execute.py

SEALS

Tooth Number	Clearance	Pitch	Tooth Thickness	Axial Length	HC Cell Size

Figure 8.1 Opti-Seal Tool Interface

8.1. Opti-Seal Tool Working Procedure

The working procedure of the Opti-Seal program is explained step by step below.

- The designer creates the necessary constraints for the straight through labyrinth seal in Microsoft Excel. A “.txt” file is prepared for the Python code.
- The necessary information is obtained by reading the “.txt” file in Python code.
- Individuals (seals) are randomly generated to fit the designer's constraints. The number of individuals to be created is 100,000 by default.
- Each individual represents a labyrinth seal and the necessary equation (selected by the designer at step 1) is selected to calculate the leakage flow of these labyrinth seals.
- An iterative solution method is required to solve the selected equations, and the secant method has been used.
- The results of each individual are compared and individuals who fulfill the designer's request ±0.1% are selected.
- The resulting individuals are printed as a “.txt” file. The designer makes a choice by reading this file from Microsoft Excel.

8.2. Secant and Random Search Method

The secant method is a root-finding procedure in numerical analysis that uses a series of roots of secant lines to better approximate a root of a function f. The secant method procedures are given below:

1- X_0 and X_1 of are taken as initial guesses.
2- $x_{n+1} = x_n - \frac{f(x_n)*(x_n - x_{n-1})}{f(x_n) - f(x_{n-1})}$ (Iterative procedure)
3- Iterative procedure goes on until function error reaches desired

Random search method is a family of numerical optimization methods that do not require the gradient of the problem to be optimized.

Let f: $R^n \rightarrow R$ be the fitness or cost function which must be minimized. Let $x \in R^n$ designate a position or candidate solution in the search-space. X will initialize with a random position in the search-space. Until a termination criterion is met (e.g., designer mass flow rate with error band), repeat the create random numbers in accordance with the restrictions.) All design parameters are determined randomly within the limits entered by the designer.

9. CONCLUSION

In the context of this thesis, straight through labyrinth seals were investigated both experimentally and numerically under both static and dynamic conditions. To demonstrate the accuracy of the numerical model developed within the scope of this thesis, comprehensive comparisons were conducted with existing literature and experimental studies. Based on the insights gained from CFD analyses and experimental investigations, the frequently utilized Zimmerman-Wolff equation in the literature was improved by applying a hybrid turbulence model approach. Correction coefficients were developed to enhance its compatibility with experimental results.

Within the scope of this study, an extensive number of analyses were conducted using parametric models developed in both 2D and 3D. Through 2D full factorial analyses, the study determined the relative importance of geometric parameters on leakage flow, swirl ratio, and windage heating. Additionally, the Taguchi approach, commonly employed in the literature for 3D analyses, yielded significant results from a limited number of simulations.

The study also delved into the intricate flow phenomena within labyrinth seals, namely the "vena contracta" and "lid-driven cavity," examining their interplay and associated effects. Furthermore, the study compared the performance of the k-ε Realizable and k-ω SST turbulence models, widely utilized in industrial CFD applications, across different labyrinth seal geometries and boundary conditions.

A total of 972 analyses were conducted to investigate the impact of RPM on swirl and windage heating numbers. The study examined how RPM affected the leakage flow and observed a reduction of up to 15% compared to static conditions under the existing parameters. Furthermore, swirl-flow function and windage heating number-flow function relations were showed. These results demonstrated that similar results can be achieved by selecting appropriate geometric parameters.

The effect of honeycomb structures with 1/16 and 1/32 cell sizes on leakage flow was examined numerically and compared with the experimental results in the existing literature. In analyzes with 1/16 cell size, it was clearly observed that the fluid increased the leakage flow instead of decreasing it by taking advantage of the space in the honeycomb structure cells. Additionally, relationships between clearance to tooth thickness ratio and pitch to clearance ratio were obtained, and a one-dimensional equation which containing the parameters of clearance, pitch, and pressure ratio was derived for the reduction rate.

At the end of the study, a one-dimensional Opti-Seal tool was developed in order to find optimum labyrinth seal. This tool uses designer constraints and both existing and improved one-dimensional correlations. Opti-Seal can solve 100.000 different seals using random-search method and it can quickly analyze the multiple labyrinth seal geometries.

REFERENCES

[1] Becker, “E. Strömungsvorgänge in Ringformigen Spalten (Labyrinth-Dichtungen)”.

[2] M. H. M., “Labyrinth Packings,” *Engineering*, vol. 85, p. 35, 1908, [Online]. Available: https://cir.nii.ac.jp/crid/1571980075787794432.bib?lang=en

[3] ESTU, “ESDU_09004_Labyrinth_seal_flow.pdf.”

[4] Stodola, *Steam and Gas Turbines*. 1927.

[5] A. Egli, “The Leakage of Steam Through Labyrinth Seals,” *J. Fluids Eng.*, vol. 57, no. 3, pp. 115–122, 1935, doi: 10.1115/1.4019911.

[6] B. Hodkinson, J. W. Baxter, and J. R. Bumby, “Proceedings of the Institution of Mechanical Engineers , Part I : Journal of Systems and Control Engineering,” 1995, doi: 10.1243/PIME.

[7] G. Vermes, “A fluid mechanics approach to the labyrinth seal leakage problem,” *J. Eng. Gas Turbines Power*, vol. 83, no. 2, pp. 161–169, 1961, doi: 10.1115/1.3673158.

[8] T. P. Flow, H. Zimmerman, and K. H. Wolff, “Air System Correlations Part 1: Labyrinth Seals,” pp. 1–8, 2016.

[9] D. L. Rhode and R. I. Hibbs, “Tooth thickness effect on the performance of gas labyrinth seals,” *J. Tribol.*, vol. 114, no. 4, pp. 790–795, 1992, doi: 10.1115/1.2920950.

[10] C. A. Meyer and J. A. Lowrie, “The leakage thru straight and slant labyrinths and honeycomb seals,” *J. Eng. Gas Turbines Power*, vol. 97, no. 4, pp. 495–501, 1975, doi: 10.1115/1.3446041.

[11] S. Suryanarayanan and G. L. Morrison, “Effect of tooth height, tooth width and shaft diameter on carry-over coefficient of labyrinth seals,” *Proc. ASME Turbo Expo*, vol. 3, no. PART B, pp. 1147–1152, 2009, doi: 10.1115/GT2009-59246.

[12] S. Suryanarayanan and G. L. Morrison, “Analysis of flow parameters influencing carry-over coefficient of labyrinth seals,” *Proc. ASME Turbo Expo*, vol. 3, no. PART B, pp. 1137–1145, 2009, doi: 10.1115/GT2009-59245.

[13] S. Suryanarayanan and G. L. Morrison, “Labyrinth seal discharge coefficient for rectangular cavities,” *Proc. ASME Fluids Eng. Div. Summer Conf. 2009, FEDSM2009*, vol. 2, pp. 99–114, 2009, doi: 10.1115/FEDSM2009-78152.

[14] H. L. Stocker, “Advanced Labyrinth Seal Design Performance for High Pressure Ratio Gas Turbines.,” *Am. Soc. Mech. Eng.*, no. 75-WA/GT-22, 1975.

[15] J. A. Demko, G. L. Morrison, and D. L. Rhode, “Effect of shaft rotation on the incompressible flow in a labyrinth seal,” *J. Propuls. Power*, vol. 6, no. 2, pp. 171–176, 1990, doi: 10.2514/3.23240.

[16] W. Ma, Z. Chen, and Y. Jiao, “Leakage and whirl speed study in labyrinth seal using CFD,” *Proc. 2011 Int. Conf. Electron. Mech. Eng. Inf. Technol. EMEIT 2011*, vol. 2, pp. 592–595, 2011, doi: 10.1109/EMEIT.2011.6023171.

[17] W. Waschka, S. Wittig, and S. Kim, “Influence of high rotational speeds on the heat transfer and discharge coefficients in labyrinth seals,” *J. Turbomach.*, vol. 114, no. 2, pp. 462–468, 1992, doi: 10.1115/1.2929166.

[18] H. L. Stocker, R. Ei, D. M. Cox, and G. F. Holle, “AERODYNAMICPERFORMANCEOF CJNVENTIONALAND ADVANCED DESIGNLABYRINTHSEALSWITH SOLID-SMOOTHABRADABLEAND HONEYCOMBLAND,” 1977.

[19] K. Willenborg, V. Schramm, S. Kim, and S. Wittig, “Influence of a honeycomb facing on the heat transfer in a stepped labyrinth seal,” *J. Eng. Gas Turbines Power*, vol. 124, no. 1, pp. 133–139, 2002, doi: 10.1115/1.1403459.

[20] D. L. R. Dong-Chun Choi, “Development of A 2-D CFD Approach For Computing 3-D Hoenycomb Labyrinth Leakage,” pp. 1–11, 2017.

[21] J. Li, Q. Deng, and Z. Feng, “Numerical investigations of the flow characteristics in the straight-through honeycomb seal,” *Proc. 2005 ASME Fluids Eng. Div. Summer Meet. FEDSM2005*, vol. 2005, pp. 1046–1052, 2005, doi: 10.1115/FEDSM2005-77064.

[22] R. T. Alessio Desando, Andrea Rapisarda, Elena Campagnoli, “NUMERICAL ANALYSIS OF HONEYCOMB LABYRINTH SEALS: CELL GEOMETRY AND FIN TIP THICKNESS IMPACT ON THE DISCHARGE COEFFICIENT,” pp. 1–11, 2017.

[23] D. Frączek, W. Wróblewski, and K. Bochon, “Influence of honeycomb rubbing on the labyrinth seal performance,” *J. Eng. Gas Turbines Power*, vol. 139, no. 1, pp. 1–10, 2017, doi: 10.1115/1.4034183.

[24] K. C. Nayak and P. Dutta, “Numerical investigations for leakage and windage heating in straight-through labyrinth seals,” *J. Eng. Gas Turbines Power*, vol. 138, no. 1, pp. 1–10, 2016, doi: 10.1115/1.4031343.

[25] X. Kong, “Gt2016-56740 Development of Rotating Labyrinth Seal in a Compressor Stator,” pp. 1–10, 2016.

[26] D. Frączek and W. Wróblewski, “Validation of numerical models for flow simulation in labyrinth seals,” *J. Phys. Conf. Ser.*, vol. 760, no. 1, 2016, doi: 10.1088/1742-6596/760/1/012004.

[27] W. Rodi, *Turbulence models and their application in hydraulics.*, vol. 1101. 1984. doi: 10.1016/0045-7825(81)90171-7.

[28] “Turbulence Modeling for CFD David C. Wilcox,” *Turbul. Model. CFD*, vol. 206, no. d, pp. 4–6, 2013.

[29] Y. Dogu, M. C. Sertçakan, A. S. Bahar, A. Pişkin, E. Arican, and M. Kocagül, “Computational Fluid Dynamics Investigation of Labyrinth Seal Leakage Performance Depending on Mushroom-Shaped Tooth Wear,” *J. Eng. Gas Turbines Power*, vol. 138, no. 3, pp. 1–10, 2016, doi: 10.1115/1.4031369.

[30] G. Liu, X. Kong, Y. Liu, and Q. Feng, “Effects of rotational speed on the leakage behavior, temperature increase, and swirl development of labyrinth seal in a compressor stator well,” *Proc. Inst. Mech. Eng. Part G J. Aerosp. Eng.*, vol. 231, no. 13, pp. 2362–2374, 2017, doi: 10.1177/0954410016664929.

BIOGRAPHY

Avni Ertas holds a Bachelor of Science degree in Mechanical Engineering from Kocaeli University, which he obtained in 2019. Currently, Avni is employed at Tusas Engine Industry as an Aerodynamics Design Engineer since May 2021. Avni is fluent in both Turkish (his native language) and English.

APPENDIX

Case Number	Honeycomb Cell Size [mm]	Tooth Thickness [mm]	Pressure Ratio	Clearance[mm]
1	0.79375 & 1.5875	0.25	1.1	0.3
2	0.79375 & 1.5875	0.25	1.1	0.4
3	0.79375 & 1.5875	0.25	1.1	0.5
4	0.79375 & 1.5875	0.25	1.3	0.3
5	0.79375 & 1.5875	0.25	1.3	0.4
6	0.79375 & 1.5875	0.25	1.3	0.5
7	0.79375 & 1.5875	0.25	1.5	0.3
8	0.79375 & 1.5875	0.25	1.5	0.4
9	0.79375 & 1.5875	0.25	1.5	0.5
10	0.79375 & 1.5875	0.45	1.1	0.3
11	0.79375 & 1.5875	0.45	1.1	0.4
12	0.79375 & 1.5875	0.45	1.1	0.5
13	0.79375 & 1.5875	0.45	1.3	0.3
14	0.79375 & 1.5875	0.45	1.3	0.4
15	0.79375 & 1.5875	0.45	1.3	0.5
16	0.79375 & 1.5875	0.45	1.5	0.3
17	0.79375 & 1.5875	0.45	1.5	0.4
18	0.79375 & 1.5875	0.45	1.5	0.5
19	0.79375 & 1.5875	0.65	1.1	0.3
20	0.79375 & 1.5875	0.65	1.1	0.4
21	0.79375 & 1.5875	0.65	1.1	0.5
22	0.79375 & 1.5875	0.65	1.3	0.3
23	0.79375 & 1.5875	0.65	1.3	0.4
24	0.79375 & 1.5875	0.65	1.3	0.5
25	0.79375 & 1.5875	0.65	1.5	0.3
26	0.79375 & 1.5875	0.65	1.5	0.4
27	0.79375 & 1.5875	0.65	1.5	0.5